

The $K_v10.1$ voltage gated potassium ion channel modulates the cell adhesion and cell migration hallmarks of cancer

Doctoral Thesis

In partial fulfillment of the requirements for the degree “Doctor rerum naturalium (Dr. rer. nat.)” in the Molecular Medicine Study Program at the Georg-August University
Göttingen

submitted by

Ioannis K. Alexopoulos

born in
Chania, Greece

Göttingen
April 2015

Members of the Thesis Committee

Prof. Dr. Walter Stühmer, Department of Molecular Biology of Neuronal Signals, Max Planck Institute of Experimental Medicine, Göttingen, Germany

Prof. Dr. Luis A. Pardo, Department of Molecular Biology of Neuronal Signals, Max-Planck Institute of Experimental Medicine, Göttingen, Germany

Dr. Dieter Klopfenstein, Department of Biophysics, Third Institute of Physics, Göttingen, Germany

Date of Disputation: 15/06/2015

Declaration

I hereby declare that this doctoral thesis has been written independently with no other sources and aids than quoted.

Ioannis K. Alexopoulos

Göttingen, April 2015

List of Publications

1. A. M. Jiménez-Garduño, M. Mitkovski, I. K. Alexopoulos, A. Sánchez, W. Stühmer, L. A. Pardo, and A. Ortega, “K_v10.1 K(+) channel plasma membrane discrete domain partitioning and its functional correlation in neurons,” *Biochim. Biophys. Acta*, vol. 1838, no. 3, pp. 921–931, Nov. 2013.
2. Schanila Nawaz, Paula Sánchez, Sebastian Schmitt, Nicolas Snaidero, Mišo Mitkovski, Caroline Velte, Bastian Rouven Brückner, Ioannis Alexopoulos, Tim Czopka, Sang Yong Jung, Jeong Seop Rhee, Andreas Janshoff, Walter Witke, Iwan AT Schaap, David A. Lyons, Mikael Simons, “Actin filament turnover drives leading edge growth during myelin sheath formation in the central nervous system”, [Submitted]
3. I. K. Alexopoulos, L. A. Pardo, W. Stühmer, M. Mitkovski, “K_v10.1 overexpression enhances cell migration, while reducing cell-cell and cell-surface adhesion”, [Working Title - Under Preparation]
4. I. K. Alexopoulos, K. Bröking, L. A. Pardo, W. Stühmer, M. Mitkovski, “Cell migration is affected by the level and the pattern of laser energy dosage”, [Working Title - Under Preparation]
5. I. K. Alexopoulos, W. Stühmer, M. Mitkovski, “ProRet: A novel algorithm to dynamically quantify surface adhesion ability from Interference Reflection Microscopy data”, [Working Title - Under Preparation]

Contents

| | |
|---|-------------|
| Acknowledgments | iv |
| Abstract | v |
| List of Figures | vi |
| List of Tables | viii |
| List of Abbreviations | ix |
| 1 Introduction | 1 |
| 1.1 Ion channels | 1 |
| 1.2 $K_v10.1$ | 2 |
| 1.2.1 Classification | 2 |
| 1.2.2 Sequence and structure | 2 |
| 1.2.3 Electrophysiological properties | 5 |
| 1.2.4 Role | 6 |
| 1.3 Cell migration | 8 |
| 1.3.1 Significance | 8 |
| 1.3.2 Types of cell migration | 8 |
| 1.3.3 Ion channels and cell migration | 10 |
| 1.3.4 Primary cilia | 11 |
| 1.4 Cell-cell adhesion | 11 |
| 1.5 Cell-surface adhesion | 12 |
| 1.6 Acquisition settings and cell migration | 13 |
| 1.7 Scratch assay | 14 |
| 1.8 Interference reflection microscopy | 15 |
| 1.8.1 IRM principle | 16 |
| 1.8.2 Quantification | 18 |
| 1.9 TIRF | 18 |
| 2 Materials & Methods | 20 |
| 2.1 Cell lines manipulation | 20 |
| 2.1.1 Cell lines | 20 |
| 2.1.2 Normal culture | 20 |
| 2.1.3 Transfection | 21 |
| 2.1.4 Cell Sorting | 21 |
| 2.2 Electrophysiology | 21 |
| 2.3 Molecular biology | 22 |
| 2.3.1 RNA purification | 22 |
| 2.3.2 Reverse transcriptase PCR | 23 |
| 2.3.3 Real-time PCR | 23 |
| 2.4 Biochemistry | 24 |
| 2.4.1 Protein extraction | 24 |
| 2.4.2 Protein quantification | 24 |
| 2.4.3 SDS-PAGE protein separation | 25 |

| | | |
|----------|---|-----------|
| 2.4.4 | Fluorescent detection from gel | 25 |
| 2.4.5 | Immunoprecipitation | 26 |
| 2.4.6 | Western blot detection | 26 |
| 2.5 | Immunocytochemistry | 28 |
| 2.5.1 | Primary cilia | 28 |
| 2.5.2 | Focal adhesion kinase | 28 |
| 2.5.3 | Phalloidin staining | 29 |
| 2.6 | Interference reflection microscopy | 29 |
| 2.6.1 | Acquisition | 29 |
| 2.6.2 | Quantification | 30 |
| 2.7 | Scratch assay | 31 |
| 2.7.1 | Sample preparation | 31 |
| 2.7.2 | Live imaging conditions | 32 |
| 2.7.3 | Microscope settings | 32 |
| 2.8 | Cell surface adhesion | 33 |
| 2.8.1 | Sample preparation | 33 |
| 2.8.2 | Cell-surface adhesion ability | 33 |
| 2.8.3 | Cell-surface adhesion dynamics | 33 |
| 2.8.4 | TIRF | 34 |
| 2.9 | Image analysis | 34 |
| 2.9.1 | Scratch assay | 34 |
| 2.9.2 | Scratch assay with IRM | 36 |
| 2.9.3 | Individual cell tracking measurements | 37 |
| 2.9.4 | Cell-surface adhesion ability | 38 |
| 2.9.5 | Cell-surface adhesion dynamics | 39 |
| 2.10 | Stimulation / acquisition settings effect | 40 |
| 2.10.1 | Laser measurements | 40 |
| 2.10.2 | Sample preparation | 42 |
| 2.10.3 | Microscope settings | 42 |
| 2.10.4 | Image analysis | 45 |
| 2.11 | Statistical analysis | 45 |
| 3 | Results | 46 |
| 3.1 | Electrophysiology | 46 |
| 3.2 | Molecular biology | 46 |
| 3.3 | Biochemistry | 47 |
| 3.3.1 | Fluorescent detection from gel | 47 |
| 3.3.2 | Immunoprecipitation and Western blot | 48 |
| 3.4 | K _v 10.1 localization | 49 |
| 3.5 | Cell migration | 51 |
| 3.5.1 | Effect of stimulation / acquisition settings on scratch closure speed | 51 |
| 3.5.2 | K _v 10.1 increases scratch closure speed | 53 |
| 3.5.3 | Effect of K _v 10.1 on individual cell migration | 54 |
| 3.6 | Cilia formation | 57 |
| 3.7 | Cell-cell adhesion | 59 |
| 3.8 | Cell-surface adhesion | 60 |
| 3.8.1 | Adhesive area at migration front | 60 |

| | | |
|----------|---|------------|
| 3.8.2 | Cell-surface adhesion ability | 61 |
| 3.8.3 | Cell-surface adhesion dynamics | 62 |
| 3.8.4 | Focal Adhesion Kinase in FA sites | 65 |
| 4 | Discussion | 66 |
| 4.1 | Stimulation / acquisition setting-dependent cell behavior | 67 |
| 4.1.1 | Fluorochromes in higher energy states increase cell migration speed | 67 |
| 4.1.2 | Optimal settings for live imaging of cell migration | 68 |
| 4.2 | Cell adhesion | 69 |
| 4.2.1 | K _v 10.1 reduces cell-surface adhesion | 69 |
| 4.2.2 | K _v 10.1 reduces cell-cell adhesion in migrating cells | 71 |
| 4.3 | K _v 10.1 overexpression enhances cell migration while reducing direction- ality | 72 |
| 5 | Conclusions and perspectives | 73 |
| 6 | Appendix / Algorithms | 76 |
| 6.1 | List of primary antibodies | 76 |
| 6.2 | Adhesion dynamics algorithm (“ProRet”) | 76 |
| | Bibliography | 82 |
| | Curriculum vitae | 103 |

Acknowledgments

I would like to thank my supervisor Dr. Mitkovski for his continuous guidance and helpful instructions throughout this project. He was the one that introduced me to the field of microscopy and educated me properly for image acquisition and analysis. I owe him a big part of the knowledge that I earned the last 3 years.

I am also extremely grateful to Prof. Dr. Walter Stühmer for accepting me as a PhD student and for his valuable suggestions during this project. I feel honored for being under the supervision of this exceptional, kind and approachable scientist. Particularly, I would like to thank him for being there for me whenever I needed him despite his tight schedule.

I would like also to express my appreciation to Prof. Dr. Luis Pardo, not only for his guidance during my PhD, but also for his willingness to discuss with me whenever I asked for. I am thankful for his practical help during this project and especially for his kindness. His scientific integrity will always be a gold standard for me.

Furthermore, I would like to honor the memory of Prof. Dr. Uwe Hanisch. Through his participation to all my committee meetings and the productive scientific discussions we had, I realized what a committed, gentle and intelligent scientist, and above all, person he was. His unfortunate and sudden loss made the scientific community much poorer.

Additionally, I want to express my gratitude to Mrs. Sabine Klöppner for her exceptional technical support. She was the person that introduced me to cell culturing and she was always available for me. I also owe many thanks to Dr. Vincenzo Romaniello for his kind help with the part of molecular biology and biochemistry. He is a great scientist and also a good friend. Moreover, I need to thank Mrs. Ute Rust and Mrs. Svea Dettmer for their kindness and their support during all these years. Both were present for me ready to solve any of my problems.

In general, I would like to thank all the members of the MBNS department, for their kindness, their help, their support and suggestions especially during our weekly seminars and for the pleasant atmosphere they created.

At last but not least, θα ήθελα να ευχαριστήσω τους γονείς μου και τα αδέρφια μου για την ηθική υποστήριξη και την πίστη τους σε εμένα. Ιδιαίτερα όμως οφείλω μεγάλη ευγνωμοσύνη στην σύζυγό μου Λίλα και στην κόρη μου Ευγενία, για την καθημερινή στήριξή τους στο δύσκολο δρόμο που έπρεπε να διανύσω προς την ολοκλήρωση αυτής της εργασίας. Ήταν τα πρόσωπα από τα οποία αντλούσα την απαραίτητη δύναμη κάθε στιγμή.

Abstract

A characteristic of the $K_v10.1$ voltage-gated potassium ion channel is its overexpression in a number of cancerous tissues and cancer cell lines, even though it should normally be restricted to the adult brain and myoblasts. This compelled us to investigate the role this ion channel may play in cancer, where we initially localized it in filopodia, lamellipodial regions and at cell-cell or cell-surface adhesion interfaces, all of which are important for cell migration, a hallmark of cancer. Therefore, to further study how $K_v10.1$ affects cell motility and adhesion, we generated two HT-1080 cell lines stably overexpressing either $K_v10.1$ -mVenus or only mVenus, both of which were then tasked to migrate induced by means of the scratch assay. However, cell behavior may be affected by the recording method used. We therefore conducted a methodological survey of a number of previously undescribed image acquisition scenarios, which enabled us to identify hardware settings with the least influence on cell behavior. Semi-automated, live-cell microscopy and image analysis revealed then that $K_v10.1$ overexpression lead to faster scratch-closure speeds with an accompanying loss of cell-cell adhesion, when compared to the control. Individual cell tracking showed that $K_v10.1$ overexpression enabled HT-1080 cells to migrate at a faster maximum speed, but along a less directed, longer and more complex path, given the same timespan. Additional experiments using interference reflection microscopy and a novel quantification algorithm, enabled us to detect cell-surface adhesion deficits due to $K_v10.1$ overexpression, which are present in stationary cells and likely cause the less coordinated, more invasive and faster migration with more degrees of freedom. We confirmed $K_v10.1$ overexpression to be the cause of the aberrant cell behavioral effects by the use of $K_v10.1$ -specific antibody mAb56, as well as the antihistaminic drug astemizole. The results of this study indicate that the hallmarks of reduced cell adhesion and increased cell migration in cancer may depend on the abnormal $K_v10.1$ expression, the understanding of which may yield new diagnostic and treatment targets.

List of Figures

| | | |
|----|---|----|
| 1 | Classification, electrophysiological properties and schematic representation of $K_v10.1$ ion channel structure | 4 |
| 2 | Schematic representation of how $K_v10.1$ can influence tumorigenesis . . . | 7 |
| 3 | Morphologies of cells, types of migration, and possible transitions | 9 |
| 4 | Jablonski energy diagram | 14 |
| 5 | Principle of Interference Reflection Microscopy (IRM) | 17 |
| 6 | Fine adjustment of objective's correction collar for IRM acquisition . . . | 30 |
| 7 | Scratch assay acquisition with a 4-well chamber | 33 |
| 8 | Scratch closure dynamics | 34 |
| 9 | Scratch assay image analysis | 35 |
| 10 | Masks of IRM images during scratch closure | 36 |
| 11 | Manual tracking of cells migrating in a scratch | 37 |
| 12 | Cell-surface adhesion ability quantification | 39 |
| 13 | Cell-surface adhesion dynamics quantification | 40 |
| 14 | Laser measurements recordings | 41 |
| 15 | Calculated laser power plot | 41 |
| 16 | Calculated laser energy density | 42 |
| 17 | Representation of single and multiple acquisition settings | 44 |
| 18 | Schematic representation of scanning durations across the different acquisition settings | 44 |
| 19 | Correlation of fluorescent intensity with $K_v10.1$ current | 46 |
| 20 | The normalized levels of <i>KCNHI</i> mRNA with Real Time PCR | 47 |
| 21 | Fluorescent detection of gel separated proteins | 48 |
| 22 | Immunoprecipitation and WB detection of $K_v10.1$ -mVenus | 49 |
| 23 | $K_v10.1$ localization revealed with various techniques | 50 |
| 24 | Effect of $K_v10.1$ overexpression on scratch closure speed before and after channel's blockage | 54 |
| 25 | Cell trajectories plotted with a common origin point before and after the blocking of $K_v10.1$ | 55 |
| 26 | Effect of $K_v10.1$ overexpression on accumulated distance, maximum migration speed, average migration angle and straightness of individual migrating cells | 56 |
| 27 | Effect of $K_v10.1$ overexpression on mean square displacement before and after blockage | 57 |

| | | |
|----|---|----|
| 28 | Acetylated- α -tubulin staining, revealing the presence of several intercellular bridges (mid-bodies) and the absence of primary cilia in both types of HT-1080 cells. | 58 |
| 29 | Cell confluency under rest state for HT-1080-mVenus and HT-1080-K _v 10.1-mVenus cells | 59 |
| 30 | Effect of K _v 10.1 overexpression on cell-cell adhesion before and after channel's blockage | 60 |
| 31 | Normalized adhesive area at the lamellipodial region of migrating cells . . | 61 |
| 32 | Cell-surface adhesion ability expressed as % of cell footprint used in FA areas | 62 |
| 33 | Cell-surface adhesion dynamics over the time of acquisition | 63 |
| 34 | Cell-surface adhesion dynamics averages | 64 |
| 35 | Localization of FAK in FA sites as quantified by the IRM signal | 65 |
| 36 | Comparison of fluorochrome state transition and acquisition settings times | 68 |
| 37 | Dialogue menu of "ProRet" software | 77 |
| 38 | Adhesion dynamics analysis algorithm | 79 |

List of Tables

| | | |
|---|--|----|
| 1 | Reverse Transcription Reaction Buffer | 23 |
| 2 | BCA Assay standards dilution | 25 |
| 3 | Individual cell tracking measurements equations | 38 |
| 4 | Equations used for energy density calculations | 42 |
| 5 | Acquisition settings for laser effect study | 43 |
| 6 | Representation of statistical significance in diagrams | 45 |
| 7 | Stimulation / acquisition settings effect on scratch closure speed | 52 |
| 8 | Stimulation / acquisition settings effect on acquired fluorescence intensity | 53 |
| 9 | List of primary antibodies | 76 |

List of Abbreviations

| | |
|----------|--|
| AA | Acrylamide |
| Acc | Accumulation of acquired signal between lines |
| AD | Accumulated Distance: The distance covered during the interval displacements of each cell |
| APS | Pierce Ammonium Persulfate. An oxidizing agent used with TEMED for acrylamide polymerization |
| AST | Astemizole |
| Av | Averaging of acquired signal between frames |
| bis-AA | Bis-Acrylamide |
| BSA | Bovine Serum Albumin |
| CaMBD | Calmodulin binding domain |
| CaM | Calmodulin |
| cDNA | complementary DNA |
| CW | Continuous Wavelegth from solid state Argon laser |
| D-Rex | Dark state relaxation |
| dc | The Eucledian distance between the first and the last point of each cell route |
| ddH2O | Double-distilled water |
| DEPC-H2O | Diethylpyrocarbonate treated water |
| di | Interval displacements during the route of every marked cell |
| DMSO | Dimethyl sulfoxide |
| DNA | Desoxyribonucleic acid |
| DoF | Depth of Focus |
| DTT | Dithiothreitol |
| ECM | Extracellular matrix |

| | |
|--------|--|
| ED | Energy density |
| EDTA | Ethylenediaminetetraacetic acid |
| FIJI | Fiji Is Just ImageJ |
| FIR | Fluorescent intensity reduction |
| g | Earth's gravitational acceleration, traditionally named relative centrifugal force (RCF) |
| gr | Gram (0.001 kilogram) |
| HEPES | 4-(2-hydroxyethyl)-1-piperazineethanesulfonic acid |
| h | hours |
| IAO | Initial Area Occupied by cells after the introduction of the scratch |
| IFN | Interferon |
| IP | Immunoprecipitation |
| IRM | Interference Reflection Microscopy |
| ISF | Imaging solution with FCS |
| IS | Imaging solution |
| kDa | Kilo (1000) Daltons |
| LDS | Lithium dodecyl sulfate |
| Li-SDS | Lithium sodium dodecyl sulfate |
| L | Liter (1000 ml) |
| MA | Average Migration Angle |
| MIA | Maximum Intercellular Area |
| min | minutes |
| MSD | Mean Squared Displacement |
| ms | milliseconds (0.001 sec) |
| NA | Numerical Aperture |

| | |
|-------------|--|
| PAC | PAS associated C-terminal domain |
| PAS | Per-Arnt-Sim domain |
| PBS | Phosphate buffered saline |
| PCR | Polymerase Chain Reaction |
| PI | Protease inhibitor |
| RNA | Ribonucleic Acid |
| RT | Room temperature |
| SCS | Scratch Closure Speed |
| SDS-PAGE | Sodium dodecyl sulfate polyacrylamide gel electrophoresis |
| SDS | Sodium dodecyl sulfate |
| sec | seconds |
| SEM | Standard error of the mean |
| Str | Straightness: The ratio of final displacement (dc) and the accumulated distance (AD) |
| T-Rex | Triplet state relaxation |
| TB Syndrome | Temple-Baraitser Syndrome |
| TBS | Tris buffered saline |
| TBST | Tris buffered saline containing Tween-20 |
| TCC | Tetramerizing coiled-coil domain |
| TEA | Tetraethylammonium acetate |
| TEMED | Tetramethylethylenediamine used for polymerization of acrylamide |
| TIRF | Total internal reflection fluorescence |
| TRAIL | Tumor necrosis factor-related apoptosis-inducing ligand |
| u(max) | The maximum migration speed appearing during the route of a marked cell |

| | |
|---------|--|
| u(mean) | The mean of all the interval migration speeds of a marked cell |
| ui | The interval migration speeds of all tracked cells |
| w/v | Percent weight of solution in the total volume of solution |
| WB | Western Blot |
| WLL | White Light Laser |
| WL | Pulsed light from White Light Laser |

1 Introduction

1.1 Ion channels

One of the most crucial processes in cellular communication with its environment is the regulated ion flow across cell membranes since it accounts for the appropriate nutrient exposure, and participates in electrical signal generation, cell volume maintenance and cell migration [Hille (2001)]. The key players in passive ion flow are ion channels; transmembrane proteins with a specific tertiary structure that are able to form a pathway for the passage of ions. These channels, unlike simple aqua pores, allow the selective transition of a wide range of inorganic ions like Na^+ , K^+ , Ca^{2+} and Cl^- and their gating behavior is regulated.

The first mathematical description of ion channel function was derived from voltage clamp experiments in 1952 by Hodgkin and Huxley who quantified how changes in ion permeability generate action potentials in neurons [Hodgkin and Huxley (1952)]. Later, the patch-clamp technique invention allowed for real time recording and analysis of ion currents through individual channels [Neher et al. (1978)]. The first crystallographically solved structure of a bacterial potassium channel [Doyle et al. (1998)] by the end of the 90s lead to valuable insights into ion channel structure and function. Since then, we have learned that most ion channels consist of several subunits that are placed in circular symmetry forming a central pore perpendicular to membrane's lipid bilayer (Figure 1C). The structural diversity of ion channels is large and is in part due to the multitude of main subunits forming a wide variety of heteromeric channels. In addition, non-pore-forming auxiliary subunits are associated with the diverse ion channel types. [Bauer and Schwarz (2001)]. This structural diversity of ion channels is reflected in their spectra of gating behaviors. The principal gating stimulus involves voltage changes across the membrane (voltage gated channels), mechanical stimulation (mechanically gated channels), or ligand binding (ligand gated channels).

Due to the variety of different types of ion channels, a classification system was essential. Different classification methods are based on the gating stimulus of channels, on the type of ions or on other characteristics like the number of pores (e.g. two-pore channels) or the duration of the response to stimuli (transient receptor potential channels). However, the most widely accepted classification system nowadays is based on the International Union of Basic and Clinical Pharmacology (IUPHAR ¹). With this classification

¹www.guidetopharmacology.org

system the ion channel proteins are named using the chemical symbol of the permeating ion (Na, K, or Ca) followed by a subscript letter that indicates the gating regulator (e.g. v for voltage gated potassium channels, K_v) and then a number indicating the gene subfamily and a decimal that corresponds to the specific channel isoform.

1.2 K_v10.1

1.2.1 Classification

K_v10.1 (hEag1, human ether-à-go-go-1) is the founding member of the Eag family of voltage gated potassium ion channels (Figure 1A). Other members of this family are the Eag-related-gene (Erg) and the Eag-like (Elk) potassium channels. The name “eag” derives from a mutant causing a leg-shaking behavior in *Drosophila melanogaster* under ether anesthesia [Kaplan and Trout (1969)]. Subsequent cloning and analysis of the locus causing this behavior revealed a voltage-gated potassium ion channel [Bruggemann et al. (1993)]. Mammalian homologues of this channel were later identified in rat [Ludwig et al. (1994)], mouse [Warmke and Ganetzky (1994); Robertson et al. (1996)] and human [Occhiodoro et al. (1998)].

1.2.2 Sequence and structure

The human K_v10.1 protein is encoded by the *KCNH1* (h-*eag*) gene, which is located on chromosome 1q32-41 and is expressed as a 9 kb transcript in myoblasts and adult brain tissue. The encoded protein of this gene consists of 962 amino-acids (Figure 1B), with a predicted molecular weight of 108 kDa and an identity greater than 90% with the respective rat and mouse proteins [Occhiodoro et al. (1998)]. This protein constitutes the α -subunit of the fully functional K_v10.1 channel and is subjected to post-translational modifications (core or complex glycosylation) as described by Napp et al. (2005).

Every K_v10.1 channel consists of four identical α -subunits that are placed in a circular symmetry, forming a pore, through which potassium may permeate (Figure 1E). Every subunit consists of six transmembrane helical structural domains that are connected with 3 extracellular and 2 intracellular loops and has long intracellular amino- and carboxyl-termini (Figure 1C). The third extracellular loop, which connects the fifth and the sixth transmembrane domain, is longer, contains glycosylation sites and a big portion of this loop participates in the pore formation of the channel [Jiang et al. (2003); Bauer and Schwarz (2001)]. The spatial conformation of the structural elements of the K_v10.1 channel is also functionally important. It seems that the pore loop together with the fifth and the sixth transmembrane helices, participate in the pore formation, while the positively charged fourth helix is a part of the gating apparatus of the channel (Figure 1D and E).

Both intracellular termini contain functional domains, like a Per-Arnt-Sim (PAS)/PAS associated C-terminal (PAC) domain and an N-terminus calmodulin binding domain (CaMBD), two C-terminal CaMBDs, a cyclic nucleotide binding domain (cNBD) and a tetramerizing coiled-coil (TCC) domain at the C-terminus. The TCC domain is crucial for the assembly of the tetramerized form of a typical $K_v10.1$ channel [Jenke et al. (2003); Ludwig et al. (1997)], while CaMBD domains are important participating in the inhibition of the channel function with intracellular binding of Ca^{2+} /CaM to CaMBDs domains [Gonçalves and Stühmer (2010)]. The PAS domain together with cNBD and the C-terminus from different channel subunits assemble together and interact with the gating machinery, but in a still unknown manner [Morais-Cabral and Robertson (2014)].

In general, the structural conformation of the $K_v10.1$ channel, even though not so well studied as its electrophysiology, seems important for the non-conducting properties of the channel. These non-conducting properties are highly interdependent with the electrophysiological role of the channel and participate in the modulation of the role $K_v10.1$ plays under physiological or pathological conditions.

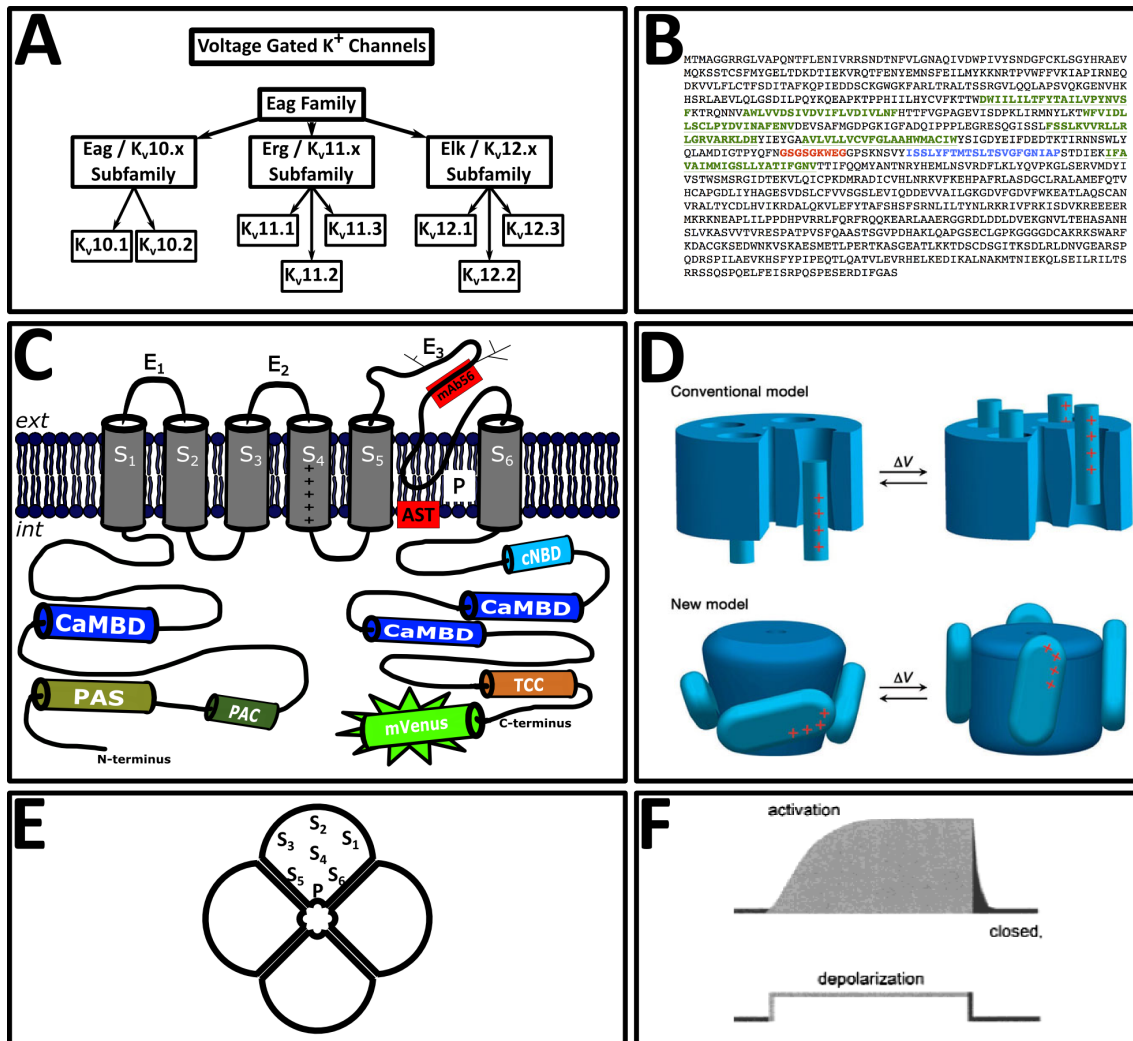


Figure 1 – (A) Classification of the Eag family of potassium channels, which belong to the voltage gated K^+ channels and includes three subfamilies (Eag, Erg and Elk). (B) The amino-acid sequence of human $K_v10.1$ α -subunit. The color-coded amino-acid sequence highlights the 6 transmembrane helical domains (S_1 - S_6) in green, the residues of the pore loop (blue) and the epitope recognized by the mAb56 (red). (C) The structure of an α -subunit of $K_v10.1$ -mVenus chimeric protein consisting of 6 transmembrane helical domains (S_1 - S_6), which are connected by 2 intracellular and 3 extracellular loops (E_1 - E_3). The positively charged S_4 domain acts as a voltage sensor for channel gating. A big portion of the E_3 loop (P) is located between the fifth and the sixth transmembrane domain, where it participates in the channel's pore formation together with the pore loops of three additional subunits. The small branches at the E_3 loop represent glycosylation sites, while the red boxes are binding sites for the mAb56 antibody and Astemizole (AST) blockers. Both N- and C-termini of each $K_v10.1$ subunit are intracellular and contain a number of functional domains, like the CaMBD, the cNBD, the PAS/PAC domain and a TCC domain. In our study, a chimeric form of $K_v10.1$ with monomeric Venus (mVenus) at its C-terminus (C) is stably expressed in HT-1080 cells. (D) Different models for tetrameric structures and voltage-dependent gating modes. In the conventional model, the gating charges (red plus signs) are carried through the protein core by movements of the S_4 helices, which move independently of other protein segments within the “gating pore”. In newer models, it is postulated that gating charges are carried through the membrane from inside (bottom) to outside (top) by movements of the voltage-sensor paddles within the lipid membrane, which in turn open the pore. (E) Proposed tetrameric structure of $K_v10.1$. The P loop together with the S_5 - S_6 domains form part of the channel's pore while the S_4 domain is placed in the middle of each subunit acting as a voltage sensor. (F) Representation of a $K_v10.1$ current. Upon a depolarization a slowly activating, non-inactivating outward current is obtained. Upon re-polarization a small tail current develops. Images A, C, E and F modified from Bauer and Schwarz (2001). Image D by Jiang et al. (2003).

1.2.3 Electrophysiological properties

The $K_v10.1$ channel, as a typical member of the EAG family of the voltage gated potassium channels, is characterized by the production of slow activating, outward rectifying currents that do not inactivate, while an inward rectification is present after strong depolarizations [Pardo et al. (1998)] (Figure 1F). The activation and inactivation of the $K_v10.1$ ion channel are a voltage dependent [Garg et al. (2012)]. The more depolarized the potential before the stimulation is, the faster the $K_v10.1$ activates. This characteristic is reminiscent of the Cole-Moore shift effect [Cole and Moore (1960)] and can be augmented by extracellular magnesium and protons [Terlau et al. (1996)]. The cell-cycle phase can also affect the $K_v10.1$ current. Inducing maturation of *Xenopus laevis* oocytes transfected with $K_v10.1$ reduced the current and exhibited a strong inward rectification [Bruggemann et al. (1997)]. Cell-cycle related changes can modify the conducting properties of $K_v10.1$ channels [Pardo et al. (1998)], while at the same time the conducting properties of potassium channels can play an active role in cell cycle progression [Urrego et al. (2014)].

$K_v10.1$ ion currents seem to be unaffected by potassium channels blockers such as tetraethylammonium acetate (TEA) and 4-aminopyridine [Bruggemann et al. (1993)]. The best known blockers for $K_v10.1$ are astemizole (AST) and imipramine [García-Ferreiro et al. (2004)]. AST is a commercially available anti-histaminic drug, targeting H1 histamine receptors, P-glycoproteins and potassium channels [Parsons and Ganellin (2006); García-Quiroz and Camacho (2011)]. H1 and H2 histamine receptor antagonists can inhibit the proliferative effect of histamine in malignant melanoma cells [Reynolds et al. (1996)] and astemizole influences doxorubicin growth inhibition in doxorubicin-resistant human leukemia cells by suppressing P-glycoprotein [Ishikawa et al. (2000)]. Astemizole is also known to block the $K_v10.1$ ion channel. It penetrates the cell and then allocates to the inner part of the channel pore. Blocked $K_v10.1$ channels stay in the open conformation, without the ability to transfer K^+ [García-Ferreiro et al. (2004)]. However, astemizole and imipramine are not specific blockers for $K_v10.1$, since they also block K_v11 channels. A specific $K_v10.1$ blocker is the monoclonal antibody mAb56 that binds extracellularly to the pore loop between the 5th and 6th transmembrane domain and blocks the pore of the channel, thereby reducing $K_v10.1$ current without affecting the activity of other ion channels [Gómez-Varela et al. (2007)] (Figure 1C). It is believed that the Fab regions of the Y-shaped mAb, which contain the antigen targeting sites, bind onto two α -subunits of $K_v10.1$. This binding prevents gating of the channel, locking its structure in the open conformation, while the Fc region of the mAb obstructs the influx and outflux of K^+ through the pore of the channel.

1.2.4 Role

K_v10.1 expression seems to be limited to the adult human brain [Occhiodoro et al. (1998); Ludwig et al. (1994)], where it has a presynaptic localization and contributes to short-term synaptic plasticity, without taking part in somatic action potentials. *K_v10.1* is also localized in parallel fiber synapses in the cerebellar cortex, where it regulates Ca^{2+} influx and neurotransmitter release during repetitive high-frequency activity [Mortensen et al. (2014)]. *K_v10.1*-deficient mice on the other hand, show a mild hyperactivity [Ufartes et al. (2013)], while specific mutations of the *KCNH1* gene have been recently identified to cause Temple-Baraitser syndrome (TB Syndrome), a multi-system developmental disorder characterized by intellectual deficiency, epilepsy, and hypoplasia or aplasia of the nails of the thumb and great toe [Simons et al. (2014)]. *K_v10.1* is also expressed in myoblasts, where it contributes to the induction of cell differentiation, by contributing to their hyperpolarization [Bauer and Schwarz (2001)].

K_v10.1 has been widely studied because of its oncogenic potential, albeit its expected (and partially known) function in the nervous system. Initially, it was observed that transfection of cells with *K_v10.1* led to faster growth rates with concomitant loss of contact inhibition, characteristics typical for cancerous cells. Additionally, these transfected cells favor xenograft tumor progression in immunodeficient mice *in vivo*. [Pardo et al. (1999)]. A wider screening of *K_v10.1* expression revealed its presence in almost 70% of human tumor biopsies [Hemmerlein et al. (2006)], increasing the interest for this channel as a tumor marker. Moreover, the presence of *K_v10.1* does not seem to be limited only to solid tumors, where it seems to induce angiogenesis [Downie et al. (2008)], but has also been reported in leukemias and has been validated there as a prognosis factor for poor outcome [Agarwal et al. (2010)]. *K_v10.1* expression levels seem to correlate also with poor prognosis for ovarian [Asher et al. (2010a)], gastric [Ding et al. (2007a)] and colon [Ding et al. (2007b)] cancer patients as well as with the cancer phase in squamous cell [Menéndez et al. (2012)] and hepatocellular carcinomas [de Guadalupe Chávez-López et al. (2015)]. Although, in glioblastoma *K_v10.1* levels are lower than in healthy tissue [Patt et al. (2004)] and further silencing of channel expression favors responsiveness to IFN (interferon)- γ treatment [Cunha et al. (2013)]. Additionally, a number of studies have shown that *K_v10.1* expression induces proliferation of several cancer cell lines and *in vivo* tumor models, while blockage or silencing of the channel inhibits proliferation [Kong et al. (2014); Wu et al. (2013); Asher et al. (2011); Weber et al. (2006); Gómez-Varela et al. (2007)].

Due to the above-mentioned findings, *K_v10.1* has been proposed as an early cancer biomarker [de Guadalupe Chávez-López et al. (2015); D'Amico et al. (2013); Ortiz et al. (2011); Wulff et al. (2009); Pardo and Stühmer (2008); Hemmerlein et al. (2006); Pardo

et al. (2005)]. Moreover, its localization as a transmembrane protein, even though not the only one [Chen et al. (2011)], makes this channel an ideal drug target [Stühmer and Pardo (2010); Wilkinson et al. (2014); Pardo and Stühmer (2008); Huang and Jan (2014); García-Quiroz et al. (2014); D'Amico et al. (2013); Asher et al. (2010b)]. In fact, pharmacological blockage of $K_v10.1$ with astemizole (AST) and imipramine reduced cell proliferation *in vitro* [García-Quiroz et al. (2012); Kong et al. (2014); García-Ferreiro et al. (2004)], and *in vivo* AST reduced the progression and the metastatic ability of melanoma, pancreatic, lung, hepatocellular and mammary carcinomas [Downie et al. (2008); de Guadalupe Chávez-López et al. (2015)]. More specific approaches involved the blockage of the $K_v10.1$ channel with small interfering RNA, which reduced cell proliferation [Weber et al. (2006)], specific blockage with monoclonal antibody 56 (mAb56), which inhibited tumor cell growth [Gómez-Varela et al. (2007)], or even the specific apoptosis inducing molecule TRAIL (tumor necrosis factor-related apoptosis-inducing ligand), targeting only tumor cells positive for $K_v10.1$, by means of a single chain antibody against $K_v10.1$ [Hartung et al. (2011)].

$K_v10.1$ related tumorigenesis, does not seem to absolutely depend on the conducting properties of the channel [Kaczmarek (2006)]. Non-conducting $K_v10.1$ mutants can still increase cell proliferation and tumor growth [Pardo (2004); Downie et al. (2008)], pointing toward a non-conducting function of the channel that can rely on signaling cascades that may be recruited through protein-protein interactions (Figure 2). Indeed, the conformational changes at the voltage sensor of $K_v10.1$ can activate p38/MAPK kinase signaling, modulating cell proliferation [Hegle et al. (2006)]. Also the carboxyl- and amino-terminal of $K_v10.1$ expressed at the inner nuclear membrane, can interact with heterochromatin modulating gene expression [Chen et al. (2011)].

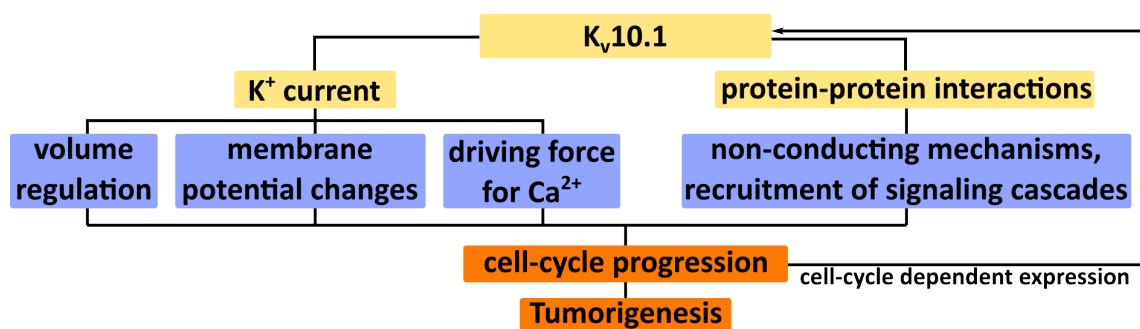


Figure 2 – The conducting and non-conducting properties of $K_v10.1$ ion channel can influence cell-cycle progression and tumorigenesis through volume regulation, membrane potential changes that also change the driving force of Ca^{2+} and through recruitment of signaling cascades. Cell-cycle progression can further influence $K_v10.1$ expression levels. Image modified by Urrego et al. (2014).

1.3 Cell migration

Cell motility is one of the most important cellular processes and along with other cell functions, is a requirement for the generation of new life, as well as for maintenance of the organism integrity [Schwab et al. (2008)].

1.3.1 Significance

During embryonic development, cell migration organizes morphogenesis. In gastrulation, large groups of cells migrate collectively in order to form the embryo. Afterwards, cells migrate from epithelial to target layers where they differentiate and form specific tissues and organs. Cell migration also occurs during wound healing and tissue repair, where cells migrate from basal to upper layers, as well as during immune responses, in which leucocytes migrate from the circulation to neighbor tissues in order to destroy invading organisms and infected cells. All these processes require a fine-tuned directed movement of cells [Lauffenburger and Horwitz (1996); Ridley et al. (2003); Becchetti and Arcangeli (2010)].

On the other hand, abnormal behavior or enhanced cell movement has been associated with severe pathological conditions, like tumor formation and metastasis [Zhu et al. (1999); Parsons et al. (2010)]. Therefore, the study of cell motility and migration, as well as of its underlying mechanisms, like cytoskeletal interactions and rearrangements, membrane formation and permeability, have received much attention over the last decades [Toral et al. (2007); Burnette et al. (2011); Ganguly et al. (2012)].

1.3.2 Types of cell migration

All migrating cells are morphologically but also functionally polarized along the direction of movement. The migrating cells form a lamellipodium [Abercrombie et al. (1971)] at their leading edge, a 300 nm thin, fan-like protruding membrane formation, while at the rear end the cell body may extend into an uropod, which finally retracts as the cell moves. The maintenance of this polarization, as well as the repetition of protrusion and retraction, will finally result in directed cell migration [Schwab et al. (2007)]. The complexity of this process depends on the type of the migrating cells, the number of dimensions where the migration occurs and the type of the extracellular matrix (ECM) surrounding the migrating cell. Every cell type displays a different type of migration behavior, although the same process (i.e. cell translocation) is executed, using specific molecular machinery and extracellular stimuli.

The different types of migration were originally classified based on cell morphology and migration pattern. Later approaches extended this terminology in order to include cy-

toskeletal organization and cell-substrate interactions [Friedl et al. (1998); Lämmermann and Sixt (2009)]. The main categories of cell migration are the individual cell migration (amoeboid or mesenchymal) and the collective one. The amoeboid migration refers to movement of round cells that lack mature focal adhesions and stress fibers and can be divided into two subtypes [Friedl et al. (2001); Lämmermann and Sixt (2009)]. The first one is the blebby movement of cells that do not really adhere, but rather push. The second subtype of amoeboid migration includes more elongated cells that form actin-rich filopodia (Figure 3). Some individually migrating cells adopt the mesenchymal type of migration, which is characterized by high levels of attachment, along with cytoskeletal reorganization and involves strong cell-substrate interactions and a fibroblast-like translocation [Kaye et al. (1971); Bergert et al. (2012)]. The migration type where individual cells form a limited number of cell-cell contacts during migration along a common path, is usually called multicellular streaming [Davis and Trinkaus (1981)]. Finally, the state where a well-attached cell population migrates along a common direction is referred to as the collective type of migration. In this case the cytoskeletal transformation is mainly located at the edges of this population or at the population-substrate interface. The collective type of migration occurs in different shapes (multicellular tubes, irregular masses or sheets) depending on the number of spatial dimensions, where the migration is taking place [Friedl and Gilmour (2009); Friedl and Wolf (2010)].

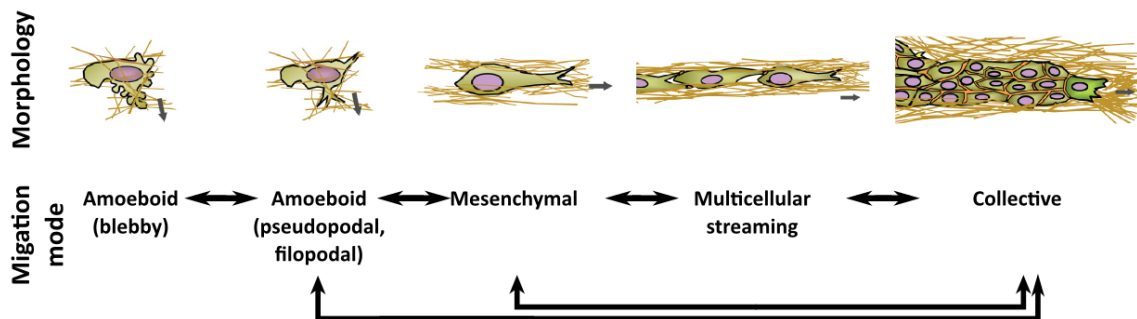


Figure 3 – The different types of migration modes are based on typical cell morphology (rounded or elongated) and pattern (individual, loosely connected or collective). A number of molecular mechanisms are responsible for each type of migration mode and the regulation of these mechanisms can alter the migration style. Most common and well-studied types of transitions are the mesenchymal-to-amoeboid or the collective-to-individual transition. The small gray arrows near the cells indicate the direction of migration. Image modified from Friedl and Wolf (2010).

The various migration types are part of the physiological behavior during morphogenesis and tissue repair but may also take part in promoting a pathology. Collective migration is essential during tissue building and reformation, but may also be important to cancer progression with local invasion into neighboring tissues [Friedl and Gilmour (2009)]. In contrast, individual migration is important when cells need to translocate locally or migrate in different locations throughout the body, as in the case of immune

trafficking [Lämmermann and Sixt (2009)]. This individual migration seems to be crucial also during cancer metastasis [Thiery (2002)].

While the determinants for each type of migration are not completely understood, specific parameters have been identified as factors that can maintain certain migration behaviors, or induce transitions from one type of migration to another. These parameters are related to the ECM architecture, to molecules responsible for cell-cell or cell-surface adhesion, to the cytoskeletal organization and to the ECM proteolytic activity of the migrating cells [Friedl and Wolf (2010)]. However, there are a number of factors that on their own cannot alter the overall migration behavior, but are able to change specific migration pattern characteristics, such as speed, directionality and the straightness of cell trajectories. These factors, among others, include membrane proteins like integrins and ion channels [Becchetti and Arcangeli (2010); Schwab et al. (2012)], cytoskeleton proteins [Schwartz and Horwitz (2006); Toral et al. (2007)], cellular structures like primary cilia [Christensen et al. (2008)], or even extrinsic factors, like the effect of light sources or medium composition [Yu et al. (2003); Babich et al. (2009)].

1.3.3 Ion channels and cell migration

An important aspect during cell migration is cell-volume regulation. In a migrating cell, the volume between the swelled-protruding front part and the shrinking-retracting back part changes continuously. Ion channels play an important role in this volume regulation [Lang et al. (1998)]. Sequentially, cell volume changes are essential for actin cytoskeleton polymerization and depolymerization [Pedersen et al. (2001)], while cytoskeletal components on their turn regulate ion channels behavior [Grunnet et al. (2002)], completing the bilateral relation between cell volume regulation and ion channel activity during cell migration. Additionally, ion channels regulate intracellular Ca^{2+} concentration, which is crucial for cell migration [Pettit and Fay (1998)]. The role of ion channels in cell migration has been studied in detail over the last decades, as revealed by several extended reviews [Schwab et al. (2012); Stock et al. (2013)].

Potassium channels also modulate cell migration [Schwab et al. (2008)]. Their main function is to control the driving force available for ion transport across the plasma membrane, which is essential for the regulation of Ca^{2+} ion concentration during migration [Pettit and Fay (1998)]. Early on it was shown that a depolarized cell membrane potential can inhibit migration of epithelial cells [Schwab et al. (1994)]. Potassium channels also participate in cell volume [Hoffmann and Pedersen (2006)] and cytoskeleton activity regulation, which is interrelated with ion channels activity. It has been shown that potassium channels stereochemically interact with proteins, which are related to cytoskeleton activity that are important for cell migration. These interaction partners include integrins

[Arcangeli and Becchetti (2010); Cherubini et al. (2005); Pillozzi and Arcangeli (2010)], cortactin [Herrmann et al. (2012); Sung et al. (2011)] and focal adhesion kinase (FAK) [Zhao and Guan (2011); Mitra et al. (2005)].

$K_v10.1$ has also been implicated in the regulation of cell migration [Restrepo-Angulo et al. (2011)]. Moreover, $K_v10.1$ regulates the migration speed by controlling Ca^{2+} entry through Orai1 channels [Hammadi et al. (2012)]. However, even though $K_v10.1$ is a well-studied member of the K_v channel family, its role in cell migration is not really known.

1.3.4 Primary cilia

The primary cilium is a singular organelle that arises from the cell surface of most mammalian cells during their growth arrest phase [Sorokin (1968)]. It consists of an axoneme of nine doublet microtubules that extends from the basal body, surrounded by the ciliary membrane (a specialized part of the cell membrane). The basal body is derived from the mother centriole of the centrosome. Primary cilia are considered to be the coordinators of signaling pathways during development and tissue homeostasis [Satir et al. (2010)], while ciliary dysfunction can lead to a number of developmental abnormalities and diseases (ciliopathies). The fact that primary cilia are present during the cellular G_0 phase, suggests an important role in growth control and cell cycle regulation. Moreover, the orientation of primary cilia in cultured fibroblasts seems to be related with migration, since cilia are aligned in parallel with the intended direction of migration [Albrecht-Buehler (1977); Wheatley (1971)]. Primary cilia appear to have the role of an antenna [Seeger-Nukpezah and Golemis (2012); Singla and Reiter (2006)], sensing (mechanically and chemically) the cell surrounding and coordinating signal transduction to a number of biochemical pathways [Christensen et al. (2008); Hassounah et al. (2012)]. This signaling coordination appears to be important for cell-cycle control [Basten and Giles (2013)], cancer and tumorigenesis [Basten and Giles (2013); Michaud and Yoder (2006)], as well as for directional cell migration [Schneider et al. (2009, 2010)].

1.4 Cell-cell adhesion

Cell-cell adhesion is responsible for the generation of functional tissues and organs, for the functionality of the nervous system and for the overall maintenance of multicellular organisms. Conversely, failure of cell-cell recognition and adhesion can generate defective individual cells or even metastatic ones during cancer. Essential for the correct recognition and maintenance of cell-cell adhesion is the expression and organization of specific molecules on the cell membrane [Damsky et al. (1984)]. Indeed, a family of glycoproteins named cadherins, has been proposed to be involved in the Ca^{2+} dependent cell-cell adhesion of most types of tissues. It has been suggested that cadherins bind cells

using their extracellular domains, while their cytoplasmic domains associate with actin bundles [Takeichi (1988)]. Clustering of cadherins and accompanying structural changes of the cytoskeleton lead to stronger cell-cell adhesion. Additionally, cadherins appear to interact with the cytoskeleton through a family of cytoplasmic proteins named catenins. This cadherin-catenin complex is involved in the regulation of cell-cell adhesion [Nelson (2008)]. Moreover, the regulation of cell-cell adhesion through alterations in the complex of cadherin-catenin seems to be crucial during cell migration [Le Bras et al. (2012)], since it can modify the epithelial-mesenchymal transition [Le Bras et al. (2012); Friedl and Wolf (2010)] and also promote tumorigenesis [Rodriguez et al. (2012)].

Despite the central role of cell-cell adhesion in cell migration and cancer on one hand, and the role of the potassium ion channels in cell migration, tumorigenesis and metastasis on the other hand, the relation of ion channels to cell-cell adhesion regulation has not been studied so far. In this thesis I present evidence on the localization of $K_v10.1$ in the cell-cell interface and its implication in the regulation of cell-cell adhesion.

1.5 Cell-surface adhesion

Cell-surface adhesion is a well-studied process of fundamental importance in physiology and pathology, which has been studied for over 40 years [Abercrombie and Dunn (1975)]. Cell proliferation and differentiation, together with surface adhesion, depend on the cell-ECM interface [Bacakova et al. (2011); Sheetz (2001)]. Additionally, the invasive ability of cancer cells is highly dependent on their adhesive behavior, which on turn controls migration [Friedl and Wolf (2003)]. Especially during cell migration, the dynamic formation and deformation of adhesions is considered to be the driving force of migrating cells [Webb et al. (2002); Krause and Gautreau (2014)].

Moreover, cell-surface adhesion is coupled with processes like actin polymerization and myosin II-generated tension [Parsons et al. (2010)] and is responsible for the determination of the cell migration type [Friedl and Wolf (2010)]. Adhesion related molecules, like integrins, have been shown to physically interact with ion channels in general [Arcangeli and Becchetti (2006, 2010); Becchetti and Arcangeli (2010); Pillozzi and Arcangeli (2010)], modulating migration and metastatic ability of cells. Additionally, FAK, which regulates adhesion dynamics [Webb et al. (2004); Mitra et al. (2005)], is also implemented in cell motility and migration [Chalkiadaki et al. (2009); Zhao and Guan (2011); Mitra et al. (2005)] and together with the cytoskeleton participates to cell volume regulation [Pedersen et al. (2001)].

Based on all these studies, we can conclude that cytoskeletal processes, volume regulation, ion channel activity, cell migration and cell-surface adhesion, are all intimately interrelated processes.

1.6 Acquisition settings and cell migration

Lasers have been used for therapeutic purposes, such as wound healing [Lucas et al. (2002)] and tissue regeneration [Amaral et al. (2001)], for eliminating unwanted structures and cells [Jay and Sakurai (1999); Surrey et al. (1998)] or even to block specific processes [Jacobson et al. (2008); Surrey et al. (1998)]. In many studies, the effects of laser light have been related to the energy level [Hawkins and Abrahamse (2005)] and the wavelength used [Dadras et al. (2006); Chung et al. (2012)].

In the case of light microscopy, and especially in live imaging experiments, the use of laser light excitation has offered great advantages for monitoring specific cellular structures and processes. However, it has been known to alter cell physiology during live imaging by altering processes such as cell proliferation [Hu et al. (2007); Yu et al. (2003); Ejiri et al. (2013); McDonald et al. (2011)] and cell migration [Yu et al. (2003); Ejiri et al. (2013); Swen et al. (2002); Chen et al. (2008)]. For this reason, in the case of time-lapse fluorescence imaging with confocal microscopes, the optimized fluorochrome excitation, as well as the optimization of emitted photons collection, is essential in order to avoid photodynamic damages and cell behavior alterations [Stephens and Allan (2003); van de Linde et al. (2012); Frigault et al. (2009); North (2006); Dailey et al. (2006, 2011)].

In the case of the scratch assay, the majority of studies usually apply phase contrast images acquired at the beginning and at the end of the cell migration process. However, in order to monitor cell migration in detail, time-lapse imaging is needed. Lately, there has been an upsurge in the need for monitoring fluorescently tagged live cells in a dynamic manner [Dailey et al. (2006)]. In these cases, the establishment of a favorable compromise between the maximum and frequent collection of photons and the minimum phototoxicity is essential.

A major point of interest in fluorescence microscopy is the increase of the acquired fluorescence signal. Some common approaches are to increase excitation intensity, or to accumulate emitted photons from sequential scans of the samples, while maintaining low excitation intensity. Both of these approaches though, may lead excited fluorochromes to be trapped in higher energy states that are not directly related to the excitation-emission cycle ($S_0 \rightarrow S_1 \rightarrow S_0$, Jablonski diagram in Figure 4). In these states, like the $S_{n>1}$ singlet state or the T_1 and $T_{n>1}$ triplet states, the fluorochromes are not contributing to the fluorescence signal, but may instead be responsible for adverse reactions like photobleaching [Eggeling et al. (1998); Anbar and Hart (1964)], for the generation of free radicals [Wojtovich and Foster (2014); Clough and Buenger (1995); Pattison and Davies (2006)] and for other phototoxic effects [Vargas et al. (1998); Tinevez et al. (2012); Magidson and Khodjakov (2013); Kolega (2004); Hoebe et al. (2008)].

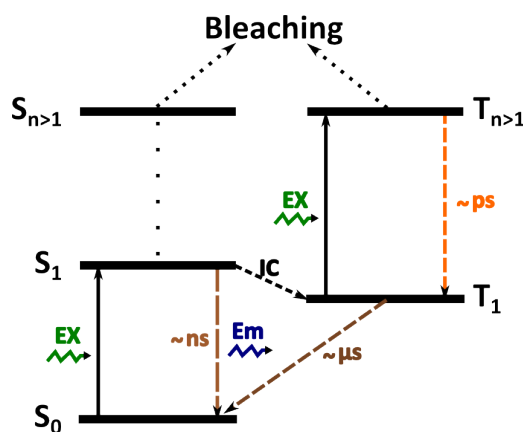


Figure 4 – Jablonski diagram showing the major photochemical pathways for excitation (EX-green), emission (Em-blue), intersystem crossing (IC), relaxation (color coded dashed lines) and photo-bleaching (bleaching). $S_0, S_1, S_{n>1}$ are single while T_1 and $T_{n>1}$ are triplet states of a fluorochrome. The excitation of T_1 and $S_{n>1}$ states are effective bleaching pathways.

Many techniques have been established to prevent these unwanted effects, e.g., by using photo-protective chemical compounds [Kim et al. (2009); Singh et al. (2006); Alberto et al. (2013); Sung et al. (2012)], by changing the medium composition [Bogdanov et al. (2012, 2009)], or by using more effective acquisition settings [Watkins and St Croix (2013); Swedlow et al. (2009); North (2006)]. The most efficient ones seem to be those where excitation repetition does not match the fluorochrome relaxation time from the higher energy states [Donnert et al. (2009, 2007)]. In these studies, triplet state relaxation (T-Rex) and dark state relaxation (D-Rex) modes improved photo-stability and signal intensity. However, to the best of our knowledge none have used these approaches in cell migration studies in combination with the scratch assay.

1.7 Scratch assay

The scratch assay (or wound healing assay) is a well-accepted low-cost method to stimulate and study migration of a confluent monolayer of cells *in vitro*. To some degree, this method imitates *in vivo* cell migration, is very reproducible and is commonly used to measure parameters such as speed, polarity and directionality of migrating cells [Liang et al. (2007)]. After scratch initiation, cells migrate towards the newly generated, cell-free gap. The cause of this reaction relies on a complex network of cellular functions (proliferation [Zahm et al. (1997); Coomber and Gotlieb (1990)] and adhesion [Parsons et al. (2010); Toral et al. (2007)]) and structures (cytoskeleton [Ganguly et al. (2012); Wong and Gotlieb (1988)], cell membrane and transmembrane proteins [Becchetti and Arcan-geli (2010); Seeger-Nukpezah and Golemis (2012); Camacho et al. (2000)]), as well as molecular processes [Lauffenburger and Horwitz (1996); Rahnama et al. (2006)] and biochemical pathways [Chalkiadaki et al. (2009); Cabodi et al. (2009)]. Due to this wide

variety of processes and pathways involved, but also due to the experimental simplicity, the scratch assay has been extensively used with a broad range of adherent cells. Moreover, chemotaxis is central to scratch closure [Devreotes and Janetopoulos (2003)] and so the scratch assay does not require additional chemoattractants or gradient chambers to elicit a directional cell migratory response. As such, can easily be applied to study the above mentioned functions and processes during cell migration [Stock et al. (2013); Schwab et al. (2008); Devreotes and Janetopoulos (2003)]. Chemotactic assays focus on specific cytokines and involve the study of respective receptors. In contrast, in scratch assays, with the presence of FCS-containing medium, all present cytokines (like EGF, FGF, VEGF) as well as integrin mediated signaling (for adherent cells), can induce cell polarization, alter actin dynamics and also affect the chemotactic migration during wound healing. Thus, the scratch assay can easily be applied to monitor cell migration behavior through time-lapse, live-imaging microscopy. As such, chemotaxis has been implicated in cancer metastasis [Condeelis et al. (2001); Gangur et al. (2002); Murphy (2001); Moore (2001); Müller et al. (2001)], especially through chemokines and their receptors. Therefore, the scratch assay is particularly suitable for the study of the regulation and/or dependency of cell migration on cell-cell and cell-surface interactions. It also can be used to extract information about directionality, speed and displacement of individual cells or from an entire cell population and moreover, to monitor cell divisions as an indicator of cell proliferation, especially in the context of cancer and tumor metastasis.

There are several variations of the wound healing assay, that differ especially the manner in which the live cells are monitored [Stephens and Allan (2003)]. Traditionally, it was performed by acquiring either phase or differential interference contrast (DIC) images at specific time points after the initiation of the scratch (time points 0h, 6h, 12h etc.). Then, the quantification of the migration was expressed as the mean, reduced scratch area over time [Liang et al. (2007); Cory (2011)]. However, in order to acquire more detailed information, especially for individual cells during gap closure, time-lapse live cell imaging must be used with either DIC or fluorescent light (in stained cells) [Cory (2011)], at different time intervals dependent on the experimental requirements. This acquisition for wound healing assays using fluorescent light is lately widely used.

1.8 Interference reflection microscopy

Interference reflection microscopy (IRM), was first introduced in cell biology by A. Curtis back in 1964 [Curtis (1964)]. Since then, numerous researchers have applied IRM to study cell adhesion to glass surface without the requirement of any stain.

1.8.1 IRM principle

The generation of an IRM image relies on the interference of the reflected light waves from the sample (Figure 5). As the light travels through the sample, it is reflected at interfaces between media of different refractive indices (n). The reflection coefficient (r) at the boundary between the media with refractive indices n_1 and n_2 is given by Fresnel's equation 1.

$$r_{12} = \frac{n_1 - n_2}{n_1 + n_2} \quad (1)$$

The reflectivity (R), which is the ratio between the reflected (I_r) and the incident (I_o) wave intensity, is given by equation 2:

$$R = \frac{I_r}{I_o} = \left[\frac{n_1 - n_2}{n_1 + n_2} \right]^2 = r_{12}^2 \quad (2)$$

When a cell is growing on a glass surface, then the first reflection takes place at the glass-to-medium interface. Since the difference of the refractive indices of glass and culture medium is relatively large, a strong reflection will result (wave 7 and pixel intensity e in Figure 5). Conversely, when a cell membrane touches the glass surface (a rare event), then the difference between the refractive index of the glass and the cellular membrane, is minimum due to the lack of imaging medium, causing low reflectivity and results in a dark area in the produced image (wave 1 and pixel a in Figure 5). When medium is present between the glass surface and the cell membrane, then reflections will be present at the glass-medium and medium-membrane interfaces (waves 2 and 3 or 4 and 5, respectively in Figure 5). The reflected waves can interfere, if the thickness of the medium film is of the order of magnitude of the used wavelength [Verschuere (1985)]. In such a case, the optical path difference Δ between the two reflections is $\Delta = 2 \cdot n \cdot h \cdot \cos \theta$, where n is the refractive index of the medium, h is the vertical distance between the glass and the membrane and θ is the angle of refraction in the medium.

The image will contain a dark pixel if $\Delta = N\lambda$, and a bright one if $\Delta = \left(N + \frac{1}{2}\right)\lambda$, where N is the order of interference. That means that all these reflections contain information about the cell-substrate distance, since the grade of interference, as visualized by different pixels intensities (pixels b and c in Figure 5), is dependent on this distance.

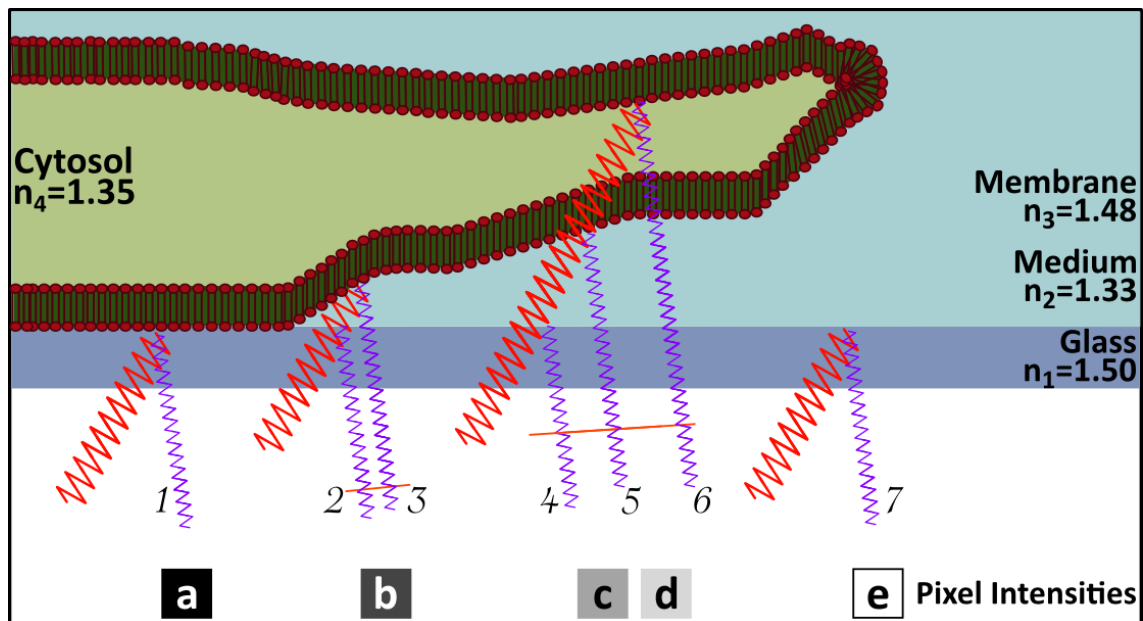


Figure 5 – Principle of IRM showing the interference effect of reflected waves and the resulting pixel intensity. The red wavy line represents light coming from the light source. Purple waves are the reflections from different interfaces. The grade of interference (see red lines) of reflected light waves is depending on the distance between the subsequent interfaces. If the distance is small, then the interference is more efficient resulting in a dark pixel (b). If the distance is bigger, then the interference is lower and the pixel intensity is brighter (c). Indicated are the typical refractive indices of the glass, medium and the cell membrane, which determine the amount of reflection.

However, the resulting images can be much more complex, since there can be reflections from other interfaces as in the case of the dorsal cellular membrane (wave 6 in Figure 5). These reflections can interfere with reflections from the lower interfaces, contributing to the resulting pixel intensities and in this case no conclusions can be made about the distances between the glass and the membrane [Gingell and Todd (1979)]. This drawback can be overcome with the use of objectives with high numerical aperture (NA). Since the optical path length Δ between glass surface and cellular membrane is related to the angle of refraction in the medium (ϑ), the broad range of angles of incidence within the illuminating cone, produced with high NA, results in a continuous series of overlapping interference patterns, which cancel out each other almost entirely [Verschueren (1985)]. These overlapping patterns converge only for the zero-order fringes (where Δ is smaller than one λ) and the intensity of the resulting image is increasing as the distance increases from 0 to approximately 100 nm [Izzard and Lochner (1976); Verschueren (1985); Choi et al. (2008); Limozin and Sengupta (2009)]. The use of high NA values reduces the depth of focus (DoF) as shown by equation 3 [Choi et al. (2008)], where λ is the wavelength used, n is the refractive index of the immersion medium and NA the numerical aperture of the objective.

$$DoF = \frac{\lambda}{4n \left(1 - \sqrt{1 - \left(\frac{NA}{n} \right)^2} \right)} \quad (3)$$

If the NA values used are greater than 1 and if cell thickness is not less than 100 nm, then the image is formed only from zero-order interferences giving information on cell-substrate distances in the range of 100 nm [Verschueren (1985); Choi et al. (2008)].

1.8.2 Quantification

As has been shown previously, a monochromatic incident wave (red waves in Figure 5) is first reflected by the glass to medium interface (reflected wave 2 in Figure 5) and then by the medium-membrane interface (wave 3 in Figure 5), giving rise to rays I_1 and I_2 i.e. These two rays can interfere and the intensity I of the resulting pixel (b in Figure 5) can be given by equation 4.

$$I = I_1 + I_2 + 2\sqrt{I_1 I_2} \cos[2kh(x,y) + \phi] \quad (4)$$

where $k = \frac{2\pi n}{\lambda}$ (with n being the refractive index of the medium and λ the wavelength of the incident light), ϕ is the phase shift normally equal to π and h is the distance between the membrane and the glass substrate at the lateral position (x,y) . The intensities I_1 and I_2 depend on the incident intensity I_0 as described in equation 2 based on Fresnel's reflection coefficient (equation 1).

Equation 4 can be written in a simpler form, using $\phi = \pi$ and the sum and the difference of the maximal ($I_{max} = I_1 + I_2 + 2\sqrt{I_1 I_2}$) and minimal intensity ($I_{min} = I_1 + I_2 - 2\sqrt{I_1 I_2}$) as follows:

$$2I = (I_{max} + I_{min}) - (I_{max} - I_{min}) \cdot \cos\left(\frac{4\pi n h}{\lambda}\right) \implies \quad (5)$$

$$\implies h = \frac{\lambda}{4\pi n} \cdot \cos^{-1}\left(\frac{I_{max} + I_{min} - 2I}{I_{max} - I_{min}}\right) \quad (6)$$

Equation 6 can be used to calculate the membrane proximity to the glass substrate, since the I_{max} and I_{min} are experimentally measurable. This equation can be used as long as the above mentioned conditions (NA values above 1 with low DoF, cell thickness and membrane distance from surface below the range of 100 nm) exist.

1.9 TIRF

Total internal reflection fluorescence (TIRF) is a microscopy technique for collecting fluorescence exclusively from interfaces between cells and substrate. TIRF utilizes a low

dose of diffuse incident light that illuminates the entire field of view within a thin layer of around 100 nm from the substrate [Axelrod (1981)]. This technique is ideal for both live-cell imaging and studies of cell migration and adhesion, since it provides high contrast images with nonexistent out-of-focus light [Lacoste et al. (2013)] and also causes low phototoxicity.

2 Materials & Methods

2.1 Cell lines manipulation

2.1.1 Cell lines

HeLa SS6 (kind gift by Prof. Mary Osborn, Göttingen; [Elbashir et al. (2001)]) and HT-1080 (DSMZ, Hannover; [Rasheed et al. (1974)]) cells were used for immunofluorescence stains and transient or stable expression of either EGFP-actin, EGFP-K_v10.1, K_v10.1-DsRed2, mVenus or K_v10.1-mVenus encoding vectors. These cells were maintained and propagated according to provider's instructions.

Dr. M. Mitkovski had previously performed all the experiments with HeLa cells, before the start of this study.

2.1.2 Normal culture

HT-1080 cells were routinely cultured in T25 or T75 flasks (Sarstedt) and incubated in a CO₂ humidified incubator at 37°C and 5% CO₂ until they reach 80-90% confluence. Then, the culture medium was removed and cells were washed with 5 ml PBS (or 10 ml in the case of T75 flasks). The cells were then detached with 0.5 ml (or 1 ml for T75 flasks) Trypsin/EDTA solution (0.05%/0.2% (w/v) in PBS without Ca²⁺/Mg²⁺, Biochrom), for 2 min at 37°C and then resuspended in 5 ml pre-warmed culture medium, transferred in sterile tubes (Greiner Bio One) and centrifuged for 2 min at 290 g at room temperature (RT). Then the supernatant was removed and the cell pellet was resuspended in 1 ml (per initial T25 flask used) culture medium. From this resuspension, 50-150 µl (according to the desired dilution) were transferred into a new T25 flask with 5 ml of fresh culture medium (or 250-400 µl into a T75 flask with 10 ml medium), supplemented by 0.5 mg/ml G₄₁₈ antibiotic (Life Technologies, Darmstadt) as an additional selective pressure to maintain the stable cell lines. Then, cells were kept at 37°C and 5% CO₂ in a humidified environment until confluency.

In the cases where special cell density was needed, cells were counted with a Neubauer slide (Laboroptik Ltd-UK). 10 µl of resuspended cells were added on the slide and 4 big squares of the Neubauer slide were counted. The total cell density (per ml) was then calculated, by dividing the counted number by 4 and multiplying by 10⁴. Then, the appropriate amount of volume was used in order to seed the desired cell density.

For the freezing of cells, approximately 10⁶ cells were resuspended in 500 µl of culture medium and placed into a cryovial (Greiner Bio One) containing 225 µl of DMEM, 150 µl of FCS and 125 µl of DMSO (Sigma). Then, the cryovials were placed at approximately 0°C for 10 minutes and then at -80°C for at least 24 h. Afterwards, they were transferred

in liquid nitrogen for permanent storage. In order to start a culture from frozen cells, the cryovials were removed from the liquid nitrogen, and placed into a water bath at 37°C for 1-2 min. Then, their content was added in 10 ml of pre-warmed culture medium and centrifuged at 290 g for 2 min. Afterwards, the supernatant was removed, the cell pellet was resuspended in 5 ml of medium containing 0.5 mg/ml G₄₁₈ antibiotic and the mixture was added into a new T25 flask.

2.1.3 Transfection

HT-1080 cells were stably transfected with mVenus or K_v10.1-mVenus encoding vectors and placed under further G₄₁₈ antibiotic selection. The expected molecular weight of the mVenus protein is at 24 kDa while the one of the chimeric K_v10.1-mVenus is at 134 or 154 kDa depending on the glycosylated isoform of the channel [Napp et al. (2005)]. The stable transfection of HT-1080 cells occurred before the start of this study and performed by Dr. Mitkovski using Lipofectamine[®] 2000 Transfection Reagent (Invitrogen) according to manufacturer's instructions.

2.1.4 Cell Sorting

The transfected HT-1080-mVenus and HT-1080-K_v10.1-mVenus cells were sorted based on their fluorescence intensity, using a FACS Aria[™] flow cytometer (BD Biosciences). For the excitation of the mVenus fluorochrome the 488 nm Argon laser was used, while the emission was collected using 530/30 BP filter. A gating around the cell population (excluding debris and cell clumps) was used based on the forward and side scatter of the cells. With this gating both types of transfected cells were sorted based on different fluorescence intensities, into three populations; low fluorescence (LF), high fluorescence (HF) and very high fluorescence (VHF). For all the following experiments (unless otherwise stated) we used the HF population of HT-1080-mVenus cells and the VHF population of HT-1080-K_v10.1-mVenus cells. For the data acquisition the BD FACS-Diva[™] software (version 5.0; BD Bioscience) was used.

Dr. M. Mitkovski performed the sorting of the transfected cell lines, before the start of this study.

2.2 Electrophysiology

For electrophysiological experiments, sorted HT-1080-K_v10.1-mVenus cells of different fluorescence intensities, were grown for 24 h before the experiment on poly-L-lysine-coated glass coverslips. Macroscopic currents were recorded at room temperature in the whole-cell configuration of the patch-clamp technique [Hamill et al. (1981)] using an

EPC-9 amplifier and Pulse software (HEKA). Patch pipettes with a tip resistance of 1.5 to 2 M Ω were made from Corning no. 0010 capillary glass (WPI) and series resistance was compensated by 70%. The internal solution contained 100 mM KCl, 45 mM N-Methyl-D-Glutamine, 10 mM 1,1-bis(O-aminophenoxy)ethane-N, N, N', N'-tetraacetic acid (BAPTA) tetrapotassium salt, 10 mM HEPES/HCl, pH 7.35 and the external solution contained 160 mM NaCl, 2.5 mM KCl, 2 mM CaCl₂, 1 mM MgCl₂, 8 mM glucose, 10 mM HEPES/NaOH, pH 7.4. The cells were held at -60 mV and a voltage step of 20 mV over the range of -100 to -40 mV with 1600 ms durations was applied. The cell was then depolarized to +40 mV to activate K_v10.1 current.

The electrophysiology experiment was performed by Dr. Ye Chen, before the start of this study.

2.3 Molecular biology

Total RNA was extracted from HT-1080 cells stably expressing either mVenus or K_v10.1-mVenus using QiaShredder columns from Qiagen and purified with the RNeasy Mini kit of Qiagen (Qiagen, Hilden, Germany). Then, the purified total RNA was reverse transcribed with the SuperScript[®] reverse transcriptase (Invitrogen, Karlsruhe, Germany) to cDNA, which was used for the quantification of the expression levels of K_v10.1 ion channel with the appropriate primers in a LightCycler[®] 480 (Roche Diagnostics Deutschland GmbH, Mannheim, Germany) real time PCR instrument.

2.3.1 RNA purification

Approximately $6 - 7 \cdot 10^6$ HT-1080-K_v10.1-mVenus and HT-1080-mVenus cells were used for the extraction of total RNA. The cells were scrapped from the flasks, collected in culture medium, centrifuged at 290 g and washed once with ice cold PBS. Then, the cells were collected after centrifugation at 290 g and after removal of the PBS they were disrupted by addition of 600 μ l RTL Buffer with 1% (v/v) β -mercaptoethanol. For the homogenization, a 25G needle was used. The homogenate then passed through QiaShredder columns (Qiagen, Cat. Nu.: 79656) with centrifugation for 2 min at 16000 g. One volume (600 μ l) of ethanol (70% in DEPC-H₂O) was added at the lysate and from that mixture approximately 700 μ l were added to RNeasy mini columns (Cat. Nu.: 74106), following manufacturer's instructions. For the elimination of genomic DNA contamination, our samples were treated with DNase for 30 min at RT. Finally, the purified RNA was eluted in 30 μ l of RNase free DEPC water, and was stored at -80°C or processed immediately with the cDNA synthesis protocol.

2.3.2 Reverse transcriptase PCR

For the cDNA synthesis, 2.5 µg of purified RNA were processed with the use of SuperScript® First-Strand kit from Invitrogen. A negative control sample was also used for each sample in order to validate for genomic DNA contamination. For each sample and negative control, we added 0.5 µg of oligo (dT) and also DEPC-H₂O to a final volume of 12 µl. Samples and negative controls, were vortexed gently and centrifuged shortly, before incubated at 70°C for 10 min. Afterwards, they were cooled for 1 min on ice and 7 µl of RT Reaction buffer were added. The mixture was incubated for 5 min at 42°C. The RT Reaction buffer for each sample contained the following:

| RT Reaction Buffer |
|------------------------------------|
| 2 µl 10x RT Buffer |
| 2 µl MgCl ₂ 25mM |
| 1 µl dNTPs 10mM |
| 2 µl of dithiothreitol (DTT) 0.1 M |

Table 1 – Reverse Transcription Reaction Buffer

Samples were then supplemented with 1 µl (200 units) of reverse transcriptase and negative controls with 1 µl DEPC-H₂O. The mixtures were then incubated at 42°C for 50 min and then at 70°C for 15 min in order to inactivate reverse transcriptase. For the digestion of the remaining RNA, 2 units of RNase enzyme were used and each reaction tube was incubated at 37°C for 20 min. Finally 4 µl of DEPC-H₂O were added at each sample and negative control, for a final volume of 25 µl and a final cDNA concentration of 100 ng/µl.

2.3.3 Real-time PCR

The resulting cDNA, as well as the calibrator cDNA (derived from human total brain and CNS RNA, Clontech Laboratories, Inc., USA) were used as template for the relative quantification of the *KCNHI* gene expression. Real-time PCR was performed using the Hydrolysis probe (TaqMan) technology in a LightCycler® 480. The primers used for the amplification of the *KCNHI* gene (exon 6) were: 5'-TCTGTCCTGTTTGCCATATG-ATGT-3' (forward), 5'-CGGAGCAGCCGGACAA-3' (reverse), while the detection probe was: 5'-(FAM)-AACGTGGATGAGGGCATCAGCAGCCT-(6-Tamra)-3'. The transferrin receptor encoding gene was also amplified in parallel as a reference with: 5'-GACT-TTGGATCGGTTGGTGC-3' (forward primer), 5'-CCAAGAACCGCTTTATCCAGAT-3' (reverse primer), and was detected with: 5'-(Joe)-TGAATGGCTAGAGGGATACCTTTC-GTCCC-(6-Tamra)-3' probe.

The PCR protocol used, included an initial incubation for 2 min at 50°C and for 10 min at 95°C, then 50 cycles of 10 sec at 95°C (denaturation), 15 sec at 56°C (annealing) and 60 sec at 60°C (extension) and a final cooling step of 30 sec at 40°C.

For the analysis of the results, the LightCycler analysis software (version 1.50Sp4) was used. All the target/reference ratios were normalized with the target/reference ratio of the calibrator sample, while no efficiency-correction for this run was used.

The Real Time PCR experiment was performed with the kind help of Mrs. U. Kutzke.

2.4 Biochemistry

2.4.1 Protein extraction

Total protein was extracted from approximately 90% confluent T75 flasks with HT-1080-mVenus and HT-1080-K_v10.1-mVenus cells. Cells were washed twice with ice cold PBS, scraped off the flasks with 10 ml PBS and centrifuged at RT for 2 min at 800 g. Then the supernatant was discarded and the pellet was washed twice with ice cold PBS. Finally, the cell pellet was resuspended in 400 µl lysis buffer [50 mM Tris-HCl pH 7.4; 300 mM NaCl; 5 mM EDTA; 1% Triton X-100; a tablet of complete protease inhibitor (PI) cocktail (Roche) per 10 ml solution] and the homogenate was incubated on ice for 20 min. After the incubation, the lysates were centrifuged for 15 min at 16000 g and the supernatants were carefully transferred into new tubes and stored at -20°C or used for downstream application.

2.4.2 Protein quantification

Diluted (1:5) protein extracts were quantified with the Pierce BCA protein assay kit (Cat. Nu.:23225; Thermo Scientific). 7 µl of total proteins extracted with the previous procedure were diluted with 28 µl of ddH₂O and 10 µl of this mixture was loaded in triplicates on a 96 well plate. On this plate were added, also in triplicates, 10 µl of the BSA (bovine serum albumin) standards, diluted as shown in Table 2.

| <i>Vial</i> | <i>dH₂O</i> (μ l) | <i>BSA</i> (μ l) | <i>Concentration</i> (μ g/ μ l) |
|-------------|-----------------------------------|-----------------------|--|
| A | 0 | 35 | 2 |
| B | 17.5 | 52.5 | 1.5 |
| C | 35 | 35 | 1 |
| D | 30 | 30 from B | 0.75 |
| E | 35 | 35 from C | 0.5 |
| F | 35 | 35 from E | 0.25 |
| G | 30 | 30 from F | 0.125 |
| H | 32 | 8 from G | 0.0025 |
| I | 60 | 0 | 0 |

Table 2 – BSA dilution scheme used for protein quantification

The working solution (WS) was prepared by dilution of Reagent B (4% cupric sulfate) 1:50 in Reagent A (sodium carbonate, sodium bicarbonate, bicinchoninic acid and sodium tartrate in 0.1 M sodium hydroxide). 200 μ l of this WS was added in each well with standards or samples, and the plate was incubated at 37°C for 30 min. The absorbances were measured at 562 nm with a Wallac VICTOR2 plate reader (Perkin Elmer) and with the titration curve from the standards we were able to calculate the extracted total protein concentration of our samples.

2.4.3 SDS-PAGE protein separation

For the electrophoretic separation of the extracted proteins under mild denaturation, we used a 10% Li-SDS gel. The gel mixture was made by 4.45 ml ddH₂O, 2.25 ml of 4x Buffer (1.5 M Tris/HCl, pH 8.8; 0.4% Li-SDS), 2.25 ml of 40% AA/bis-AA (Acrylamide-/Bis-Acrylamide) (29:1; BioRad), 4.5 μ l TEMED 100% and 45 μ l APS 10%. The liquid mixture was put between two glass surfaces and left for 30-45 min at RT in order to polymerize.

Protein extracts from HT-1080-mVenus and HT-1080-K_v10.1-mVenus cells as well as a ladder (Precision Plus Protein™, All Blue Standards; Bio-Rad Laboratories, Inc.) were loaded in different concentrations at the gel. Specifically, 5, 10 and 20 μ g of total protein extract from HT-1080-mVenus cells and 40, 50 and 60 μ g from HT-1080-K_v10.1-mVenus cells were loaded. The electrophoresis took place for approximately 150 min under 100 mVolts.

2.4.4 Fluorescent detection from gel

The fluorescence signal from the mVenus protein (expressed in both types of HT-1080 cells), was detected using a GE Typhoon Trio™ imager (Amersham Biosciences Corp).

The gel was imaged upon 488 and 633 nm excitation generated by an Argon and He-Ne laser, respectively. For the detection of mVenus fluorescence the 520/40 band pass (BP) emission filter was used, while for the detection of the ladder, the 670/30 BP filter was used.

2.4.5 Immunoprecipitation

For the immunoprecipitation (IP) approximately 300 μg of proteins extracted and quantified as described in 2.4.1 and 2.4.2 respectively, were incubated for 1 h at 4°C together with 20 μl of Protein G Magnetic Beads (New England Biolab; Cat. Nu.: S1430S), in order to clear the extract and reduce non specific binding to the beads. Then, with the use of a magnetic rack, the beads were separated from the supernatant, which was placed into fresh tubes. Then 2 μg of mAb1218 (Abcam Anti-GFP antibody, mouse monoclonal; 2 $\mu\text{g}/\mu\text{l}$) was added and the samples were incubated overnight using a rotator, at 4°C.

20 μl of the magnetic beads were added at the mixture, vortexed gently and incubated for 1 h at 4°C. Then the beads were recovered using a magnetic rack and washed 3 times with 400 μl of protease free wash solution (0.1% Triton X-100, 50 mM Tris-HCl, 300 mM NaCl, 5 mM EDTA and one PI tablet for each 10 ml solution). After an additional wash with 400 μl protease free TBS (TRIS buffered saline: 50 mM TRIS, 150 mM NaCl, pH 7.6), the beads were resuspended in 16.25 μl TBS, 2.5 μl Reducing Agent (Invitrogen; 500 mM DTT) and 6.25 μl of 4x LDS sample buffer (Invitrogen; 40% glycerol, 6.8% Tris-Base, 6.6% Tris-HCl, 8% LDS, 0.06% EDTA, 0.75% Serva Blue G250, 0.25% Phenol Red) for a final volume of 25 μl . For every sample, a no-IP (input) tube, containing 16.25 μl of the extracted protein, together with 6.25 μl of 4x LDS sample buffer and 2.5 μl Reducing Agent was also prepared.

All the samples (IP and No-IP) were incubated for 10 min at 70°C and then placed in a magnetic rack to separate beads from supernatant. The IP and No-IP samples and a pre-stained protein ladder (New England Biolabs; Cat. Nu.: P7710S) were finally loaded on a 3-8% Tris-Acetate SDS gel for separation and western blotting.

2.4.6 Western blot detection

For the protein separation of the immunoprecipitated samples the NuPAGE Tris-Acetate SDS Buffer Kit (Invitrogen) was used. The Running Buffer was prepared by diluting 50 ml of 20x Tris-Acetate Running buffer (1 M Tricine, 1 M Tris Base, 70 mM SDS in H₂O, pH 8.25) in one liter of distilled water. From this dilution, 200 ml were complemented with 500 μl Antioxidant (N,N-Dimethylformamide and sodium bisulfate). A ready-to-use pre-cast NuPAGE Novex 3–8 % Tris-Acetate gel (Invitrogen) was loaded into a XCell SureLock electrophoresis chamber (Invitrogen) and the 200 ml of the Run-

ning Buffer with the antioxidant were used to fill the inner part of the chamber, while the rest of the Running Buffer filled the outer part. The samples and the ladder were loaded in the gel and the electrophoresis run for 50 min at 150 mVolts.

Before the end of the electrophoresis, 1200 ml of Transfer Buffer (10 mM NaHCO₃, 3 mM Na₂CO₃, 20% methanol and 0.01% SDS solution at pH 9.22) were prepared. After the separation, the proteins were transferred to a nitrocellulose membrane (Amersham Hybond ECL - GE Healthcare) with the following procedure: The membrane and the gel were incubated in Transfer Buffer and under shaking at RT for 10 min. Then a 'sandwich' consisting of the gel with the proteins and the membrane placed within tight contact surrounded by two pieces of Whatman paper and a sponge at each side, was placed into a transfer tank Mini Trans-Blot Cell (BioRad) within a gel holder cassette (Bio-Rad). For the transfer, a gradient voltage from 10 to 40 mV increased by steps of 10 mV every 10 min and a final step at 50 mV for 40 min was applied. Then, the nitrocellulose membrane with the proteins was removed and dried overnight at RT.

The dried membrane was incubated in distilled water for 10 min and then the Pierce Western Blot Signal Enhancer (Thermo Scientific) was used according to the manufacturer's instructions (Solution A for 5 min, 5x wash with distilled water, solution B for 10 min and 5x wash with distilled water). Then, the blotted membrane was blocked for 1 h with 0.1% Casein (Roche) in TBST (Tris buffered saline containing Tween-20) at RT, in order to block unspecific binding sites for the antibodies. Afterwards, the membrane was incubated with polyclonal rabbit anti-Eag1 antibody (Napp et al. (2005); 1:1500 in 0.1% Casein-TBST) for 90 min and washed thoroughly for 7 times with deionized water followed by 5 min incubation with TBST at RT. Then, the membrane was incubated for 60 min at RT with secondary ECL anti-rabbit IgG antibody HRP-linked (GE Healthcare; 1:7000 in 0.1% Casein-TBST). Subsequently, the membrane was washed again for 7 times with deionized water and incubated for 5 min with TBST at RT. Then, we dried the membrane with paper towels and incubated it for 5 min with Immobilon Western Chemiluminescent HRP Substrate (Millipore). Finally, the luminescence was imaged using Chemi-Doc XRS system (BioRad).

In order to blot again the membrane with a second antibody after the imaging, the nitrocellulose was washed for 5 min at RT with TBS, the strip buffer was applied for 7 min and a last wash for 5 min with TBS was performed. Then, the procedure could start again from the blocking step (1 h with 0.1% Casein in TBST at RT). In this study, the second blotting of the membrane took place with mAb6556 (anti-GFP polyclonal mouse; 1:1000; Abcam) and in this case the secondary antibody used was ECL anti-mouse IgG antibody HRP-linked (GE Healthcare; 1:7000 in 0.1% Casein-TBST). All the interval steps for the second blotting were the same, as for the first blotting.

2.5 Immunocytochemistry

2.5.1 Primary cilia

Primary cilia consist of microtubules [Satir et al. (2010)] with acetylated- α -tubulin present at various microtubule formations stabilizing this specific structure [Maruta et al. (1986)] and its labeling can be used to visualize primary cilia [Schneider et al. (2009)].

Cells (with a density of 130 thousand per ml) were grown on glass coverslips (#1.5 - Menzel-Gläser) for 24h, scratched with a 10 μ l pipet tip and then 1h after the scratch, they were fixed in 10% Neutral Buffered Formalin (100 ml/L formaldehyde 37-40%, 900 ml/L distilled water, 4 gr/L monobasic sodium phosphate, 6.5 gr/L dibasic sodium phosphate; SIGMA[®]) for 8 min at 4°C and permeabilized at RT in 0.5% Triton-X-100 in TBS. After the blocking in TBS with 10% BSA for 30 min, cells were incubated for 1h at RT with anti-acetylated- α -tubulin [1:2000 mouse; Abcam[®]] and then after washing with TBST, they were incubated for 30 min at RT with AlexaFluor[®]546 secondary antibody [1:1000 goat anti-mouse; Life Technologies[®]]. The prepared coverslips were then mounted with Prolong Gold anti fade kit with DAPI (Molecular Probes[®]) and kept for at least 12h at 4°C.

Samples were then visualized in a Leica SP5 CLSM, using the 514 nm argon laser excitation for the mVenus fluorochrome (expressed in HT-1080 cells), the 405 UV laser for the DAPI signal and the 561 laser excitation for the AlexaFluor[®]546 signal.

2.5.2 Focal adhesion kinase

Focal Adhesion Kinase is a crucial signaling protein that acts as an important receptor and regulator of cell shape, adhesion and motility and is localized to cell adhesion sites known as focal contacts [Mitra et al. (2005)]. These contacts are thought to be approximately 40 nm higher than the substrate, almost twice the length of the extracellular fragment of integrins [Pierres et al. (2002)].

For the staining of FAK, cells were grown for 24h in 4-well dishes (Lab-Tek Chambered Coverglass #1 - Thermo Scientific Nunc[™] Lab-Tek[®] Chamber Slides) with a density of 50 thousand per ml. The cells were then fixed with 10% Neutral Buffered Formalin (SIGMA[®]) for 10 min at RT and permeabilized also at RT in 0.5% Triton-X-100 in TBS. After blocking with 10% BSA in TBS for 30 min, cells were incubated for 1h at RT with anti-FAK mAb [1:250 purified mouse; BD Bioscience] and then after washing with TBST, they were incubated for 30 min at RT with AlexaFluor[®]647 secondary antibody [1:500 goat anti-mouse IgG; Molecular Probes[®]]. The prepared samples were kept in TBS at 4°C until the time of imaging.

Samples were visualized in a Leica SP5 CLSM, using the 514 nm laser excitation for

the mVenus fluorochrome, and the 633 nm laser excitation for the AlexaFluor[®]647 signal. For the IRM acquisition we followed the settings that are described at 2.6.

2.5.3 Phalloidin staining

Phalloidin bicyclic peptide can selectively label filamentous-actin (F-actin) and can be used to visualize stress fibers and filopodia. Filopodia are F-actin rich, long and thin plasma membrane protrusions that can be found in association with lamellipodia at the leading edge of migrating cells and are involved in migration and in extracellular environment sensing [Doherty and McMahon (2008)].

In this study, the phalloidin staining was used in HeLa cells, together with EGFP-K_v10.1 in order to reveal the localization of K_v10.1 ion channel to filopodia. HeLa cells were fixed with 10% Neutral Buffered Formalin (SIGMA[®]) for 10 min at RT and permeabilized also at RT in 0.5% Triton-X-100 in TBS. The samples were then blocked with 10% BSA in TBS for 30 min, and incubated for 1 h at RT with AlexaFluor[®]633-Phalloidin [1:100; Invitrogen, Cat. No. A22284] followed by washing with TBS.

Dr. M. Mitkovski prepared the samples and acquired the respective images, before the start of this study.

2.6 Interference reflection microscopy

2.6.1 Acquisition

In this study, for the acquisition of IRM images we used two excitation wavelengths at 570 and 670 nm (at 10% of nominal laser output) using the Leica SP5 white light laser. The usage of dual wavelength excitation gave us the opportunity to identify higher order interferences in multiple Newton rings patterns. We also used a Leica HCX PL APO 63x / 1.3 Glyc CORR CS (21°C) objective (A in Figure 6), while the mounting medium was Immersol[™] G Glycerin (Zeiss) with a refractive index $n=1.456$ (at 23°C). With this objective, which has a relatively high NA (1.3), and choosing a pinhole size of 1 A.U. we had achieved a relatively small DoF ensuring that only the reflections from the lower part of the acquired cells were collected. This objective had also a correction collar. With the proper correction collar adjustments, we were able to make corrections for the mounting medium refractive index, the cover glass thickness as well as the temperature. We also used the resonant scanner of the system, which can scan and acquire data with high frequency (8 kHz) and collected the reflected light using Leica's hybrid-detectors using 10 times frame averaging and 2 times line accumulation of photons.

Moreover, in order to ensure that the objective was set correctly, before the start of the acquisition we performed the following adjustments: we used the excitation from both

wavelengths (570 and 670 nm) and under reflection mode we focused on the upper level of the glass substrate by selecting the focal plane with the brightest background (wave 7 and pixel e in Figure 5). Then we switched to an xz scan mode and without changing the focal plane we rotated the objective correction collar in such a way that the xz scan line (orange line in B in Figure 6) was as sharp and intense as possible, indicating that most reflection takes place at this interface. The above procedure was repeated also when we acquired images from distant areas of the same well or from different wells of the 4-well chamber that we used, in order to ensure that the possibly different glass thickness would not affect the acquired reflected signal.

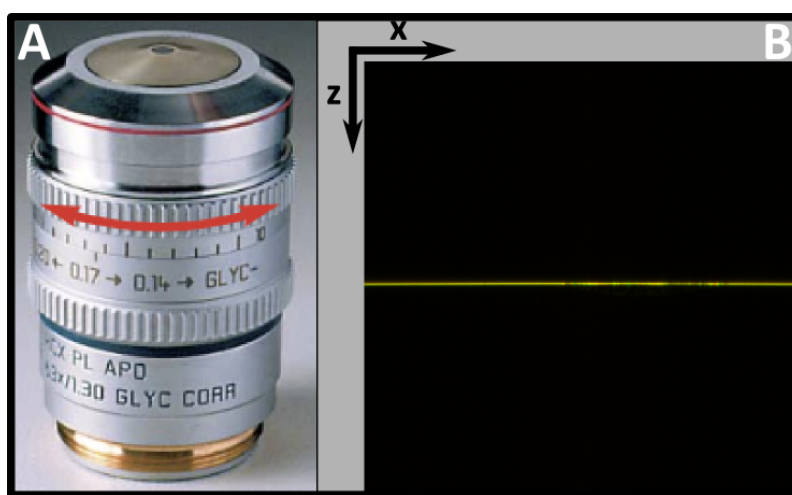


Figure 6 – Fine adjustment of objective's correction collar (red arrow in **A**) in order to obtain the sharpest line under xz IRM scan mode (**B**). The horizontal yellow line is coming from the reflection of 570 and 670 nm wavelength of the interface between the glass and the culture medium. Image in **A** from Leica Microsystems - Confocal Application Letter - [April 2004, No. 17](#)

The above settings were used in the case of single time point IRM acquisition of live cells in order to determine the adhesion ability of cells, but also in the case of time lapse live IRM imaging for the dynamics of cell-surface adhesion. Especially for the time lapse live IRM imaging, we employed an auto focus routine based on the IRM signal from a position 2-3 fields of view away from the acquired cells. Areas containing small, granular particles were avoided, as they are prone to generating high intensity signal that can skew the final IRM-based adhesion quantification. Also, cells that under IRM appeared with multiple Newton rings were avoided. These rings in some cases were apparent despite the settings we used, probably because of cell thickness (lower than 100 nm) that caused interference of reflections from dorsal cell areas or unevenness of the chamber surface.

2.6.2 Quantification

The background of the acquired images is always not homogeneous, even when all hardware settings have been set up properly. In our case, in order to overcome this prob-

lem, we removed the uneven illumination of the background by normalizing the raw pixel intensities by a highly blurred version of the raw image, using the gaussian distribution of intensities in a range of 20 pixels radius. The normalization occurred with the division of the raw pixel intensities by the intensities of the blurred image, removing the low frequency signal from the acquired images. This technique is quite similar to other techniques that make use of background subtraction from IRM images [Limozin and Sengupta (2007)].

For the height reconstruction based on the normalized reflected intensities, we used the Min/Max method [Limozin and Sengupta (2009); Schilling et al. (2004)], since the distances of cell membranes from the substrate are less than a couple of hundred nm, and the NA values are such that we can avoid interferences from the dorsal area of the cell. In this case, the experimental maximum and minimum intensities are the same as the theoretical ones and equation 5 or 6 can be used for height determination. In this study, the minimum and maximum normalized intensities were determined from the acquired images (single time point or time lapse images), using a simple algorithm. Having these intensities we managed to reconstruct the IRM images with pixel values that correspond to the distance of the membrane from the glass surface.

2.7 Scratch assay

For every scratch assay performed in this study, all the following conditions were kept, unless stated otherwise.

2.7.1 Sample preparation

HT-1080-mVenus and / or HT-1080-K_v10.1-mVenus cells were seeded in 4 or 8-well chambers (Lab-Tek Chambered Coverglass #1 - Thermo Scientific Nunc™ Lab-Tek® Chamber Slides), 24 h before the experiment at a density of 130 thousand cells per ml. Approximately 45 min before acquisition, a scratch with a 10 µl pipette tip was made in each well, and the cells were washed once with imaging solution (IS). The IS is a modified Tyrodes buffer consisting of 135 mM NaCl, 5.37 mM KCl, 1.66 mM MgCl₂, 1.8 mM CaCl₂ and 10 mM HEPES at pH 7.4. Finally, IS supplemented with 5% FCS (ISF) was added to each well prior to acquisition.

For imaging with the IncuCyte™ ZOOM device (Essen Bioscience Inc.), cells were seeded in wells of an ImageLock™ 96-well micro-plate with a density of 15 thousand cells per well. Cells, seeded in micro-plate vessels were incubated for 24 h in the IncuCyte™ ZOOM at 37°C and 5% CO₂. Then the scratch was made with the Wound-Maker™, a 96-pin mechanical device designed to create homogeneous, 700-800 micron wide scratch wounds in cell monolayers. The culture medium was then exchanged with

fresh one, in order to remove the detached cells and the plate was put back in the In-cuCyte™ ZOOM.

For the case where mAb56 or AST blockers were used, cells were incubated with 0.01 µg/ml mAb56 or 1 µM AST, respectively for 24 h prior to live imaging. The IS contained the identical blocker concentrations.

2.7.2 Live imaging conditions

For the time-lapse acquisition, cells were kept at 37°C (controlled by “The Cube” system (Life Imaging Services; Switzerland)) and 8% CO₂ (controlled by “The Brick” (Life Imaging Services; Switzerland) gas mixer with a rate 25 L/h) in a humidified environment. The scratch closure was monitored for at least 3 hours after the generation of the scratch.

2.7.3 Microscope settings

Time lapse imaging was performed with a Leica SP5 (Leica Microsystems, Mannheim) confocal laser scanning microscope (CLSM), at multiple positions at an approximate 150 sec time interval using a 20x immersion objective, while employing an autofocus routine to counteract z-drifts in time (Figure 7).

The mVenus fluorochrome was excited using 3% of the nominal Argon laser power output, at 514 nm, with an energy density of 1.581 µJ/cm² per time frame scan (see 2.10.1 for laser energy measurements). For the detection of emitted photons, a hybrid detector (under photon counting mode) was used, where each line was accumulated 10 (Acc) and each frame averaged 6 times (Av) (Figure 17). In this case, we used the resonant scanner of the system at 8 KHz. The pinhole of the system was set at 2 AU (Airy units). These stimulation / acquisition settings were found to generate low phototoxicity, but sufficient fluorescence signal for later analyses and are in accordance with previous studies [Borlinghaus (2006); Donnert et al. (2007)]. The resulted data consisted of single channel time stack images per monitored field of view, used for analysis.

During IRM live cell imaging the environmental conditions were kept identical to those during fluorescence collection. Using the same time interval, objective and the same type of scanner, we employed an autofocus routine based on the IRM signal of the scratch. The recorded IRM signal was based on the 633nm excitation/reflection (10% nominal laser output). The mVenus signal generated by the stably transfected HT-1080 cells upon 514 nm excitation was collected in a sequential manner. The resulted data consisted of multi channel time stack images per monitored field of view, where the pixel intensities of the IRM acquired signal reflected the distance of cell membranes from the substrate (Figure 5).

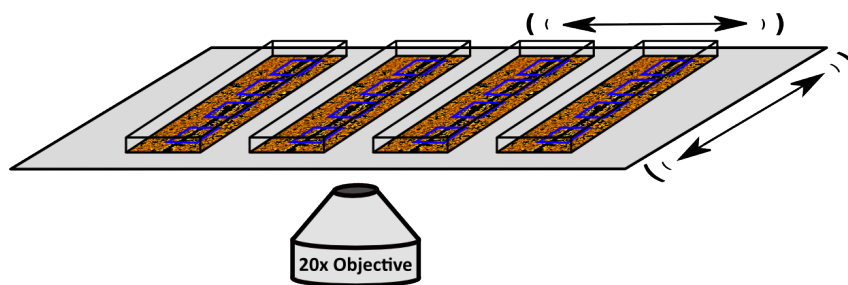


Figure 7 – Schematic representation of the scratch assay acquisition using a 4-well chamber. Multiple positions / fields of view (blue squares) were monitored over time. Up to 4 positions per well were acquired for at least 3 h after the generation of the scratch.

2.8 Cell surface adhesion

2.8.1 Sample preparation

For the study of cell-surface adhesion of individual cells with IRM, both HT-1080-mVenus and HT-1080-K_v10.1-mVenus cells were seeded in 4-well chambers (Lab-Tek Chambered Coverglass #1 - Thermo Scientific Nunc™ Lab-Tek® Chamber Slides), 24 h before the experiment. In this case the cell density was 50 thousand cells per ml. Before the acquisition, the culture medium was replaced with pre-warmed at 37°C ISF, after a wash with also pre-warmed IS. This medium exchange was essential to take place slowly and gently in order not to disturb the adherent cells. For experiments where mAb56 blocker was used, the culture medium as well as the ISF were supplemented with 0.01 µg/ml mAb56.

2.8.2 Cell-surface adhesion ability

In order to measure the adhesion ability of individual HT-1080-mVenus and HT-1080-K_v10.1-mVenus cells, we acquired single time point Dual-Wavelength IRM images as described in 2.6. More specifically, 35 HT-1080-mVenus and 35 HT-1080-K_v10.1-mVenus live cells were acquired under IRM mode. The experiment was repeated after blocking K_v10.1 with 0.01 µg/ml mAb56 24 h before and during the experiment. In this case, 40 individual HT-1080-mVenus and 30 HT-1080-K_v10.1-mVenus cells were acquired under IRM mode.

2.8.3 Cell-surface adhesion dynamics

In order to reveal the dynamic nature of cell-surface adhesion process, we proceeded with time-lapse live imaging acquisition using dual-wavelength IRM settings as described in 2.6, monitoring every cell for almost 20 min with a time interval of approximately 24

sec. For this experiment, 7 individual HT-1080-mVenus and 5 HT-1080-K_v10.1-mVenus cells were acquired and quantified.

2.8.4 TIRF

In this study for the qualitative detection of K_v10.1-mVenus signal from the lower part of the adhesive cell surface, a demo system from TILL Photonics (now part of FEI Life Sciences) was used. For TIRF experiments the samples were prepared as described in the cases of scratch assays (see 2.7.1).

2.9 Image analysis

The FIJI (Fiji Is Just ImageJ) image-processing package [Schindelin et al. (2012)] was used to open, inspect, manipulate and quantify all our CLSM data sets. Additionally, new, automated analysis algorithms were implemented in the form of FIJI macros or Perl² programming language scripts in order to analyze images and post-process measured results.

2.9.1 Scratch assay

The scratch closure speed was calculated from the slope of the linear part of the plotted scratch area over time (red line in Figure 8).

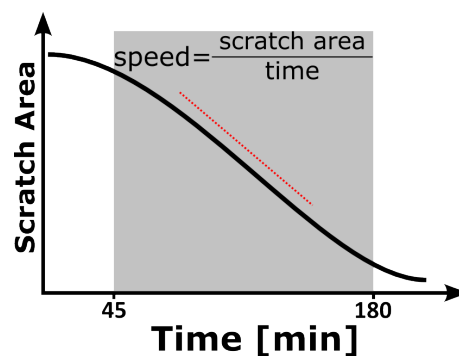


Figure 8 – Reduction of scratch area over time. During scratch closure, the phases of acceleration, stable speed and deceleration (initial, central and final part of plotted curve, respectively) can be distinguished. Speed [$\frac{\mu\text{m}^2}{\text{min}}$] was calculated only for the time period with a linear scratch closure speed (red line).

With a specific program, implemented as a set of FIJI macros we were able to process the time-lapse sequence of each field of view in a frame-by-frame manner, while detecting

²www.perl.org

and measuring the scratch area and the unoccupied intercellular area (Figure 9). Data obtained in this manner, with the help of a number of Perl scripts, was used to calculate the scratch closure speed (SCS) in $\frac{\mu\text{m}^2}{\text{min}}$ (by equation 7) and the cell-cell adhesion loss (as a maximum intercellular area - MIA - during the monitored scratch closure period, normalized by the initial area occupied by cells - IAO), during the dynamic phenomenon of cell migration, initially induced by a scratch (equation 8).

$$\text{Scratch Closure Speed (SCS)} = \frac{\Delta\text{ScratchArea}}{\Delta t} \quad (7)$$

$$\% \text{Maximum Intercellular Area (\%MIA)} = \frac{\text{Maximum Intercellular Area}}{\text{Initial Area Occupied}} \quad (8)$$

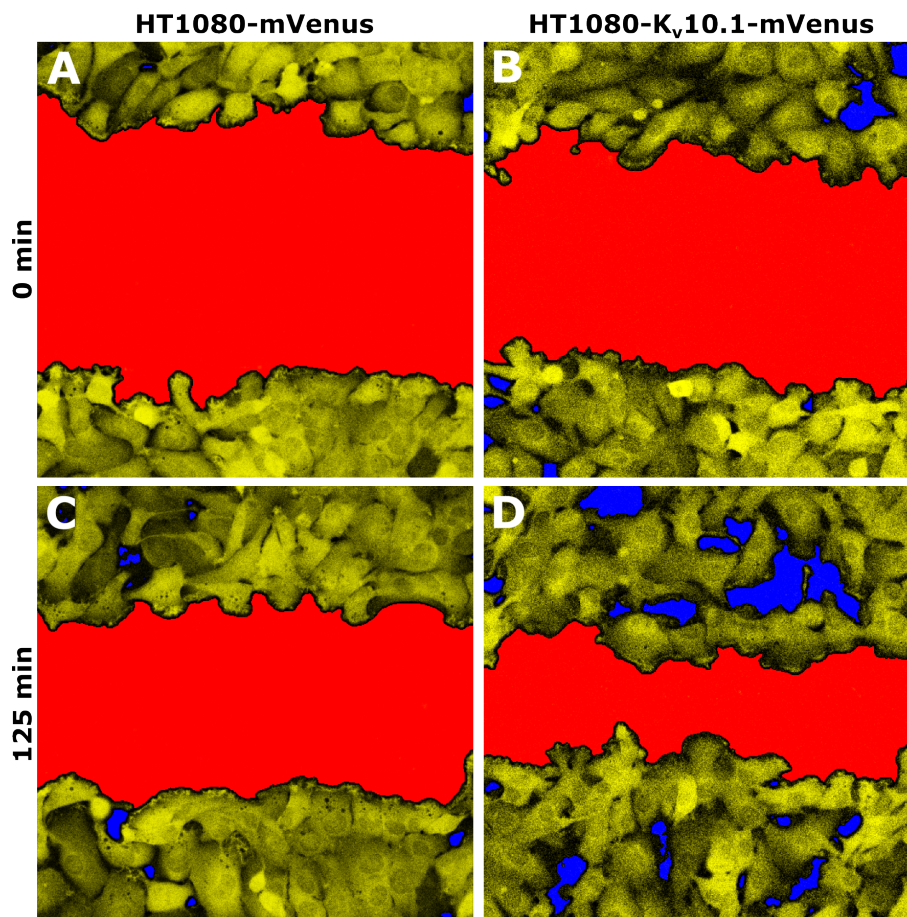


Figure 9 – **A** and **C** illustrate the 0 and 125 min (after the acquisition started) time point of HT-1080-mVenus cells, while **B** and **D** show the same respective time points with HT-1080-K_v10.1 cells. Marked in red is the scratch area, while the blue color is indicative of the intercellular space. Both colors are masks generated and overlaid by the FIJI macro at each time point.

2.9.2 Scratch assay with IRM

The dynamic measurement of the lamellipodial cell-surface adhesion during the scratch closure, was accomplished by acquiring and processing the fluorescence and IRM signal. We applied the same algorithm used for the quantification of the scratch closure rate to generate binary masks of migrating cells from their fluorescence signal. These masks were then modified by subtracting sequential frames and dilating the resulting mask, to cover parts below the lamellipodium, where anterograde movement had occurred (red areas in B of Figure 10). In these regions we measured the adhesive area (green in C of Figure 10) from the IRM signal (A in Figure 10) and these measurements were then normalized by the size of the migration zone area and accumulated for the first 40 mins of the acquisition. With this, we were able to generate graphs showing the dynamic cell-surface behavior of migrating cells under the lamellipodial area.

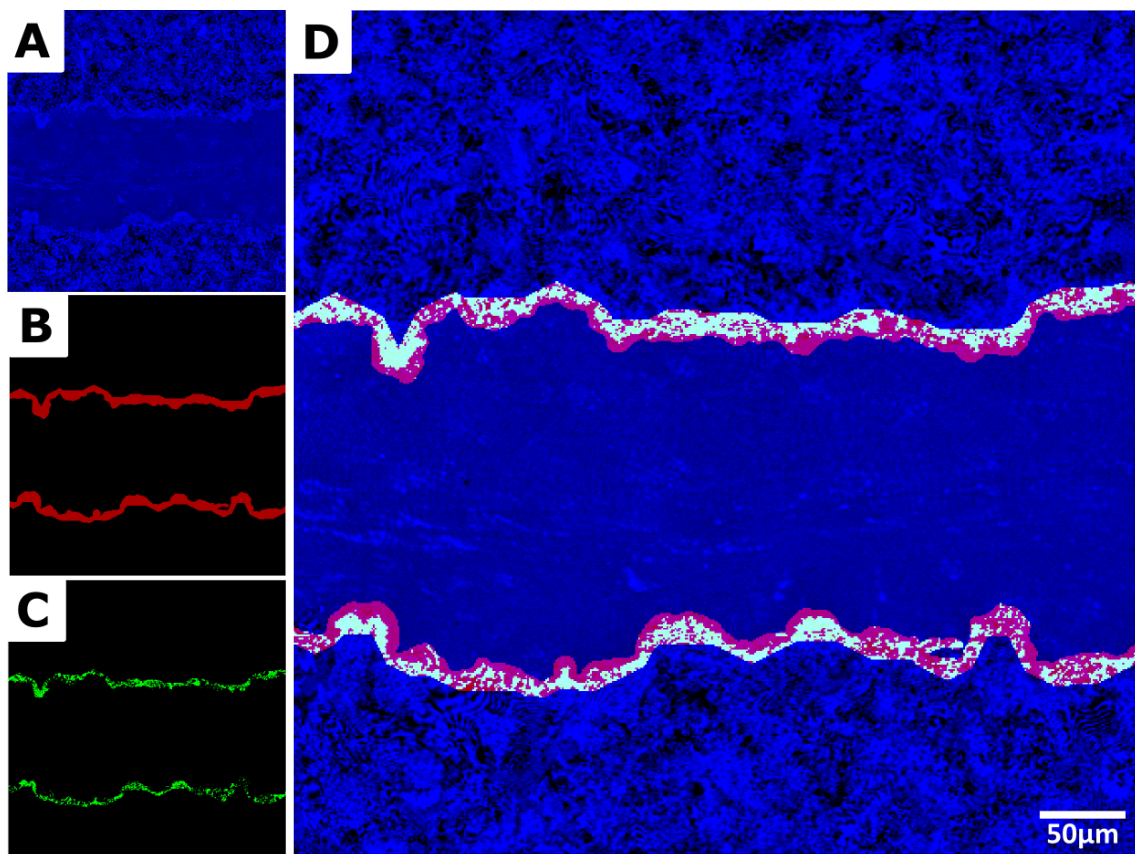


Figure 10 – IRM images of cells during scratch closure. The IRM signal was inverted (**A**), and after the generation of migration zone masks (**B**), the thresholded adhesive area (shown in **C**) was calculated. **D** is the merged image of **A**, **B** and **C**. The adhesive area (green in **C** and **D**) was normalized by the migration zone area (red in **B** and **D**).

2.9.3 Individual cell tracking measurements

A representative group of cells was marked for the first 140 min of scratch closure with an interval of 2.16 min and cell-route coordinates were extracted with FIJI. In total, 500 HT-1080-mVenus and 490 HT-1080-K_v10.1 cells, from different experiments were tracked using fields of view, where the major scratch axis was always horizontal. From each field of view 10 individual cells from the edges of the scratch were manually marked as shown in Figure 11.

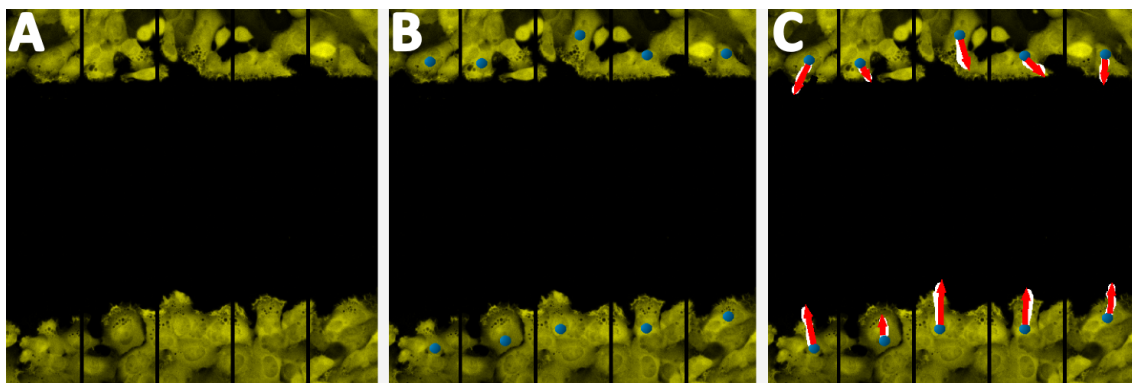


Figure 11 – Each scratch field of view was divided in 5 sections (**A**) in each of which 2 cells migrating into different directions were manually marked (**B**). The reference point for each cell (blue dots) was placed at the nucleus. From the coordinates of each reference point at every time frame, we were able to project all cell trajectories (white tracks) in **C** and also calculate the final displacement vector for each cell (red arrows). Additional measurements performed with all cell routes coordinates using the equations described in Table 3. Cells shown are HT-1080-mVenus.

Cell trajectories were plotted using a common origin point in order to visualize any possible differences at their migratory pattern, after the extraction of the coordinates from control and K_v10.1 overexpressing cells and for all time points. In addition to all routes and for an interval of 2.16 min, we calculated the displacements (d_i) (equation 13, Table 3), the final displacement from the point of origin (d_c) (equation 15, Table 3; red arrows in Figure 11) and also the accumulated distance (AD) covered during N displacements of each cell (equation 17, Table 3).

Additionally, for every displacement we calculated the interval migration speed (u_i) (equation 10, Table 3), and we were able to find the mean (\bar{u}_i) and maximum (u_{max}) migration speed of all N displacements (equations 12 and 14 in Table 3, respectively). Concerning the directionality of migration, we calculated the average migration angle (\overline{MA}) of every cell (equation 16, Table 3) and we were also able to calculate the straightness (Str_c) of each route, as the ratio between the final displacement (d_c) and the accumulated distance AD (equation 18, Table 3).

Finally, in order to describe the overall motion of these migrating cells we calculated the Mean Squared Displacement (MSD) value, which can be considered as the amount of

explored space [Dieterich et al. (2008)] and is used to describe the type of movement that particles or even cells have. In this study the Δt used for the MSD calculation, ranged from 2.16 to 13 min, out of 140 min time period measured, for both cell types.

| | |
|--|---|
| $\Delta_x = (x_{i+1} - x_i) \quad (9)$ | $u_i = \frac{d_i}{\Delta t} \quad (10)$ |
| $\Delta_y = (y_{i+1} - y_i) \quad (11)$ | $\bar{u}_i = \frac{1}{N} \sum u_i \text{ for } i = 1 \dots N \quad (12)$ |
| $d_i = \sqrt{\Delta_x^2 + \Delta_y^2} \quad (13)$ | $u_{max} = \max(u_i) \quad (14)$ |
| $d_c = \sqrt{\Delta_{x(final)}^2 + \Delta_{y(final)}^2} \quad (15)$ | $\overline{MA} = 1/\tan\left(\frac{\Delta_{y(final)}}{\Delta_{x(final)}}\right) \quad (16)$ |
| $AD = \sum d_i \text{ for } i = 1 \dots N \quad (17)$ | $Str_c = \frac{d_c}{AD} \quad (18)$ |
| $MSD_i = \frac{1}{N} \sum d_i^2 \text{ for } i = 1 \dots N \quad (19)$ | |

Table 3 – Equations used for individual cell tracking measurements

2.9.4 Cell-surface adhesion ability

From the acquired IRM images we calculated the proximity of membrane area to the glass surface using the equation 6 described in 2.6.2. Additionally, binary masks of cells footprints were generated by segmenting the IRM images with the FIJI Trainable Weka Segmentation plugin³ (blue area in Figure 12) and their areas were measured. Membrane areas lower than 40 nm from the substrate (focal adhesion areas) were considered to be the areas that participate to focal adhesion sites [Pierres et al. (2002); Klein et al. (2013)]. These areas were masked (red areas in Figure 12) and measured for every acquired cell.

³http://fiji.sc/Trainable_Weka_Segmentation

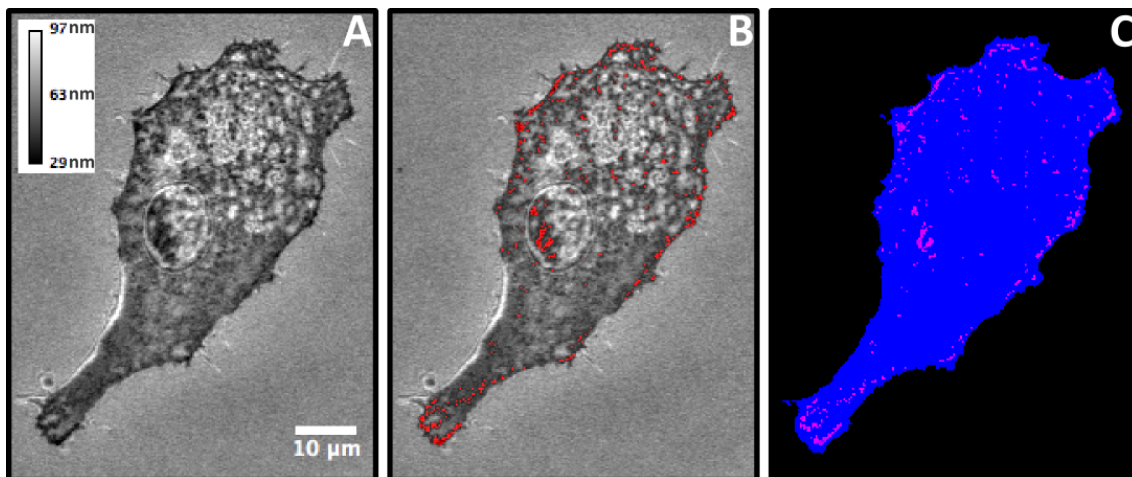


Figure 12 – Representative image of cell-surface adhesion ability quantification. From the IRM raw data, we generated images with pixel intensities that correspond to membrane-substrate distances in nm (**A**). Additional mask images were generated, that correspond to cell footprints (blue area in **C**) and the areas that are closer than 40 nm to the surface were marked (red areas in **B** and **C**). Calibration bar units in **A** are in nm. Cell shown here is HT-1080-mVenus.

With these measurements at hand, we calculated the ratio of membrane area that is closer than 40 nm to the surface by the cell footprint for every cell. This ratio is the proportion of cell footprint that is used for focal adhesion on the substrate. The higher this ratio is, the greater is the ability of a cell to adhere on the substrate.

2.9.5 Cell-surface adhesion dynamics

Using the algorithm that is extensively described in 6.2, we were able first to define for every time point and for every monitored cell, the non-motile area (blue in Figure 13), as well as the protruding (green in Figure 13) and retracting (red in Figure 13) areas.

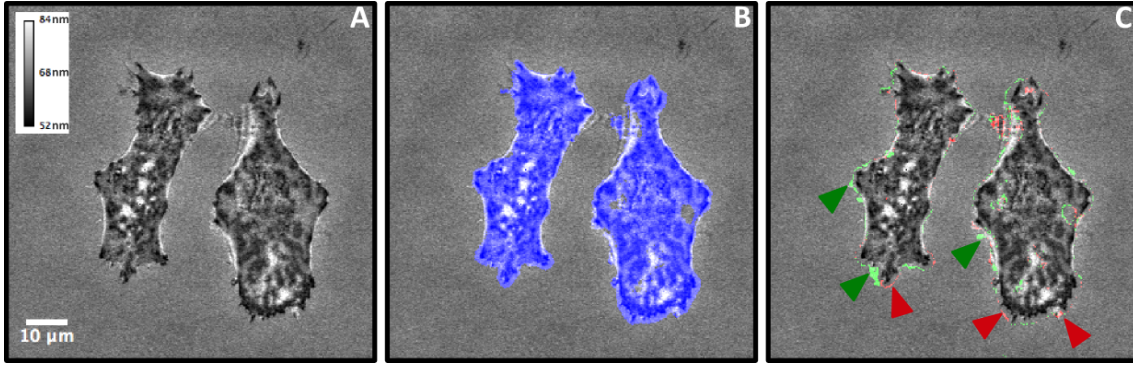


Figure 13 – Representative result image of cell-surface adhesion dynamics quantification. From the IRM raw data, we generated images with pixel intensities that correspond to membrane-substrate distances in nm (**A**). Additionally, mask images were generated that correspond to cell footprints for every time point and from these masks the non-motile area of each cell was defined (blue area in **B**). From each cell footprint area, the protrusions (green areas in **C** indicated with green arrowheads) and the retractions areas (red areas in **C** indicated with red arrowheads) were defined using a subtraction step of one frame (see text for details). Calibration bar units in **A** are in nm. Cells shown here are HT-1080-mVenus.

Moreover, we managed to measure for both HT-1080-mVenus and HT-1080-K_v10.1-mVenus cells, the mean cell footprint, the protrusion and retraction rate ($\mu\text{m}^2/\text{min}$), the mean distance (in *nm*) of cell membrane in protrusion, retraction and non-motile cell regions, as well as the rate of vertical membrane movements (in *nm/min*) in protruding, retracting and non-motile membrane areas.

2.10 Stimulation / acquisition settings effect

2.10.1 Laser measurements

The laser intensity was measured using a photodiode mounted on a soda lime glass slide and placed in the object plane of the microscope. The photodiode (Hamamatsu S2386-18K) was connected to a commercial trans impedance amplifier of ≥ 50 kHz bandwidth at a conversion factor of up to $\kappa=10^7 \frac{\text{V}}{\text{A}}$ (FEMTO DLPCA 200), the output voltage U_{out} of which is recorded with a digital storage oscilloscope (Figure 14). From the photodiode's calibration sheet, the responsivity $\gamma(\lambda)$ of the photodiode (given as current per incident power) can be derived for the exact wavelengths in question with sufficient accuracy by linear interpolation. The incident light power is then given by equation 20:

$$P = \frac{U_{out}}{\kappa \cdot \gamma(\lambda)} \quad (20)$$

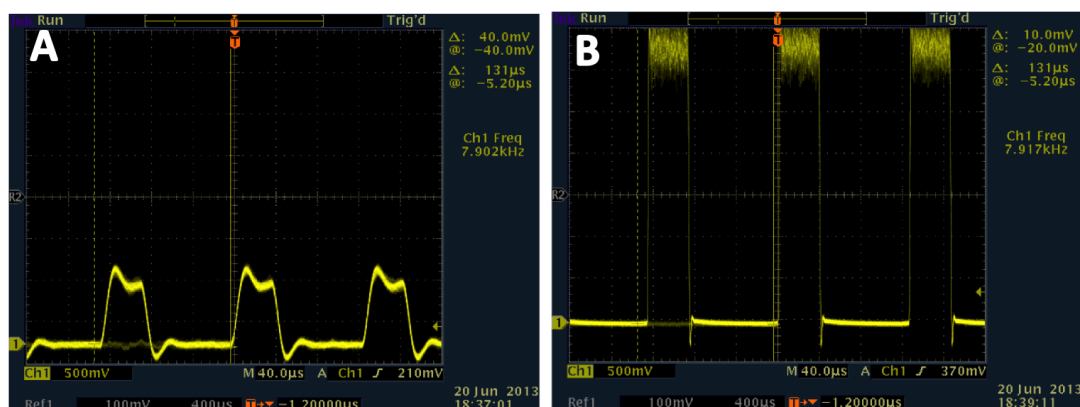


Figure 14 – Photodiode's light signals recorded as voltages by a digital storage oscilloscope. Software setting at 1 and 80% of nominal laser power (**A** and **B**, respectively)

Special caution must be taken at all times to ensure that the photodiode does not saturate, or that the combination of photodiode, BNC-cable and amplifier does not smooth out the signal. The saturation was checked by additionally illuminating the Photodiode with a high power LED torch. The signal rises far above the values obtained for the lasers, thus proving that the photodiode is not saturated. The above-described measurements took place with the kind help of Mr. Kai Bröking.

The light signal consists of square pulses of a constant duration (Figure 14). Integration over one pulse yields the total incident light energy imposed on the sample during the acquisition of each single pixel. The duration of one such pulse was established to be $\tau = 40 \mu\text{s}$. The measurement was repeated using either continuous 514 nm wavelength (CW) generated by the Argon ion laser, or pulsed laser at 514 nm from an NKT White Light Laser (WL), and a resonant scanner at 8 kHz or a conventional scanner at 0.4 kHz. The power delivered to the sample was independent of the scan speed (Figure 15).

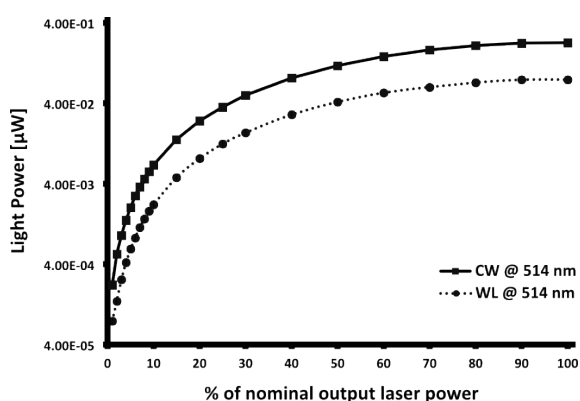


Figure 15 – Laser power delivered to sample for each % setting of nominal output laser power. The power delivered is independent of the scan speed.

Moreover, we were able to calculate the energy density ED as $\mu\text{J}/\text{cm}^2$ for each % of nominal laser power used, from the characteristics of the 20x objective, used for the mea-

surements and the following experiments (Figure 16).

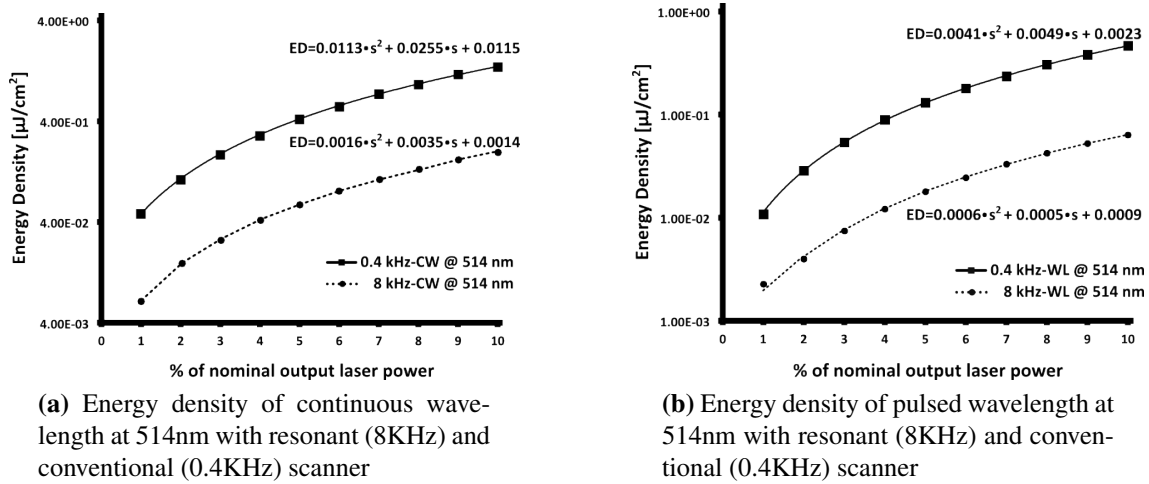


Figure 16 – Energy density of continuous and pulsed wavelength with two different scanners

The fitted polynomial equations shown in graphs of Figure 16 were used to calculate the energy density for every combination of laser and scanner used during the acquisition of data (Table 4).

| | |
|------------------------|---|
| CW and 0.4 kHz scanner | $ED = 0.0113 \cdot s^2 + 0.0255 \cdot s + 0.0115$ |
| CW and 8 kHz scanner | $ED = 0.0016 \cdot s^2 + 0.0035 \cdot s + 0.0014$ |
| WL and 0.4 kHz scanner | $ED = 0.0041 \cdot s^2 + 0.0049 \cdot s + 0.0023$ |
| WL and 8 kHz scanner | $ED = 0.0006 \cdot s^2 + 0.0005 \cdot s + 0.0009$ |

Table 4 – Equations used for energy density calculations for the different combinations of settings used. ED is the energy density and s the % of nominal laser power

2.10.2 Sample preparation

The effect of different stimulation and acquisition settings on cell migration, was studied with the use of the scratch assay and only for HT-1080-mVenus cell line. For the preparation of the samples we followed the steps described in 2.7.1.

2.10.3 Microscope settings

Throughout the study, it was essential to ensure that every described difference in cell behavior across different acquisition settings does not arise due to differences at the amount of the delivered laser excitation energy. To this direction, with the equations of Table 4, we calculated the % of nominal laser output(s) for the different combinations of acquisition settings, using specific energy density (ED) levels. The energy densities described in Table 5 (first column), correspond to the total energy delivered to the sample

during the acquisition of a single time frame. The time interval between two sequential time frames was, as in all scratch assays in this study, approximately 150 sec. The maintenance of this time interval was not possible using the slow scanner (0.4 kHz) together with multiple acquisition settings over multiple position of the multi-well dishes. For this reason we did not choose this approach in our study.

| Energy Density ($\mu\text{J}/\text{cm}^2$) | CW 8 kHz (multi) | CW 8 kHz (single) | WL 8 kHz (multi) | WL 8 kHz (single) | CW 0.4 kHz (single) | WL 0.4 kHz (single) |
|--|---|--|---|--|--|--|
| 0.948 | 3% (6x Acc, 6x Av) | 23.26% | 6.11% (6x Acc, 6x Av) | 39.32% | 8.05% | 14.60% |
| 1.581 | 3% (10x Acc, 6x Av) | 30.34% | 6.11% (10x Acc, 6x Av) | 50.90% | 10.71% | 19.03% |
| 2.453 | 4% (10x Acc, 6x Av) | 38.06% | 8.49% (10x Acc, 6x Av) | 63.51% | 13.61% | 23.86% |
| 4.905 | 6% (10x Acc, 6x Av) | 54.28% | 12.13% (10x Acc, 6x Av) | 90.00% | 19.71% | 33.99% |

Table 5 – List of % of nominal laser powers and accumulation (Acc) / average (Av) settings for each combination of hardware settings used at each level of energy density delivered to sample per time frame scan. CW corresponds to continuous wavelength from the argon state laser, while WL refers to the white light pulsed laser. For both types of lasers the excitation wavelength was at 514 nm. A multiple and a single scanning approach, concerning the Acc and Av, was selected almost for every combination of laser and scanner type.

The mVenus fluorochrome was excited using either Argon laser at 514 nm (continuous wavelength - CW) or White Light Laser at 514 nm (pulsed wavelength at 80 MHz - WL). Two types of scanning were used in combination with the two laser types. A fast, with the use of resonant scanner at 8 kHz, and a slow, with the use of a conventional scanner at 0.4 kHz (Figure 18). In the case of the fast scanner, we were also able to try different line accumulation and frame average settings (Figure 17), within the 150 sec frame interval as shown in Table 5.

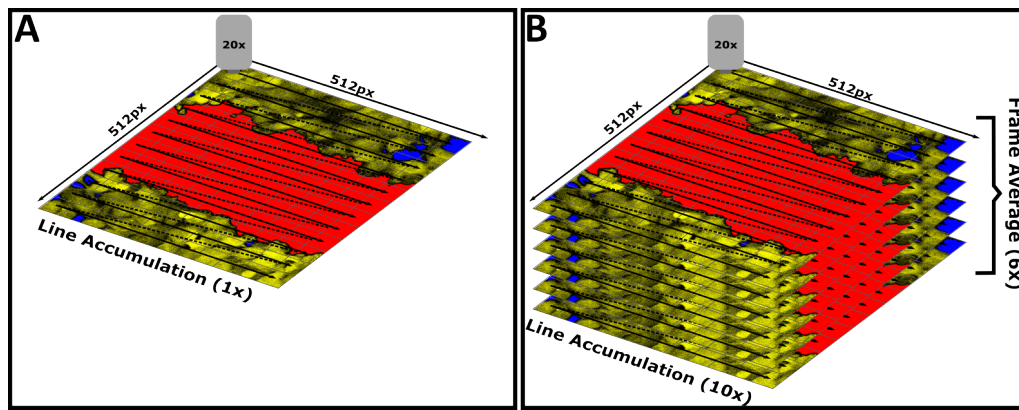


Figure 17 – Two different scanning modes were followed for the acquisition of a single time frame in the live time-lapse imaging. In single acquisition mode (**A**), the field of view is scanned line-by-line only once acquiring the emitted photos. In multiple acquisition mode (**B**), each line of the field of view is scanned multiple times accumulating the emitted photos and the procedure is repeated multiple times for frame averaging. In yellow is presented the HT-1080-mVenus cells with intercellular areas (blue areas) generated during the closure of the scratch (red area).

The different acquisition time scales, as shown in Figure 18, were calculated from the hardware's specifications or were exported from the metadata information, contained within the acquired images. Every combination of acquisition settings was repeated at least three times in different wells of the multi-well chambers, using at least 4 fields of view for each well.

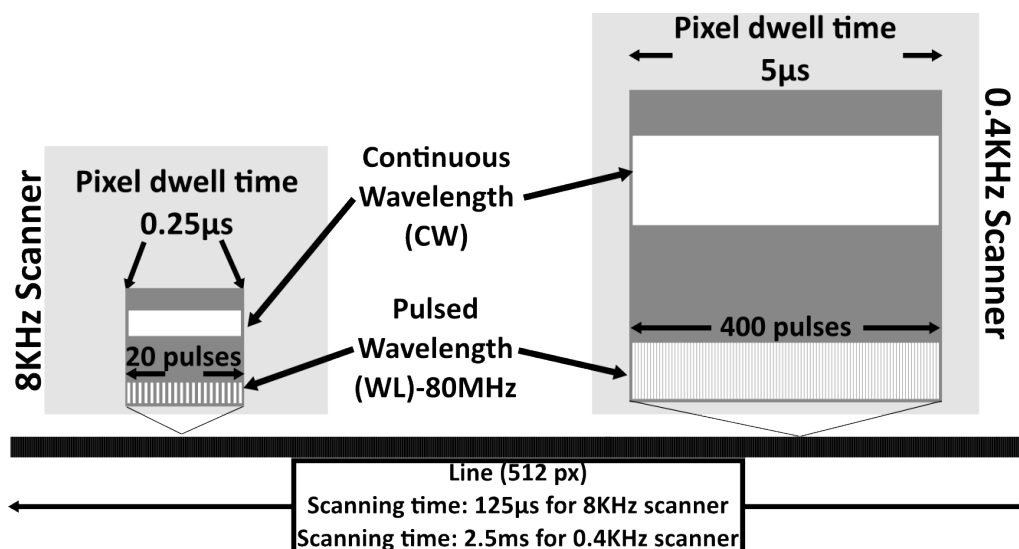


Figure 18 – Schematic representation of the respective settings for each line scan. The use of resonant scanner (8 kHz) resulted in a short line scanning time (125 μ s for 512 x 512 pixel images). In this case, during the pixel dwell time (0.25 μ s) the pulsed (at 80 MHz) white light laser excites fluorochromes with 20 pulses per pixel, while the argon laser (CW) is continuously on. The use of the 20 times slower scanner (0.4 kHz) raises the line (512 pixels) scanning time to 2.5 ms, meaning that the pixel dwell time is 5 μ s. During this time period there is a constant excitation with the argon laser (CW) or 400 pulses from the pulsed WL laser.

2.10.4 Image analysis

For each different combination of settings, the scratch closure speed was measured from the acquired data as described in 2.9.1.

Concerning the calculation of acquired fluorescent intensity reduction, we measured the mean gray value of a manually selected region at the migration front of the scratch, at time point 0 and then after 100 min of acquisition. The mean gray value measured with FIJI is independent by the size of the selected region. However, special attention was taken in order to avoid selecting intercellular areas lacking fluorophores. Then, with the mean gray values from time point 0 and 100 (G_0 and G_{100} , respectively) we were able to calculate the % of the fluorescent intensity reduction (FIR) with equation 21. At least 4 different time-lapse acquisitions, derived from 3 different experimental dates for each combination of hardware settings, were used for the quantification of FIR.

$$\%FIR = \left(\frac{G_0 - G_{100}}{G_0} \right) \cdot 100 \quad (21)$$

2.11 Statistical analysis

Multiple measurements were obtained for each experiment and for each cell line used. Results are shown as mean \pm standard error of the mean (SEM). The comparison of two independent population means inferred from two or more experiments was conducted by applying the Student's t-test and p values less than 0.05 were considered significant. For the statistical analysis of the results we used the Excel software package (Microsoft, Redmond, USA). In all graphs the statistical significance is represented with * as shown in Table 6.

| | |
|------------|------------------------------------|
| ns | $p\text{ value} > 0.05$ |
| * | $0.01 < p\text{ value} \leq 0.05$ |
| ** | $0.001 < p\text{ value} \leq 0.01$ |
| *** | $p\text{ value} \leq 0.001$ |

Table 6 – Representation of statistical significance in diagrams

3 Results

3.1 Electrophysiology

The fluorescence intensity correlated with the $K_v10.1$ current, where higher mVenus fluorescence corresponded with higher $K_v10.1$ -current (Figure 19). This correlation confirmed that the chimeric $K_v10.1$ -mVenus channels were functional and properly placed at cellular membrane.

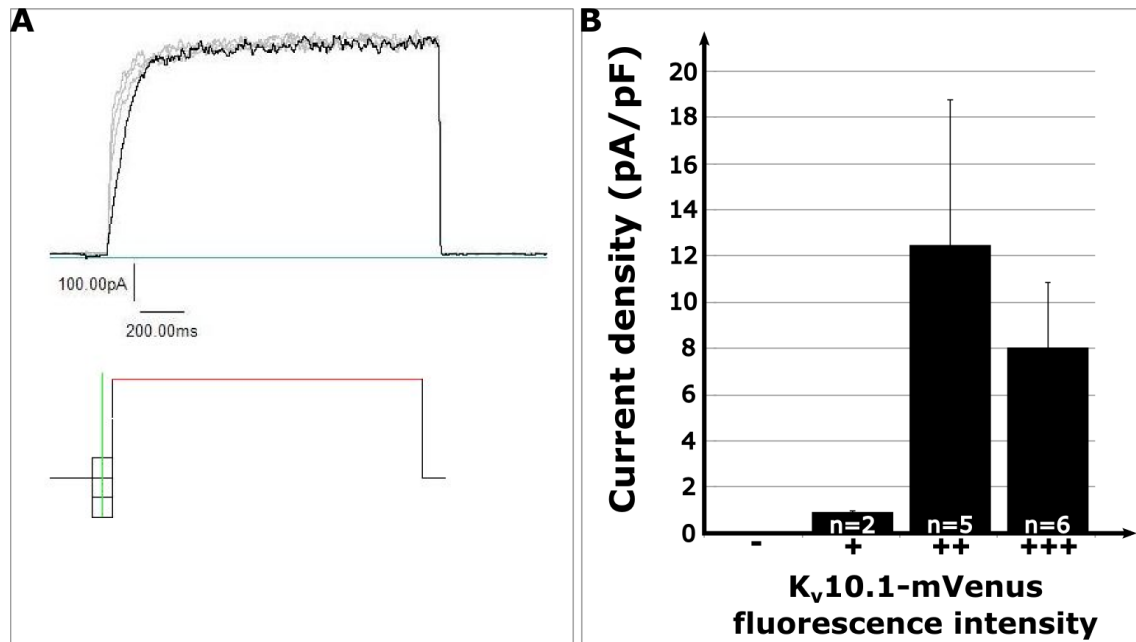


Figure 19 – Typical $K_v10.1$ current characterized by a Cole-Moore shift can be measured on the plasma membrane of HT-1080 cells stably expressing $K_v10.1$ -mVenus. (A) Upper part of the figure shows a representative $K_v10.1$ current from one recording. Below, the voltage protocol used to stimulate the current is shown. The cells were held at -60 mV and voltage steps of 20 mV over the range from -100 to -40 mV lasting for 1600 ms (only 100 ms is shown) were applied. The cell is then depolarized to $+40$ mV to activate the $K_v10.1$ current. (B) For different cell populations with varied fluorescent intensities (low, medium, high and very high also indicated by -, +, ++ and +++, respectively), the portion of cells which have surface $K_v10.1$ current are 0% ($n=15$), 13% ($n=16$), 30% ($n=20$) and 38% ($n=16$) respectively. The current densities ($\text{pA/pF} \pm \text{std}$) are 0 , 0.92 ± 0.06 ($n=2$), 12.48 ± 6.28 ($n=5$) and 8.04 ± 2.79 ($n=6$) respectively. Data acquired by Dr. Ye Chen.

3.2 Molecular biology

The $K_v10.1$ overexpression in HT-1080- $K_v10.1$ -mVenus cells in respect to the mVenus (control) cells has been shown with real-time PCR, where the transferrin receptor expression was used as a reference and the results were normalized to the respective ratio of a calibration sample. As shown in Figure 20, the *KCNH1* expression levels are significantly higher for $K_v10.1$ -mVenus overexpressing cells, revealing a successful and stable transfection.

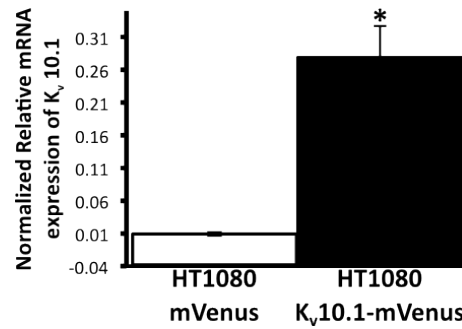


Figure 20 – The normalized expression level of *KCNH1* gene in HT-1080-K_v10.1-mVenus cells is significantly higher (p value 0.029) than in HT-1080-mVenus cells.

3.3 Biochemistry

3.3.1 Fluorescent detection from gel

The detection of the mVenus fluorescence derived, either from the free mVenus expressed in control cells, or from the chimeric K_v10.1-mVenus expressed in HT-1080-K_v10.1-mVenus cells, revealed the overexpression of mVenus tagged K_v10.1 protein with a molecular weight between 134 and 154 kDa, as expected for the glycosylated isoforms of the ion channel [Napp et al. (2005)], indicated with a blue arrow in Figure 21. Moreover, with this detection we were able to ascertain the overexpression of the mVenus fluorochrome from HT-1080-mVenus cells as revealed by the thick and intense bands below the marker for 25 kDa (red arrow in Figure 21).

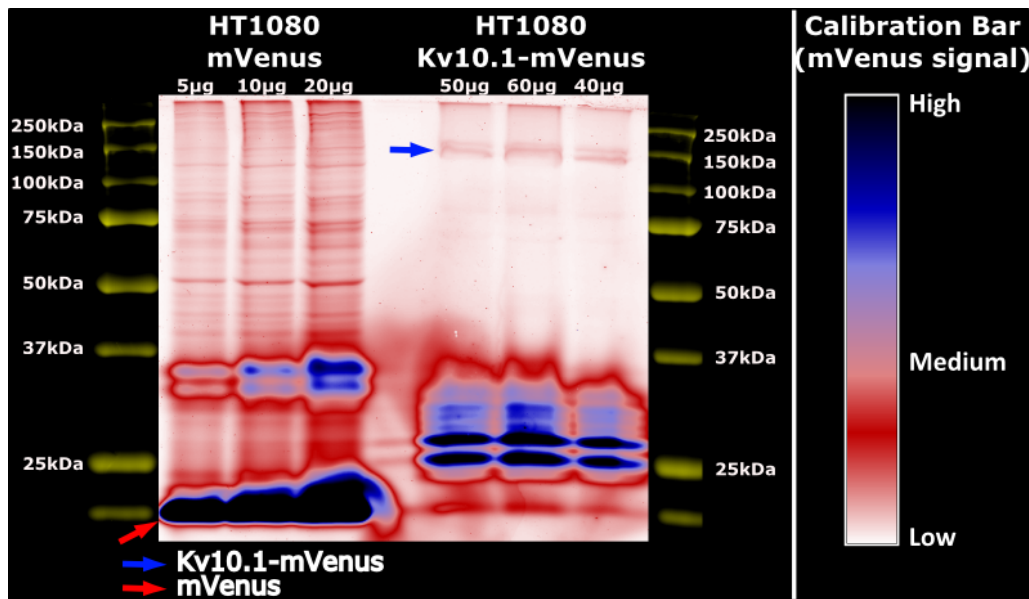


Figure 21 – Fluorescence detection of the free mVenus (red arrow) and $K_v10.1$ -mVenus (blue arrow) chimeric proteins expressed in HT-1080-mVenus and HT-1080- $K_v10.1$ -mVenus cells, respectively. Proteins were separated by electrophoresis in a Li-SDS gel and the mVenus fluorochrome was excited with the 488 nm wavelength of the argon laser of the Typhoon gel imager (signal in red, blue or black as shown at the calibration bar). For the protein ladder we used the 633 nm excitation from the He-Ne laser of the system (yellow signal at the edges of the gel).

From this detection, we can also conclude that the expression levels of the free mVenus fluorochrome are very high in our control cells, indicated by the intense signal of mVenus, even when we loaded 10 times less total protein extract (5 μ g; second lane from the left in Figure 21). On the other hand the levels of $K_v10.1$ -mVenus protein are much lower as seen by the low fluorescent signal (blue arrow in Figure 21). These findings confirm the electrophysiology and molecular biology experiments and also the observation with confocal microscopy, where the fluorescent signal from HT-1080- $K_v10.1$ -mVenus cells was less intense than in the case of our control cells, using the same acquisition settings.

Unspecific fluorescent signals (double bands between 25 and 37 kDa markers in Figure 21) can be interpreted as mVenus fragments or mVenus dimers not separated by the electrophoretic procedure.

3.3.2 Immunoprecipitation and Western blot

As a further proof of the expressed mVenus and $K_v10.1$ -mVenus proteins, we performed an immunoprecipitation of mVenus using an anti-GFP antibody (that specifically targets mVenus) as described in 2.4.5, followed by Western blotting with an antibody against $K_v10.1$ (targeting the C-terminal region of the channel) and also with an anti-GFP antibody as described in 2.4.6.

Membrane immunoblotting with the anti- $K_v10.1$ antibody, generated a band just be-

low the 150 kDa marker for the extract from HT-1080- $K_v10.1$ -mVenus cells, which corresponds to the chimeric $K_v10.1$ -mVenus protein (single arrowheads in left panel of Figure 22). This band (even though not so sharp) appeared after the membrane blotting, also at the non-immunoprecipitated input of HT-1080- $K_v10.1$ -mVenus extracts. Unfortunately, since the expression level of $K_v10.1$ in HT-1080-mVenus cells is very low (Figure 20), no band was visible for non-IP HT-1080-mVenus extract after anti- $K_v10.1$ blotting.

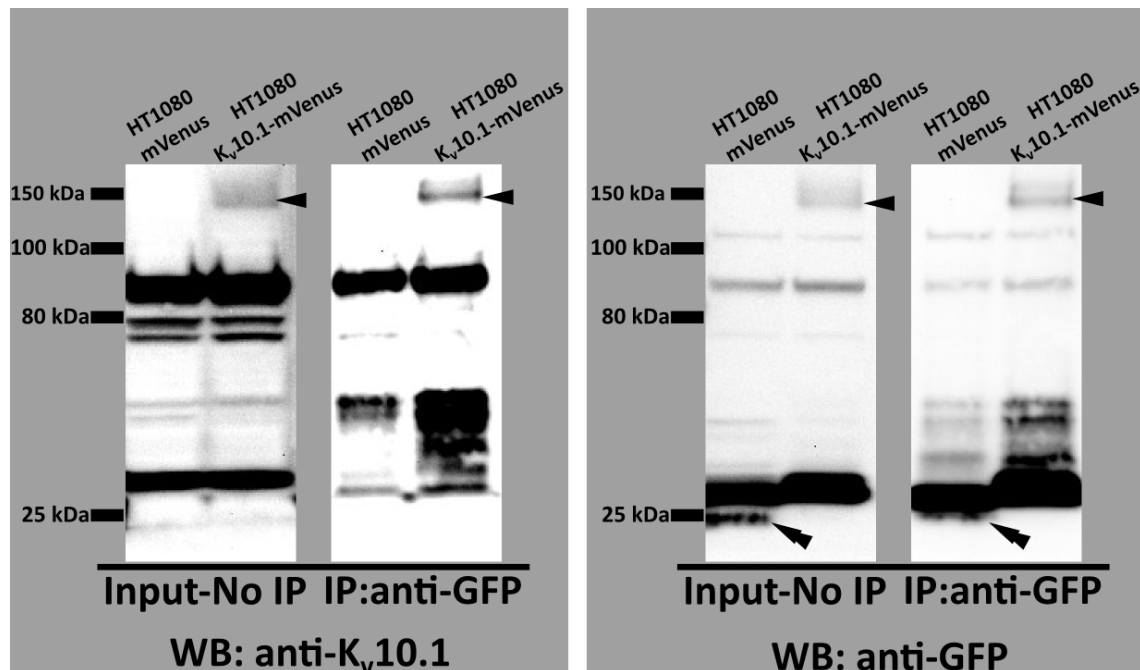


Figure 22 – Immunoprecipitation with anti-GFP and immunoblotting with anti- $K_v10.1$ (left) and anti-GFP (right), shows the overexpression of mVenus (double arrowheads at 24kDa) and $K_v10.1$ -mVenus (single arrowheads below 150kDa) in HT-1080-mVenus and HT-1080- $K_v10.1$ -mVenus cells respectively.

Moreover, the membrane blotting with anti-GFP not only confirmed the co-precipitation of $K_v10.1$ -mVenus described above, but also we were able to detect the expressed mVenus from HT-1080-mVenus extracts, just below the 25 kDa marker (double arrowheads at right panel in Figure 22).

With this experiment, we were able to confirm and enhance the findings of the gel fluorescent detection with the Typhoon system, revealing the successful and stable transfection of HT-1080 cells with either the mVenus fluorochrome (control cells) or with the $K_v10.1$ -mVenus chimeric construct.

3.4 $K_v10.1$ localization

Live, EGFP-actin and $K_v10.1$ -DsRed2 co-expressing HeLaSS6 cells, grown on a fibronectin-coated glass surface, formed EGFP-actin stress fibers and contained the typical, spotted appearance of $K_v10.1$ -DsRed2 positive endosomes as reported by Ninkovic

et al. (2012). Figure 23 (arrows in B₁) illustrates filamentous EGFP-actin-rich structures that converge onto common points, which is characteristic of focal adhesion (FA) site-rooted stress fibers [Wolfenson et al. (2009)]. B₂ in Figure 23 (DsRed2 channel), shows that $K_v10.1$ -DsRed2, acquired during live imaging, also localized near these adhesion sites (arrows at identical positions in B₁ and B₂).

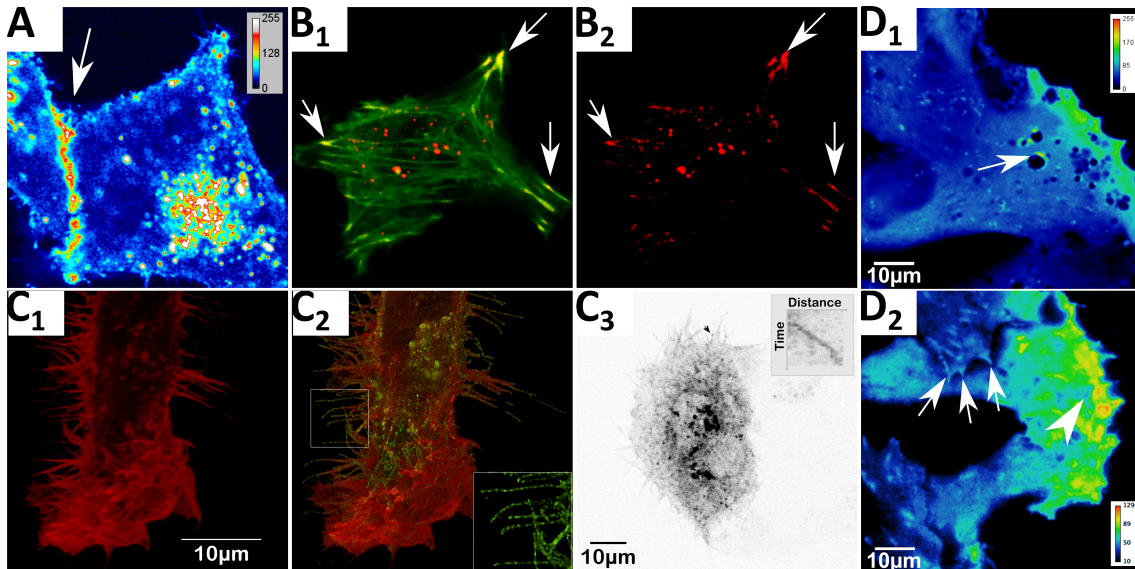


Figure 23 – (A) $K_v10.1$ -mVenus aggregated at the cell-cell interface when expressed in neighboring cells. (B₁-B₂) FA sites (arrows) revealed by EGFP-Actin stress fibers (B₁; green pixels) and $K_v10.1$ -DsRed2 (B₁ and B₂; red pixels) revealed overlapping localization of $K_v10.1$ with FA sites. A phalloidin stain (C₁) revealed that EGFP- $K_v10.1$ (inset of C₂) localized to filopodia (C₂). Additional live cell imaging studies revealed an anterograde transport of $K_v10.1$ (black arrow in C₃) into filopodia (kymograph inset in C₃). Migrating cells at the front of the scratch imaged with spinning disk CLM (D₁) and in TIRF mode (D₂). Cells shown at B and C are HeLa. Cells shown at A and D are HT-1080- $K_v10.1$ -mVenus. Images acquired by Dr. M. Mitkovski.

TIRF live-imaging microscopy was employed to further investigate $K_v10.1$ localization to adhesion sites. HT-1080 cells stably transfected with $K_v10.1$ -mVenus, located at a scratch assay migration front, were imaged over time. In this experiment, we observed the localization of $K_v10.1$ -mVenus at the lower membrane (~ 100 nm). Regular flashes of mVenus signal in time indicate transport of $K_v10.1$ -mVenus to the membrane (data not shown). The striped appearance of $K_v10.1$ -mVenus at the lower cell membrane is indicative of its localization within FA sites (white arrows in D₂ of Figure 23).

Filopodia are F-actin rich cellular processes, often located at the cell migration front and can be visualized in fixed cells with fluorescently labeled phalloidin. C₁ of Figure 23 shows one such stain, revealing EGFP- $K_v10.1$ (green pixels in C₂ of Figure 23) aggregates localized along filopodia. Moreover, live imaging experiments revealed an anterograde transport of EGFP- $K_v10.1$ along filopodia showing the dynamic nature of this process (kymograph inset in C₃ of Figure 23).

Live imaging with K_v10.1-mVenus overexpressing HT-1080 cells revealed that K_v10.1-mVenus localizes in the cell-cell membrane interface (A of Figure 23).

3.5 Cell migration

As described in 2.9.1 we studied cell migration in the context of the scratch assay for both types of cells (HT-1080-mVenus and HT-1080-K_v10.1-mVenus). First, in order to choose the optimal acquisition settings that allowed us to have the best signal with the minimum consequences in cell migration speed, we studied the effect of different combinations of hardware settings (Table 5) on the scratch closure speed (SCS) of HT-1080-mVenus cells. SCS as defined with equation 7 was calculated from the linear slope portion of the plotted scratch area over time, as indicated in Figure 8. Moreover, after tracking a representative number of cells from the leading edge of scratch assays, we were able to quantify specific migration characteristics of individual cells, using the equations described in Table 3.

3.5.1 Effect of stimulation / acquisition settings on scratch closure speed

Increased energy density causes increased cell migration rate The increased energy density delivered to samples at each scan was accompanied by an increased migration rate of cells (expressed as SCS in $\mu\text{m}^2/\text{min}$). This rise in cell migration speed appeared in all acquisition combinations used in this study as shown in Table 7. Additionally, in some cases the maximum energy density used per scan ($4.905 \mu\text{J}/\text{cm}^2$) caused a decreased migration (SCS) of cells reflecting a non-physiological behavior and inhibition of cell motility.

| Energy Density ($\mu\text{J}/\text{cm}^2$) | Scratch Closure Speed ($\mu\text{m}^2/\text{min}$) | | | | | | Migration & Phototoxicity Scale |
|--|--|------------------|-----------------|------------------|--------------------|--------------------|---------------------------------|
| | CW 8kHz (multi) | CW 8kHz (single) | WL 8kHz (multi) | WL 8kHz (single) | CW 0.4kHz (single) | WL 0.4kHz (single) | |
| A | B | C | D | E | F | G | H |
| 0.948 | 353 | 370 | 405 | 435 | 387 | 395 | Low |
| 1.581 | 367 | 390 | 435 | 453 | 405 | 417 | Medium |
| 2.453 | 369 | 402 | 450 | 480 | 412 | 435 | High |
| 4.905 | 396 | 426 | 475 | 404 | 381 | 391 | Inhibition |

Table 7 – Scratch Closure Speed is affected by the amount of energy density delivered to the sample during live imaging. Increased energy density caused an increase in SCS in most different combinations of hardware settings. In some cases the higher energy density delivered to the sample caused inhibition of cell migration due to non-physiological behavior of cells. The pulsed excitation (WL) always causes an increased migration speed compared with continuous wavelength excitation (CW), as well as the single acquisition mode versus multiple acquisition. The slower scanning speed (0.4 kHz) seems to have the same effect on SCS despite the different types of lasers and seems to cause inhibition of cell migration at higher energy density levels. Column H indicates the color-coded scale of cell migration and phototoxicity effects. SCS numbers are the average values from each combination of hardware settings, performed in triplicates.

Pulsed laser increases cell migration speed The use of White Light Laser (WL - columns D, E and G of Table 7) as an excitation source (at 514 nm) for the mVenus-expressing HT-1080 cells, caused an increased migration speed compared with the use of continuous laser emitting at 514 nm (CW - columns B, C and F of Table 7) in all different combinations of scanning speeds and accumulation settings. Moreover, the comparison of the same scanning speed and accumulation settings revealed that the use of the pulsed laser, lead to a cell migration speed increase.

Scanning speed affects cell migration Due to the fact that we used the conventional scanner with a scanning speed (0.4 kHz) 20 times slower than the resonant scanner (8 kHz), the use of slow scanning in combination with multiple accumulation was not possible for live image acquisition, while maintaining a time interval of 150 sec. For this reason, we are only able to compare cell migration speed between slow (columns F and G of Table 7) and fast (columns C and E of Table 7) scanning, only under single accumulation mode regime.

Interestingly the effect of scanning speed in cell migration, differs for the two types of lasers used in this study. Specifically, it seems that for the case where continuous wavelength was applied, the fast scanning speed affects less the scratch closure rate than the slow scanning speed (column C versus column F of Table 7, respectively). The opposite seems to happen in the case of the pulsed laser, since with the slower scanning mode (column G) cells migrate slower than in the case of fast scanning (column E) mode.

Single accumulation mode increases cell migration speed As mentioned before, the multiple accumulation settings were used only in combination with the resonant scanner (8 kHz). After comparison of multiple accumulation settings (columns B and D of Table 7) with single accumulation settings (columns C and E of Table 7, respectively), it is seen that single accumulation mode with the use of either pulsed or continuous wavelength increases scratch closure speed.

Increased cell migration correlates with increased fluorescence intensity reduction

After the measurement of mean gray value reduction (equation 21), we were able to observe that the hardware settings combinations that favored an increased SCS, were also effective for an increased reduction of the acquired fluorescent signal during the first 100 min of acquisition. More specifically, we were able to discover that increased migration speed was accompanied by a higher reduction of acquired fluorescence intensity over time. Interestingly, the comparison of the two heat-map tables 7 and 8, matches perfectly, with the exception of column D. There, the combination of pulsed laser excitation with the fast scanner under multiple acquisition mode, seems to promote migration, but with a small reduction in fluorescence intensity.

| Energy Density ($\mu\text{J}/\text{cm}^2$) | Fluorescence Intensity Reduction (%) | | | | | | Fluorescence Intensity Reduction Scale |
|--|--------------------------------------|------------------|-----------------|------------------|--------------------|--------------------|--|
| | CW 8kHz (multi) | CW 8kHz (single) | WL 8kHz (multi) | WL 8kHz (single) | CW 0.4kHz (single) | WL 0.4kHz (single) | |
| A | B | C | D | E | F | G | H |
| 0.948 | 12.5 | 18.6 | 15.1 | 27.0 | 24.4 | 23.7 | Low |
| 1.581 | 13.0 | 21.3 | 15.8 | 28.3 | 23.2 | 25.6 | Medium |
| 2.453 | 13.7 | 23.5 | 16.5 | 29.7 | 26.2 | 27.7 | |
| 4.905 | 15.2 | 27.1 | 17.7 | 31.6 | 30.2 | 30.2 | High |

Table 8 – The reduction of fluorescence intensity is proportional to the amount of energy density delivered to the sample during live imaging, in all different combinations of hardware settings. The mVenus bleaching is more likely under pulsed laser excitation (WL), as well as the single acquisition mode versus multiple acquisition. The slower scanning speed (0.4 kHz) seems to have the same effect on fluorescence intensity reduction despite the different types of lasers. Column H indicates the color-coded scale of acquired fluorescence intensity reduction.

3.5.2 $K_v10.1$ increases scratch closure speed

As described in 2.7.3, we used identical acquisition settings for both cell types for the recording of a number of scratch assays, which were then subjected to semiautomatic analysis that ultimately calculated the SCS. This calculation revealed that the $K_v10.1$ overexpression in HT-1080 cells increased the scratch closure rate, while its blockage with 0.01 $\mu\text{g}/\text{ml}$ mAb56 significantly inhibited this increased migration. Application of

1 μM AST lead to an SCS decrease and effectively rescued the effect introduced by the $\text{K}_v10.1$ overexpression (Figure 24).

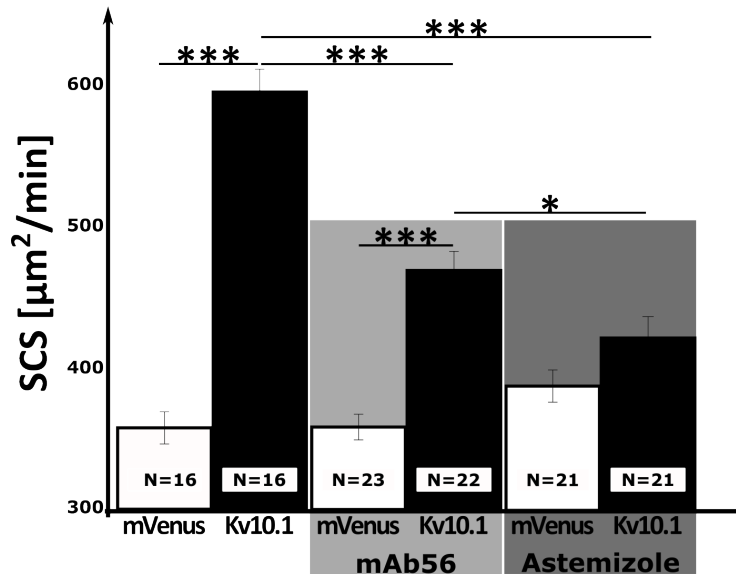


Figure 24 – HT-1080-mVenus cells (white bar) close the scratch at a significantly lower rate ($355.7 \frac{\mu\text{m}^2}{\text{min}}$) than HT-1080- $\text{K}_v10.1$ -mVenus cells (black bar- $593.9 \frac{\mu\text{m}^2}{\text{min}}$) p value= 2.24×10^{-12} . After the incubation with $0.01 \mu\text{g/ml}$ mAb56, mVenus cells retain their scratch closure rate ($356.3 \frac{\mu\text{m}^2}{\text{min}}$), while $\text{K}_v10.1$ cells significantly (p value= 1.03×10^{-6}) reduce their SCS ($467.4 \frac{\mu\text{m}^2}{\text{min}}$). Their between difference remained statistically significant with a p value= 4.89×10^{-8} . In the case of incubation with AST ($1 \mu\text{M}$), mVenus cells increased (not significantly) their scratch closure rate ($385.3 \frac{\mu\text{m}^2}{\text{min}}$) while $\text{K}_v10.1$ cells appeared to have a highly significant (p value= 2.28×10^{-9}) reduction of scratch closure speed compared with $\text{K}_v10.1$ cells without any blocking agent, down to $415 \frac{\mu\text{m}^2}{\text{min}}$, statistically the same with the control treated cells. AST showed a significantly (p value= 10^{-2}) greater inhibition of the $\text{K}_v10.1$ -enhanced scratch closure speed when compared to the mAb56 blockage. Sample number (N) is the number of different fields of view quantified in each case.

3.5.3 Effect of $\text{K}_v10.1$ on individual cell migration

The track coordinates of the respectively marked cells were extracted and plotted using a common origin point (Figure 25). Therein, the plots reveal that $\text{K}_v10.1$ overexpressing cells have longer and more dispersed routes, compared with control cells during the same period of time. The blockage with mAb56 or AST appears to decrease these differences.

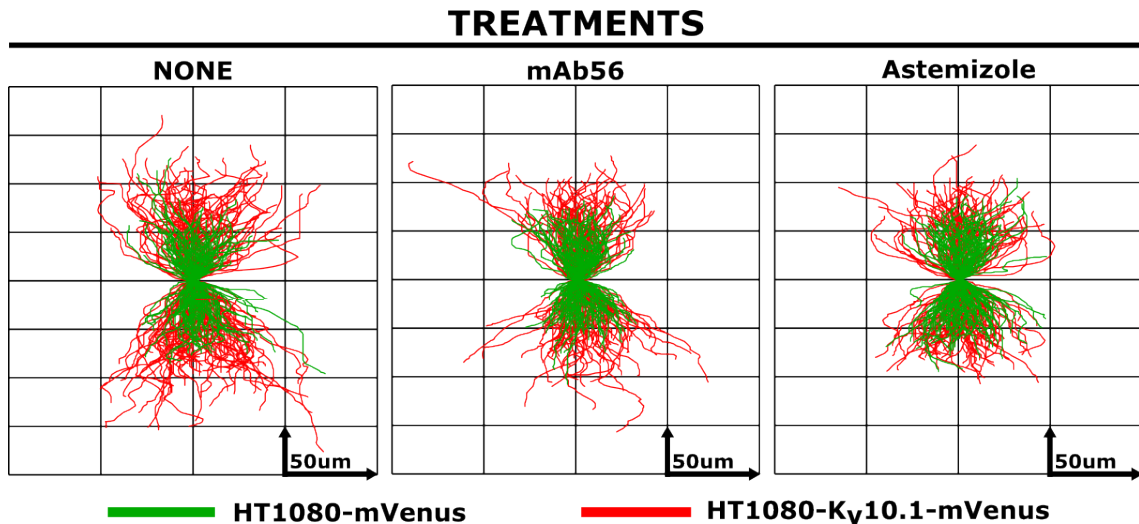


Figure 25 – The tracks of individual migrating cells from the leading edge of the scratch, plotted using a common origin point, reveal the differences in cell migration pattern between HT-1080-mVenus (green lines) and HT-1080-K_v10.1-mVenus cells (red lines) before and after the mAb56 or AST blocking.

In order to quantify these apparent differences in the migration pattern between mVenus and K_v10.1-mVenus overexpressing cells, we calculated the average final migration angle with respect to the x-axis (horizontal axis of the field-of-view), the maximum migration speed, the accumulated distance, the mean squared displacement and the straightness of each cell route, using the previously mentioned equations (16, 14, 17, 19 and 18, respectively). The fact that the general task of scratch closure was not affected by K_v10.1 overexpression or blocking thereof is reflected in the overall lack of difference in the final migration angle (90°; orthogonal to the major scratch axis, C in Figure 26).

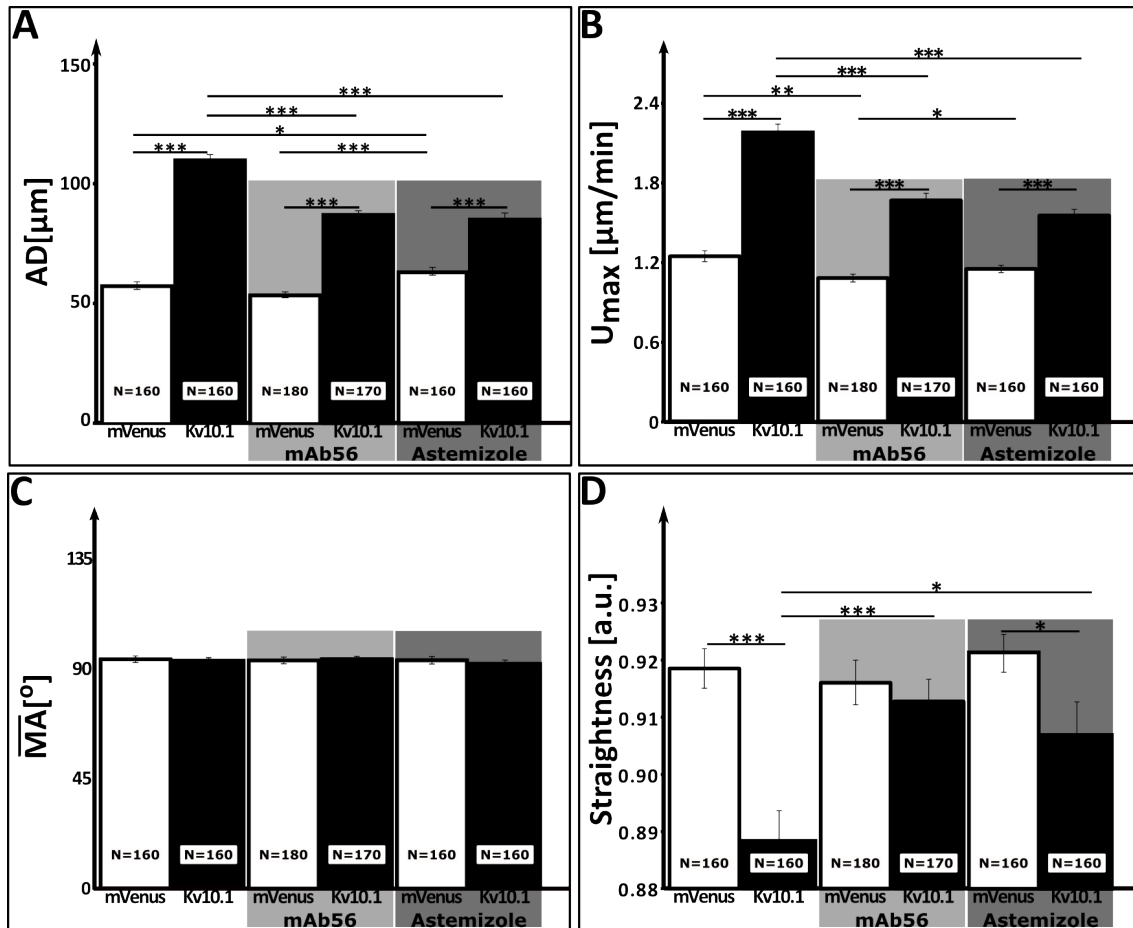


Figure 26 – (A) The accumulated distance (AD) was significantly (p value= 1.5×10^{-56}) greater for $K_v10.1$ cells ($110.01\mu\text{m}$) than the one of mVenus cells ($57.53\mu\text{m}$). Incubation with mAb56 or AST caused a significant AD reduction (p value 4.8×10^{-15} and 2.3×10^{-15}) of $K_v10.1$ cells ($86.82\mu\text{m}$ and $86.34\mu\text{m}$ respectively). The accumulated distance of mVenus cells after the treatment with mAb56 or AST remained significantly (p value 1.9×10^{-34} and 4.4×10^{-17}) lower than the one of $K_v10.1$ overexpressing cells ($53.64\mu\text{m}$ and $64.20\mu\text{m}$ respectively). (B) The average maximum migration speed (U_{max}) differed significantly between mVenus and $K_v10.1$ cells ($1.26 \frac{\mu\text{m}}{\text{min}}$ versus $2.16 \frac{\mu\text{m}}{\text{min}}$) with a p value of 1.8×10^{-29} . mAb56 blocking caused a U_{max} speed decrease in both cell types at $1.08 \frac{\mu\text{m}}{\text{min}}$ and $1.68 \frac{\mu\text{m}}{\text{min}}$ respectively with their between difference having a p value of 4.3×10^{-19} . The maximum migration speed reduction was significant for mVenus (p value 10^{-3}) and for $K_v10.1$ cells (p value 8.7×10^{-10}). With AST, the maximum migration speed decreased for both cell types at $1.14 \frac{\mu\text{m}}{\text{min}}$ and $1.56 \frac{\mu\text{m}}{\text{min}}$, respectively. This reduction was not significant for mVenus cells treated with AST, but it had a great significance for $K_v10.1$ cells (p value 7.9×10^{-15}). The difference in maximum migration speed between mVenus and $K_v10.1$ cells, incubated with AST, remained significant with a p value of 1.4×10^{-12} . (C) The average migration angle \overline{MA} for HT-1080-mVenus and HT-1080- $K_v10.1$ -mVenus cells was almost orthogonal to the scratch axis revealing that the task of wound closure in the scratch assay was not affected. (D) The straightness of cell routes expressed as the rate between the Euclidian and accumulated distance was significantly different (p value= 3×10^{-6}) between mVenus and $K_v10.1$ cells (0.92 versus 0.89, respectively). This difference disappeared after mAb56 blocking, since the straightness of $K_v10.1$ cell routes increased significantly (p value= 2.2×10^{-4}) to 0.91. The AST treatment increased slightly the straightness of mVenus control cell routes (straightness 0.92) and significantly (p value=0.01) the straightness of $K_v10.1$ cell trajectories (straightness 0.90), while their between difference remained statistically significant (p value= 2×10^{-3}). Sample number (N) is the number of individual cells, tracked in each case.

Additionally, $K_v10.1$ overexpression resulted in a greater maximum migration speed (B in Figure 26). However, the speed increase is reduced by mAb56 or AST treatment.

Faster HT-1080- $K_v10.1$ cell migration resulted in a greater accumulated distance, compared with HT-1080-mVenus cells during the same period of time, while it was reduced for HT-1080- $K_v10.1$ cells, after the blocking with mAb56 or AST (A in Figure 26).

Moreover, HT-1080- $K_v10.1$ cells migrate along significantly less straight routes than HT-1080-mVenus cells (D in Figure 26). However, mAb56 application rescued the effect generated by the $K_v10.1$ overexpression, while AST treatment only reduced this difference.

The overall effect of the $K_v10.1$ ion channel on the migration pattern can be presented by a MSD plot (Figure 27), with $K_v10.1$ overexpression resulting in a more exploratory behavior with more degrees of freedom, as indicated by the different intercepts of the power fitted trend lines. This behavior changed after mAb56 or AST treatment. This MSD plot further confirms the observed dispersed routes in Figure 25.

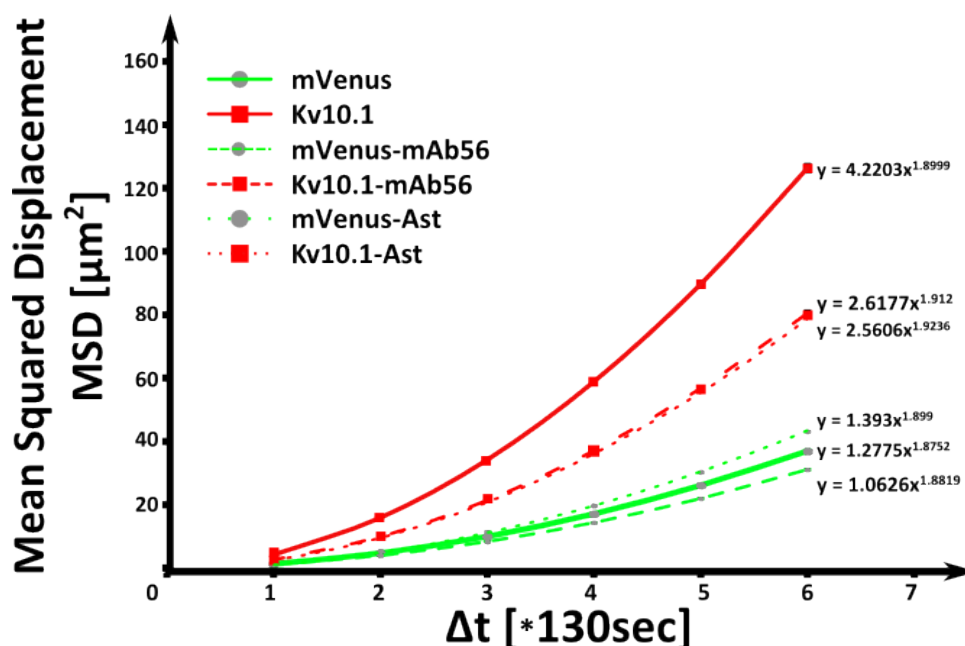


Figure 27 – The more dispersed routes of HT-1080- $K_v10.1$ cells (red lines) compared with the ones of HT-1080-mVenus (green lines) is reflected in an MSD diagram. This diagram also illustrates that the routes of HT-1080- $K_v10.1$ cells are less dispersed after mAb56 and AST blocking (dashed and dotted lines, respectively).

3.6 Cilia formation

The marked differences in migration pattern between HT-1080-mVenus and HT-1080- $K_v10.1$ -mVenus cells lead us to investigate the role primary cilia may play in this process. With this aim in mind, a number of scratch assays were fixed 1 h after introduction of the

scratch, and stained with anti-acetylated- α -tubulin-AlexaFluor[®]546 to mark the primary cilia and DAPI as a nuclear counterstain (Figure 28).

This staining revealed the absence of primary cilia in both types of HT-1080 cells, even after 24 h starvation (data not shown) and so the different migration patterns cannot be explained by the appearance of primary cilia. In both cell types (HT-1080-mVenus and HT-1080-K_v10.1-mVenus), the acetylated- α -tubulin staining revealed several midbodies connecting the separated daughter cells, indicating at least, a successful fixation and staining protocol.

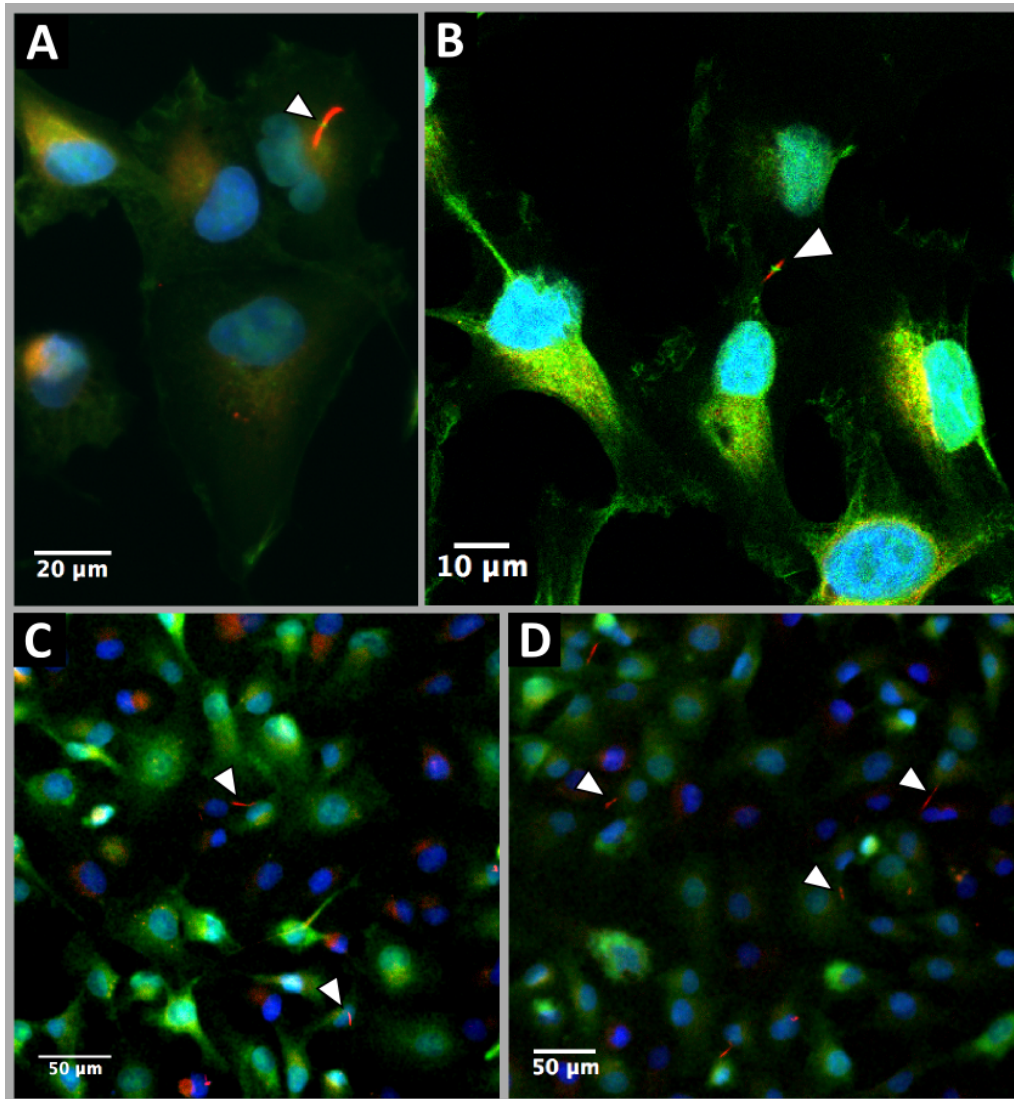


Figure 28 – A and B are HT-1080-mVenus cells while C and D are HT-1080-K_v10.1-mVenus cells. Blue signal comes from DAPI stained nuclei, green signal from mVenus expressed fluorochrome and red signal from anti-acetylated- α -tubulin-AlexaFluor[®]546. White arrowheads, indicate the presence of midbodies as stained with the anti-acetylated- α -tubulin. Several of these midbodies seem to be broken after the immunocytochemistry treatment.

3.7 Cell-cell adhesion

As is the case for mVenus-expressing HT-1080 cells, the $K_v10.1$ -mVenus expressing counterparts are capable of generating a confluent layer when cultured under *in vitro* conditions, such that no gaps are created between cells. Both cell types completely occupied the intercellular area before the migration stimulation (A and D in Figure 29). However, the differences between HT-1080-mVenus and HT-1080- $K_v10.1$ -mVenus cells, became visible immediately after the scratch introduction to the confluent cell layer (B and E in Figure 29). After the complete closure of the scratch, both cell types manage to form again a confluent layer without any apparent differences (C and F in Figure 29).

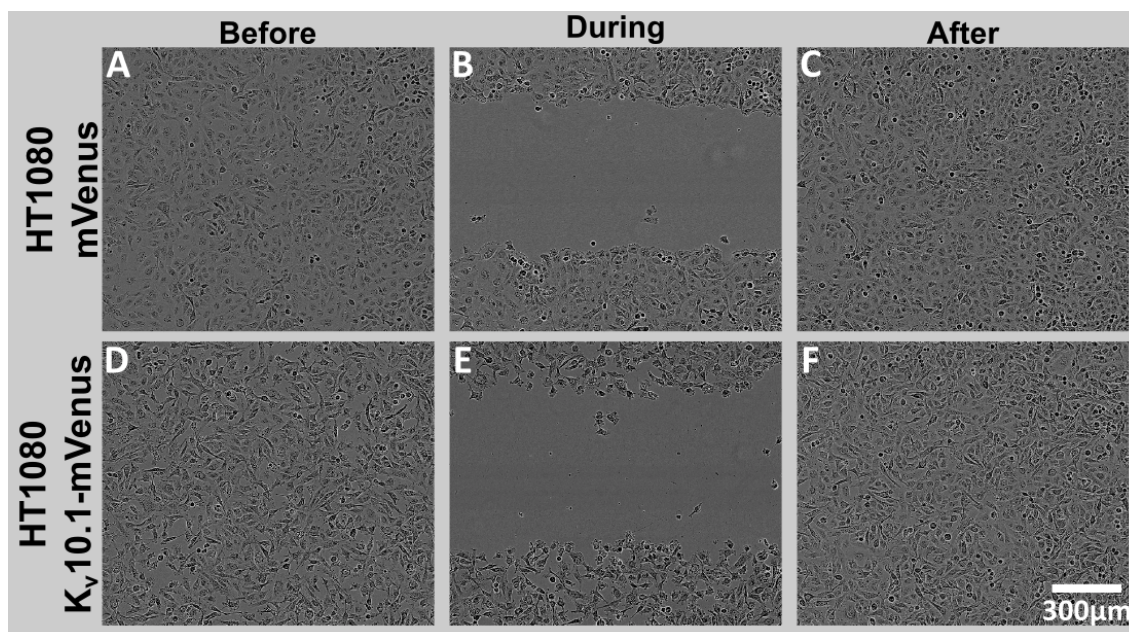


Figure 29 – Phase contrast images acquired with the IncuCyte™ ZOOM of HT-1080-mVenus (A, B and C) and HT-1080- $K_v10.1$ -mVenus cells (D, E, F) before the scratch introduction (A and D), during migration (B and E) and after the complete closure of the scratch (C and F), indicate that during a non-migratory state both cell types do not have any obvious differences concerning their shape, size and cell-cell adhesion ability.

Intercellular area measurements were used to estimate the difference in cell-cell adhesion between HT-1080-mVenus and HT-1080- $K_v10.1$ -mVenus overexpressing cells. The measured intercellular area (blue areas in Figure 9), generated only at the onset of cell movement, was significantly larger for HT-1080- $K_v10.1$ -mVenus cells. These measurements were normalized to the initial area occupied by cells in order to have a comparable intercellular-space-value that is independent of the initial gap width or the number of cells around the scratch (%MIA in equation 8).

The results revealed a significantly larger %MIA between migrating $K_v10.1$ cells (Figure 30) and mVenus control cells, indicating a deficit in cell-cell adhesion due to the overexpression of $K_v10.1$. In fact, migrating HT-1080- $K_v10.1$ cells were generating 2.5 times

more %MIA compared to HT-1080-mVenus cells.

The increased intercellular space, due to $K_v10.1$ overexpression, was significantly reduced upon exposure to channel blockers, such as the monoclonal antibody mAb56 or AST.

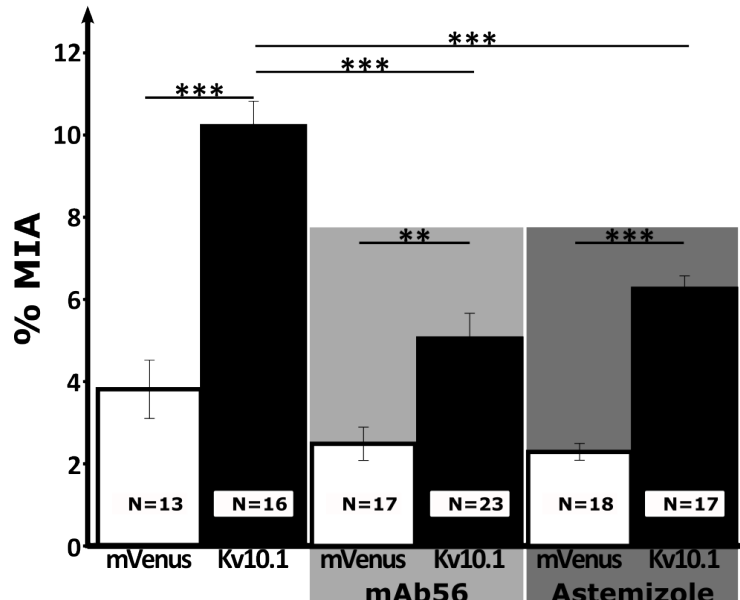


Figure 30 – The %MIA was significantly (p value= 3.3×10^{-7}) higher for HT-1080- $K_v10.1$ -mVenus cells (10.22%) compared with the one of HT-1080-mVenus cells (3.81%). After mAb56 or AST incubation, there was a significant (p value= 6.96×10^{-7} and p value= 6.38×10^{-6} respectively) reduction of the % maximum intercellular area for $K_v10.1$ overexpressing cells almost by half (5.05% and 6.25%). The reduction of the intercellular space of HT-1080-mVenus cells due to mAb56 or AST blocking (2.49% and 2.29% respectively), was not statistically significant. Sample number (N) is the number of different fields of view quantified in each case.

3.8 Cell-surface adhesion

Cell-surface adhesion for both HT-1080-mVenus and HT-1080- $K_v10.1$ -mVenus was measured in three different ways. Since TIRF experiments revealed a strong localization of $K_v10.1$ to the lamellipodial region (D_2 in Figure 23), we started by measuring the adhesive area at the lamellipodial region of migrating cells in the context of the scratch assay, using the IRM technique described in 2.9.2. Furthermore, we measured the adhesive ability of individual cells as a ratio of focal adhesion areas (areas that are closer than 40 nm to the glass surface) per footprint area, as well as the adhesion dynamics over time as described in 2.9.5.

3.8.1 Adhesive area at migration front

As described in 2.9.2, we managed to calculate the normalized, accumulated, adhesive area at the migration front, which is constant over time for mVenus and $K_v10.1$

overexpressing cells (linear slopes in Figure 31). However, the normalized adhesive area is significantly greater for HT-1080-mVenus cells when compared to HT-1080-K_v10.1-mVenus, which is reflected in the larger slope of the normalized, accumulated, adhesive area (Figure 31). This result indicates better lamellipodial-surface adhesion for migrating HT-1080-mVenus cells.

Interestingly, the mAb56 incubation rescued the effect of K_v10.1 overexpression in lamellipodial-surface adhesion of migrating cells, while AST had no effect on both cell types.

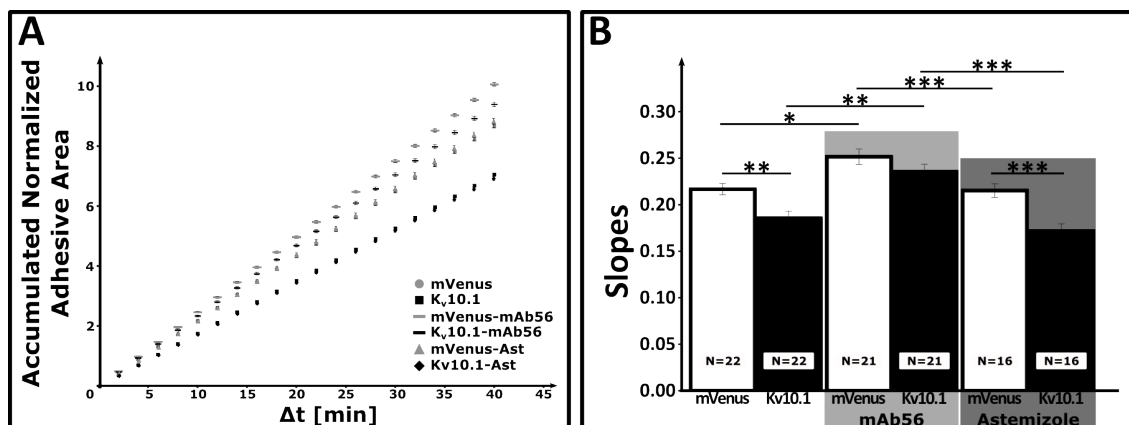


Figure 31 – (A) The adhesive area at the migration front for HT-1080-mVenus cells (grey circles) is always greater than the one of HT-1080-K_v10.1-mVenus cells (black squares) during the first 40 minutes of scratch closure. After the blocking with mAb56 (grey bars for mVenus and black bars for K_v10.1 cells), the normalized adhesive area of both cell types increased at similar level. AST blocking had no effect on the adhesive area for both mVenus and K_v10.1 cells (grey triangle and black polygon respectively). The error bars were calculated using a simplified formula as described by Ku (1966). (B) The slope of the accumulated adhesive area for HT-1080-mVenus cells ($0.22 \pm 6 \times 10^{-3}$) is significantly (p value= 2.6×10^{-3}) greater than the slope of HT-1080-K_v10.1-mVenus cells ($0.19 \pm 7.8 \times 10^{-3}$). A significant (p value= 1.6×10^{-2} and 3.8×10^{-3}) slope increase to 0.25 ± 10^{-2} and 0.24 ± 10^{-2} resulted after mAb56 incubation for HT-1080-mVenus and HT-1080-K_v10.1-mVenus cells respectively rescuing the effect of K_v10.1 overexpression. AST had no effect on the slope of the accumulated adhesive area for both types of cells.

3.8.2 Cell-surface adhesion ability

After calculating the membrane distances from the substrate using equation 6, the cell-surface adhesion ability of individual cells was quantified from DW-IRM images as described in 2.9.4. With these measurements, we were able to identify and measure area that participates in focal adhesion, since they were separated from the glass surface by less than 40 nm. The % of cell footprint area that is at a distance less than 40 nm from the substrate is indicative of cell-surface adhesion ability.

Interestingly, from these measurements we were able to see that the ability for surface adhesion of HT-1080-K_v10.1-mVenus cells was significantly less than the ability of control cells, confirming and reproducing the results obtained from the normalized adhesive

area at the lamellipodial region of the cells (Figure 32). Moreover, as in the adhesive area of the migration front, the adhesive ability of $K_v10.1$ -mVenus overexpressing cells was rescued after blocking of the channel with the mAb56, since there was a significant increase of the % of cell footprint that is available at the FA sites.

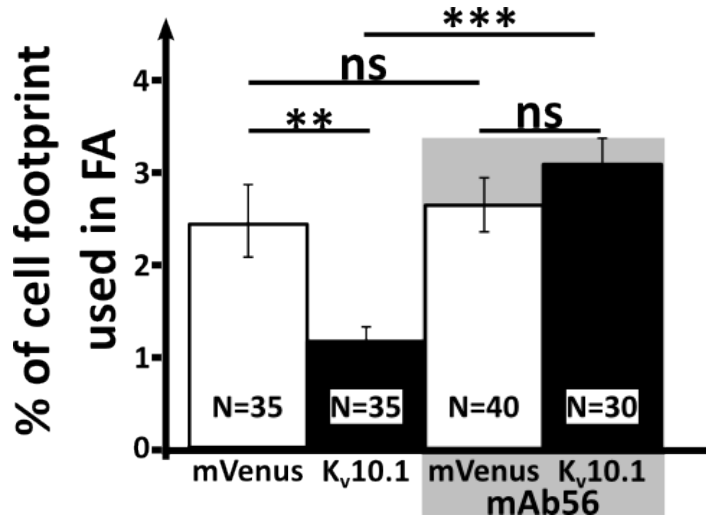


Figure 32 – The % of cell footprint used in FA sites for HT-1080-mVenus cells ($2.47 \pm 0.4\%$) is significantly (p value= 9×10^{-3}) greater than the one of HT-1080- $K_v10.1$ -mVenus cells ($1.23 \pm 0.1\%$). This effect of $K_v10.1$ overexpression was rescued after mAb56 incubation for HT-1080-mVenus and HT-1080- $K_v10.1$ -mVenus cells since the percentage of cell footprint area used in FA sites for $K_v10.1$ overexpressing cells increased significantly (p value= 2.6×10^{-5}) to $3.09 \pm 0.2\%$, without any significant difference from the respective % of HT-1080-mVenus cells ($2.64 \pm 0.2\%$) after mAb56 incubation. This % for the control cells, after mAb56 blocking, even though slightly increased compared to the one before the blockage, was significantly different. Sample number (N) is the total number of individual cells measured in each state.

3.8.3 Cell-surface adhesion dynamics

The cell-surface adhesion process dynamics of individual cells was monitored over time (2.8.3) and quantified as described in 2.9.5, based on a novel algorithm (See 6.2 for details).

After plotting the average measurements out of 7 individual HT-1080-mVenus and 5 HT-1080- $K_v10.1$ -mVenus cells, we were able to see that both cell types have the tendency to increase their footprint over time (A in Figure 33). Interestingly, in this study the control cells seemed to have a smaller (not-significant though) footprint than the $K_v10.1$ overexpressing cells (A in Figure 34).

The rate of protrusions and retractions varied slightly over time, but was mostly stable over time and higher for $K_v10.1$ overexpressing cells (B in Figures 33 and 34), showing that they tended to explore their surrounding more, by protruding and retracting their membranes at a higher rate than the control cells.

Additionally, after calculating the mean distance of different parts of cell membranes

from the substrate, we were able to see that the non-motile parts of the cells were anchored more closely to the surface, than the motile protruding and retracting parts. All the parts of HT-1080-K_v10.1-mVenus cells appeared higher, than the corresponding ones of HT-1080-mVenus cells (C in Figures 33 and 34), revealing a looser cell-surface adhesion.

Interestingly, the calculation of the average surface-membrane distance changes over time, showed a deficit of HT-1080-K_v10.1-mVenus cells in changing their cell-surface adhesion contacts, compared to their control counterparts. Their rates in protruding and retracting regions were significantly lower than the rates of HT-1080-mVenus cells. For both cell types the anchored non-motile regions were not changing their vertical position over the time of acquisition, since their rate of changing the distance from the surface was almost zero (D in Figures 33 and 34).

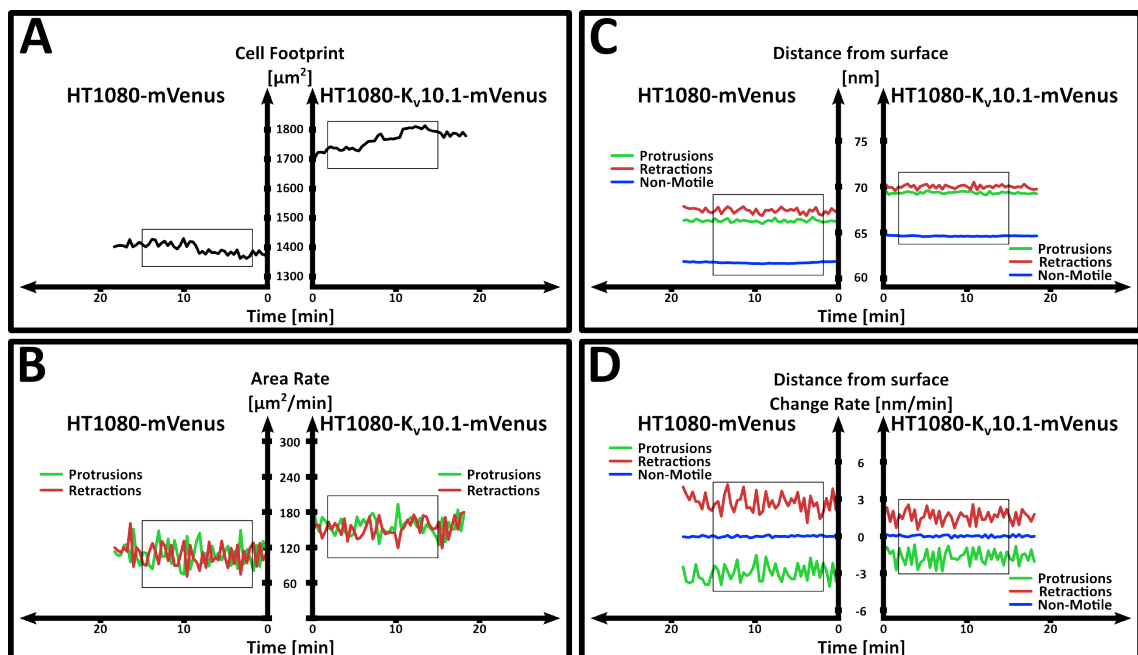


Figure 33 – (A) Cell footprints (in μm^2) over the time of live imaging. Both types of cells expand their footprints over time. (B) The protrusions and retractions rates (in $\mu\text{m}^2/\text{min}$) were stable over time for both HT-1080-mVenus and HT-1080-K_v10.1-mVenus cells. The rate of protrusions and retractions seems to be higher for the K_v10.1 overexpressing cells. (C) The average distances from surface over time are different for the distinct defined areas of each cell. The non-motile regions of cells are closer to the surface than the protruding and retracting regions for both types of cells. K_v10.1 overexpressing cells though, seem to have a greater overall distance from the substrate over time. (D) The average rate of vertical membrane movements are different for the defined cell areas. For both types of cells the non-motile parts of membrane appear to have almost no vertical movements, since their rate is around zero. The protruding areas appear to have negative rates meaning that they have the tendency to increase their distance from the surface, while the retracting areas seem to have the opposite tendency with movements towards to the substrate. Interestingly HT-1080-K_v10.1-mVenus cells appear to have lower rates of vertical movements. The lines in all line plots are the average measurements out of the monitoring of 7 HT-1080-mVenus and 5 HT-1080-K_v10.1-mVenus cells. The delineated areas represent the measurements used for the calculation of the average values plotted in Figure 34.

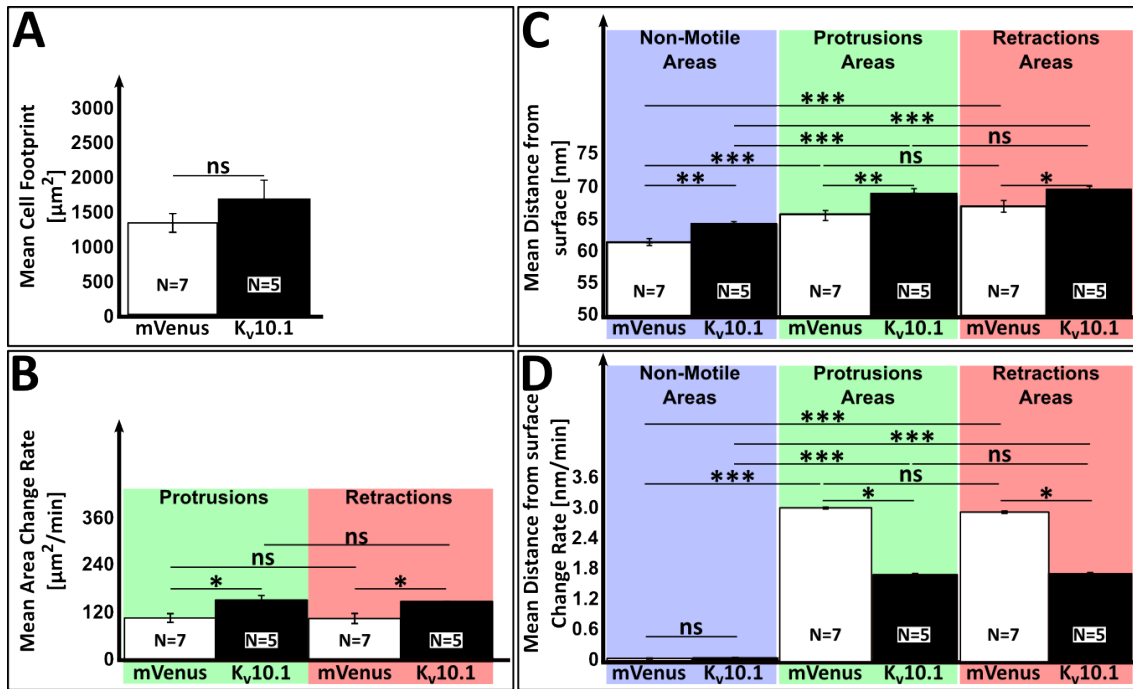


Figure 34 – (A) The average cell footprint (in μm^2) over the time of live imaging was not significantly (p value=0.26) different between HT-1080-mVenus ($1399.17 \pm 144.89 \mu\text{m}^2$) and HT-1080-K_v10.1-mVenus cells ($1767.56 \pm 260.25 \mu\text{m}^2$). (B) The mean rate of protrusions and retractions (in $\mu\text{m}^2/\text{min}$) was significantly lower for HT-1080-mVenus cells than the one for K_v10.1 overexpressing cells (p values 0.020 and 0.028 respectively). More specifically, the protrusion rate for control cells was $108.6 \pm 11.6 \mu\text{m}^2/\text{min}$ while for HT-1080-K_v10.1-mVenus cells was $155.6 \pm 12.2 \mu\text{m}^2/\text{min}$. The retraction rate was also lower for HT-1080-mVenus cells ($106.9 \pm 13 \mu\text{m}^2/\text{min}$) than the retraction rate of HT-1080-K_v10.1-mVenus cells ($151.8 \pm 11.6 \mu\text{m}^2/\text{min}$). The protrusion rate was not statistically different than the retraction rate for both cell types. (C) The non-motile areas of HT-1080-mVenus cells were significantly (p value= 2×10^{-3}) closer to surface (61.70 ± 0.5 nm) than the one of HT-1080-K_v10.1-mVenus cells (64.6 ± 0.4 nm). The mean distance of protruding areas for control cells (66.27 ± 0.7 nm) was also significantly lower (p value= 5.7×10^{-3}) than the one of K_v10.1 cells (69.33 ± 0.4 nm). For the retracting areas, the mean distance from substrate for HT-1080-K_v10.1-mVenus cells was significantly (p value=0.023) higher (70.00 ± 0.4 nm) than the one of HT-1080-mVenus cells (67.36 ± 0.9 nm). The protruding areas of HT-1080-mVenus and HT-1080-K_v10.1-mVenus cells were significantly larger (p values 4×10^{-4} and 6×10^{-5} respectively) than the non-motile areas but not significantly different than the retracting areas (p values 0.36 and 0.26 respectively). Moreover, the retracting areas were also significantly larger than the non-motiles areas for both types of cells (p values 2.4×10^{-4} and 2.1×10^{-5} respectively). (D) The rate of vertical membrane movements was close to zero for the non-motile areas of mVenus and K_v10.1-mVenus cells (2.7×10^{-5} and 3.8×10^{-3} nm/min respectively). Interestingly, this rate was significantly (p value=0.012) larger for the protruding areas of HT-1080-mVenus cells (2.92 ± 0.35 nm/min) compared with the respective rate of HT-1080-K_v10.1-mVenus cells (1.69 ± 0.08 nm/min). The respective rate of the retracting areas was also significantly (p value=0.012) higher for control cells (2.69 ± 0.32 nm/min) compared with K_v10.1 overexpressing cells (1.57 ± 0.11 nm/min). The vertical movement rate for protruding areas for HT-1080-mVenus and HT-1080-K_v10.1-mVenus cells were significantly higher (p values 1.6×10^{-4} and 4.3×10^{-5} respectively) than the ones of non-motile areas, but not different (compared as absolute values) than the rates of retracting areas which were also significantly higher (p values 1.5×10^{-4} and 1.8×10^{-4} respectively) than the almost zero rate of non-motile areas. For all these rates, the absolute values have been plotted. The mean values in these plots were derived by averaging the respective values in the delineated areas of Figure 33. Sample numbers (N) are the number of individual cells monitored with DW-IRM.

3.8.4 Focal Adhesion Kinase in FA sites

In order to validate our IRM measurements and especially the membrane height determination, we fixed HT-1080-mVenus and HT-1080-K_v10.1-mVenus cells as described in 2.5.2 and stained FAK. We then acquired IRM data and also the emission from the anti-FAK-AlexaFluor[®]647 fluorochrome. The IRM intensities were then converted to membrane-surface distances (using equation 6) and the converted images were overlaid with the signal from FAK as shown in Figure 35.

This reported, as expected, that the FAK protein is mainly localized in focal adhesion (FA) sites, where it participates in the formation of focal contacts. These sites were the areas whose location was less than 40 nm from the substrate, as quantified from the IRM signal. The co-localization of these sites with the FAK proteins, as shown in B of Figure 35, validates the accuracy of our calculations concerning the distance of cell membrane from the surface based on the IRM signal intensity.

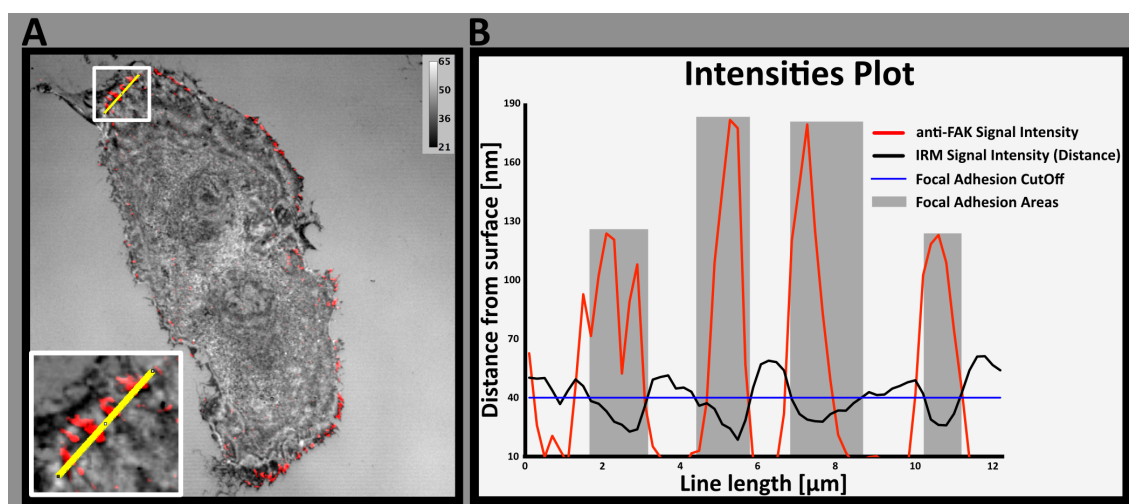


Figure 35 – Representative example of an HT-1080-mVenus cell showing Focal Adhesion Kinase (FAK) localization in Focal Adhesion areas, as calculated from IRM signal intensities. **(A)** Gray scale intensities represent the distance in nm of cell membrane from the glass surface, as calculated from the IRM signal based on equations 5 and 6. Red areas, indicate anti-FAK-AlexaFluor[®]647 staining of Focal Adhesion Kinase. **(B)** Plot of intensities, along yellow line in **A** for anti-FAK-AlexaFluor[®]647 signal (red line) and for gray scale intensities/distances (black line). Membrane areas located at a distance smaller than 40 nm (blue line cutoff) are considered focal adhesion areas and are marked in gray.

4 Discussion

Cell migration is a process fundamental to life, but may also be one of the hallmarks of a pathological scenario such as is cancer [Dieterich et al. (2008)]. The latter has been associated with an increase in $K_v10.1$ expression [Agarwal et al. (2010)], which motivated us to further investigate how this particular ion channel may affect cell migration. Cell-cell and cell-surface adhesion dynamics impact cell physiology and alterations thereof may lead to transitions between different migration patterns, some of which enable cancer cell invasion and metastasis [Friedl and Wolf (2003); Le Bras et al. (2012); Rodriguez et al. (2012)]. The latter has been well-characterized in the human mesenchymal malignant HT-1080 fibrosarcoma cell line [Folpe (2014); Stout (1948); Rasheed et al. (1974)]. In addition, HT-1080 cells have been found to natively express the $K_v10.1$ ion channel, whose silencing by RNA interference reduces their proliferation [Weber et al. (2006)]. To better discern the role of $K_v10.1$ in cancer, we generated a stable HT-1080 cell line overexpressing a fluorescently tagged form of this ion channel, and compared it to an additional control HT-1080 cell line stably overexpressing the fluorophore only. The well-studied malignancy and invasiveness of HT-1080 cells, together with the implication of the $K_v10.1$ ion channel in tumorigenesis and cell migration, makes them an ideal model for the study of cell adhesion and migration.

We applied the *in vitro* scratch assay to study the migration characteristics of entire cell populations or those of individual cells. In this study we employed and further developed the capabilities of the traditional scratch assay to estimate and measure cell-cell and cell-surface adhesion, through the implementation of novel acquisition regimes and new analysis algorithms. We implemented time-lapse live imaging in multi-well dishes to assess in parallel the behavioral dynamics of the two HT-1080 cell lines in response to different treatments, targeting $K_v10.1$. Moreover, for the first time, live IRM recordings of non-migrating individual cells and migrating cell populations were acquired and analyzed with novel algorithms, which enabled us to study and measure the effect of $K_v10.1$ on the cell-surface adhesion ability and dynamics.

Accurate acquisition of multiple parameters, along with their automated large-scale analysis, are important steps towards the discovery of potentially statistically significant, treatment-induced changes in the dynamic behavior of the cells during scratch closure. Towards this goal, we have used a Leica SP5 CLSM, highlights of which include: 1. the 8KHz resonant scanner, 2. the fully motorized microscope stage capable of carrying multi-well dish within a temperature and CO_2 -controlled environment, 3. the low-noise and highly sensitive hybrid detectors, 4. the software-based autofocus and 5. the live data acquisition mode. Appropriate choice of image acquisition settings necessitated a methodological study of their effect on the migration behavior of HT-1080 cells.

4.1 Stimulation / acquisition setting-dependent cell behavior

We observed that the control HT-1080 cell behavior depended on the various time-lapse live image acquisition settings. Therefore, we were compelled to quantify the degree of phototoxicity of these acquisition settings by means of the scratch closure rate, where faster migration rate (up to a total loss of migration) corresponded to higher phototoxicity. The resulting findings enabled us to select the optimal settings for this type of hardware and cells, and may be used by others as an initial template towards the optimization of their live imaging model systems. Surprisingly, to the best of our knowledge, there is only one study [Spitler and Berns (2014)] that has reported the effect of a very limited set of image acquisition settings on the scratch assay outcome, but not in the context of live imaging and only by using a single dosage of red sifted wavelengths, as used for low-level laser therapy (LLLT). Our study is the first to report the effect of different laser types and scan settings on cell migration speed and fluorophore bleaching, during time lapse imaging of scratch closure.

4.1.1 Fluorochromes in higher energy states increase cell migration speed

Some of the acquisition settings we applied favor the scenario where a larger number of fluorochromes to remain longer in higher energy states like S_1 and T_1 , since some of the scanning durations of our settings match the $S_1 \rightarrow S_0$ and $T_1 \rightarrow T_0$ transition times (Figure 36). Interestingly, we observed in these cases an increase in scratch closure speed for all the energy density levels tested, or even an altogether cell migration stop when the delivered energy density exceeded an apparent tolerance limit of the cells (Table 7). This inhibition was accompanied by higher reduction of fluorescence yield over time and therefore indicated a higher photobleaching rate of the mVenus fluorochrome (Table 8). The white light laser (WL) delivers 0.25 ns lasting laser pulses that repeat every 12.5 ns. This excitation scenario was found to increase cell migration speed, by likely favoring fluorochromes to populate the higher S_1 energy state (Figure 4), with a low reduction of fluorescence intensity (column D in Table 8). Additionally, with the use of the conventional scanner set to a scanning speed of 0.4 kHz, we excited mVenus fluorochromes with a pixel dwell time of 5 μ s continuously with CW laser illumination, or repeatedly with the pulsed WL laser. This period of excitation, which is not only longer than the mVenus lifetime (~ 3 ns) [Sarkar et al. (2009)], but also exceeds the triplet state relaxation time ($T_1 \rightarrow T_0$ at the range of μ s), can favor the existence of fluorochromes at higher energy states, which are effective pathways for photobleaching (columns F and G in Table 8) and coincides with an increased migration rate. The increased cell migration speed with the use of single acquisition mode and the fast, resonant 8 kHz scanner, can be explained by the fact that per pixel the amount of energy delivered is almost 40 to 60 times more than

in the case of the multiple acquisition regime. In this scenario, many more fluorochromes are excited simultaneously and therefore increase the probability of intersystem crossing at high-energy triplet states, which are efficient photobleaching pathways (columns C, E, F and G in Table 8).

The interaction of higher energy state fluorochromes, or of the newly-generated free radicals with surrounding macromolecules responsible for cell-surface adhesion and cell motility, may be the reason of increased migration rate, after the usage of the above-mentioned stimulation / acquisition settings.

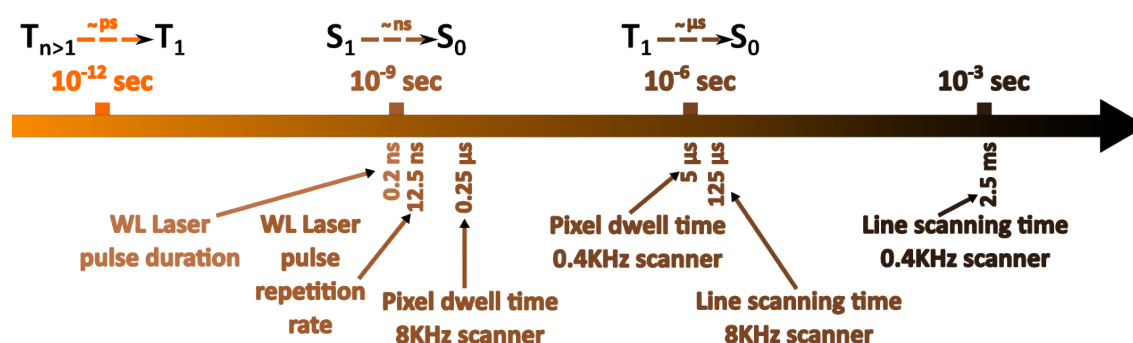


Figure 36 – Time scale bar relating relaxation durations of the various excited states to the various applied acquisition settings. mVenus fluorochrome lifetime is ~ 3 ns while its triplet state relaxation time is at the range of μ s.

4.1.2 Optimal settings for live imaging of cell migration

Live, time-lapse imaging of cell migration processes is essential in order to acquire the maximum amount of information regarding dynamic events. However, we must be aware that the process of cell migration is promoted by the laser excitation type and intensity as well as by the pixel dwell time, even with the minimum amount of energy required to generate enough recorded photons for subsequent analysis. In our study the scratch closure time of the same cell type, with the use of transmitted light during image acquisition, was at least 3 times slower than the case where the minimum energy levels used (data not shown). However, the knowledge of the stimulation settings effect on cells behavior is essential in order to choose the optimal hardware settings that give the best signal-to-noise ratio, while exerting the least effect on cell migration, so as to not overshadow the biological effect under investigation.

Based on our results and also considering previous studies concerning fluorescence yield optimization and photobleaching reduction [Donnert et al. (2007, 2009); Borlinghaus (2006)], we propose that for the laser-based monitoring of scratch assay dynamics that relies on the hardware we had at our disposal, a CW laser at a scanning speed of 8

kHz is most optimal. In order to increase the signal intensity, it proved helpful to use multiple line accumulations of emitted photons, where the hybrid detectors accumulated the signal faster than the background noise. The optimal way of delivering the energy, required for a more efficient fluorochrome excitation, is in small packages, in order to reduce the bleaching by the transition of excited fluorochromes to higher singlet or triplet states, which in turn can favor cell migration.

4.2 Cell adhesion

4.2.1 $K_v10.1$ reduces cell-surface adhesion

The dynamic nature of the cell adhesion process is more obvious during changes of cell state, like movement and surface adhesion [Webb et al. (2002)]. Specifically, migrating cells are morphologically and functionally polarized along the movement axis [Ridley et al. (2003); Schwab et al. (2007)], following a protrusive machinery based on cytoskeleton polarization. Depending on the type of protrusion, actin filaments can polymerize in a dendritic network within the lamellipodia, or in long parallel bundles in filopodia, having an essential role in migrating and invading cancer cells [Condeelis et al. (2001); Bergert et al. (2012); Zahm et al. (1997)].

It is also known that FAK co-localizes with integrins at FA sites and together with many additional signaling molecules (like small GTPases) interacts with the cytoskeleton [Parsons et al. (2010); Zhao and Guan (2011)]. There are studies concerning the dynamic transport of $K_v10.1$ via endosomal vesicles to the cell membrane, after interacting with Rabaptin-5 [Ninkovic et al. (2012)] and also about the transport of $K_v10.1$ to focal adhesion sites and its interaction with the cytoskeleton, with the cooperation of cortactin (CTTN) [Herrmann et al. (2012)]. Moreover, we have identified anterograde transport of $K_v10.1$ in filopodia, which are structures where focal adhesions may be formed.

In this study, no obvious cell-surface adhesion differences were noticeable between resting $K_v10.1$ and mVenus-overexpressing HT-1080 cells, as both cell types managed to form a confluent layer without noticeable cell-cell adhesion artifacts. However, using IRM and novel quantification methods, we were able to see that even non-migrating individual HT-1080- $K_v10.1$ -mVenus cells were dedicating a much smaller portion of their footprint to FA areas, than the control cells (Figure 32). Moreover, their adhesion dynamics were also different from control HT-1080-mVenus cells, which had closer contacts with the surface (mean distances of non-motile, protruding and retracting areas from the surface, in Figure 34C) and also higher rates of vertical distance changes over time (Figure 34D). These differences reveal a deficit in cell-surface adhesion in $K_v10.1$ overexpressing cells, which results in a more distant placement of the cell with respect to the glass surface, indicating a looser substrate adhesion. This deficit also results in the reduced ability

of $K_v10.1$ overexpressing cells to move their membrane in axial direction, compared with the control cells. The surface adhesion deficit of those cells is also accompanied by an increased spread rate, as indicated by the significantly higher protrusion and retraction rate (Figure 34B). This increased spread rate is likely rooted in the cell-surface adhesion deficit, since looser adhesion of the protruding and retracting parts of cell membrane favors the ability for faster lateral movements. Interestingly, the ability of $K_v10.1$ overexpressing cells to protrude and retract faster than control, is apparent even during the resting state, before the cells are tasked to migrate, and can explain also the increased migration rate in the context of scratch assay.

Impressively, mAb56 application improved cell-surface adhesion significantly for both mVenus and $K_v10.1$ overexpressing cells, by generating larger adhesive areas at the migration front and using larger portion of their footprint in FA areas. The improvement in lamellipodial-surface adhesion ability is significant even in control cells after mAb56 exposure, probably due to the presence and higher concentration of natively expressed $K_v10.1$ at the leading edge of migrating HT-1080-mVenus cells. This result could be promising for fibrosarcoma patient treatment with mAb56, where the adhesion ability of fibrosarcoma cells would be improved, thereby reducing the malignancy and invasiveness of this cancer. However, it seems that this improvement in the cell adhesion of control cells, after the application of mAb56, is not sufficient to cause a significant difference in their migration ability, with the exception at the maximum migration speed (U_{max}), which was reduced considerably. This can be explained by the low $K_v10.1$ expression levels in control cells and may be an additional indication that cell adhesion deficits, due to $K_v10.1$, precede and favor migration speed alterations. More importantly, the effect of $K_v10.1$ overexpression in cell-surface adhesion was rescued by the mAb56, since no significant difference was measured between not only the lamellipodial but also the full adhesive area of the mVenus and $K_v10.1$ -overexpressing cells. This rescue by the specific mAb56 blocker indicates also the specificity of the $K_v10.1$ effect in cell-surface adhesion deficit it generated in the first place. The proof of $K_v10.1$ participation in cell-surface adhesion inhibition is enhanced by the accompanied reduced migration ability of HT-1080- $K_v10.1$ cells upon mAb56 treatment, in accordance with the previously reported interrelation of adhesion and migration [Friedl and Wolf (2010)]. Interestingly, AST treatment had no effect in the lamellipodial cell-surface adhesion of control and $K_v10.1$ overexpressing cells.

The fact that the $K_v10.1$ ion channel is responsible for cell-surface adhesion deficits is supported by the localization of this channel to focal adhesion sites and at the lamellipodial area of some migrating cells. This localization was discovered using TIRF live imaging. The areas where F-actin fibers converge are sites where focal adhesions are located and that is where the localization of $K_v10.1$ ion channels was also shown in our

study. Moreover, with live imaging experiments we were able to show the anterograde transport of $K_v10.1$ ion channel in filopodia, which are important for cell-surface adhesion and directional migration [Parsons et al. (2010)]. These findings, together with the previously mentioned studies [Ninkovic et al. (2012); Herrmann et al. (2012)], leave no doubt that $K_v10.1$ is transported to focal adhesion sites, where it interacts with focal adhesion-associated proteins in a dynamic way, whenever there is a formation or turnover of cell-surface adhesion and affects cell-surface adhesion.

Both mAb56 and AST prevent K^+ ion permeation, and change the structural conformation of $K_v10.1$. More specifically, it is believed that after binding, both blockers force the $K_v10.1$ channel to remain in the open conformation. It is suspected that mAb56 and AST affect the $K_v10.1$ conformation in a different manner, since their binding sites are located in distant areas of the pore of the channel. The rescue of the effect caused by $K_v10.1$ overexpression on cell-surface adhesion ability, upon mAb56 application, but not after AST treatment, suggests that cell-surface adhesion is regulated by the non-conducting properties of $K_v10.1$, probably due to stereochemical interactions with molecules involved in these processes. This hypothesis is enhanced by the $K_v10.1$ localization results of this study and is in agreement with other studies, in which structural and functional interactions of potassium channels with molecules important for cell-surface adhesion (i.e. integrins), have been proposed [Arcangeli and Becchetti (2006); Bretscher (1996); Pardo and Stühmer (2013); Pillozzi and Arcangeli (2010)].

4.2.2 $K_v10.1$ reduces cell-cell adhesion in migrating cells

Initially, we were able to show the aggregation of $K_v10.1$ at the cell-cell interface of neighboring HeLa $K_v10.1$ overexpressing cells. However, $K_v10.1$ overexpression did not cause an apparent cell-cell adhesion defect in resting HT-1080 cells, since these cells managed to form a confluent layer before and after the end of scratch closure. Nevertheless, the dynamic observation of scratch closure, gave us the opportunity to investigate cell-cell adhesion dynamics and revealed adhesion deficits in $K_v10.1$ overexpressing cells, since during scratch closure greater intercellular space was generated in the HT-1080- $K_v10.1$ migrating population (Figure 30). These cell-cell adhesion deficits seem to be related with the accumulation of $K_v10.1$ over-expressed channels at cell-cell interfaces.

The blockage of $K_v10.1$ with mAb56 and AST showed a significant reduction of generated intercellular space, indicating a significant improvement in cell-cell adhesion. A non-statistically significant reduction of generated intercellular space was also observed after the application of mAb56 and AST in HT-1080-mVenus (control) cells, probably corresponding to the low levels of natively expressed $K_v10.1$, in HT-1080 cells.

More probably, direct or indirect $K_v10.1$ stereochemical interactions with macro-

molecules that mediate and regulate cell-cell adhesion may weaken cell contact forces causing the generation of larger intercellular spaces during cell migration. Such candidate macromolecules could be cadherins [Takeichi (1988)] and/or catenins [Nelson (2008); Ngok et al. (2013)] or ERM proteins (ezrin, radixin and moesin) [Ngok et al. (2013); Valderrama et al. (2012); Fehon et al. (2010)], which have been extensively implicated in regulation of cell-cell adhesion and cell migration, through Ca²⁺-dependent cell-cell adhesion mechanisms or through interactions with other transmembrane proteins with the cytoskeleton [Seeger-Nukpezah and Golemis (2012); Rahnama et al. (2006); Le Bras et al. (2012)]. It seems though, that the different conformation of K_v10.1 upon mAb56 or AST treatment, do not affect cell-cell adhesion in a different manner.

4.3 K_v10.1 overexpression enhances cell migration while reducing directionality

We have documented that the increase in cell migration speed coincides with K_v10.1 overexpression in individual cells that are part of a migrating cell population. In absolute agreement with previous studies [Hammadi et al. (2012)], we also showed the increased migration rate of K_v10.1 overexpressing cells during scratch closure. Additionally, K_v10.1 overexpression caused a different migration pattern of individual cells located at the scratch frontier. More specifically, HT-1080-K_v10.1 individual cells migrate with a greater maximum migration speed and adopt a more dispersed migration pattern with longer and less straight routes, while they retain their ability to migrate orthogonally with respect to the major scratch axis. This behavior could explain the invasiveness and metastatic ability [Dieterich et al. (2008); Becchetti and Arcangeli (2010); Pillozzi and Arcangeli (2010)] that has been reported [Pardo et al. (1999, 2005); Lin et al. (2011); Agarwal et al. (2010)] for cancers over-expressing K_v10.1.

The increased migration ability of K_v10.1 overexpressing cells seems to be due to cell-surface adhesion deficits, caused by accumulation of K_v10.1 ion channels at the cellular membrane. This increased migration ability was apparent even in stationary cells, where it manifested itself in high protrusion and retraction rates. Moreover, the blocking of K_v10.1 ion channels with mAb56 inhibited the migration rate of HT-1080-K_v10.1 cells in the context of scratch closure and also their individual maximum migration speed, while at the same time causing a less dispersed migration pattern with shorter and more straight routes. The same changes were observed upon AST treatment, where scratch closure rate and maximum individual migration speed of HT-1080-K_v10.1 cells decreased, resulting also in a less dispersed migration pattern with shorter routes. However, AST treatment did not rescue (but reduced) the effect of K_v10.1-overexpression on the route straightness. This result in combination with the non-affected lamellipodial-surface adhesion

after AST application, indicates a modulation of cell migration by cell-surface adhesion forces. This is consistent with what previous studies have reported concerning the effects of cell adhesion on cell-migration patterns [Friedl and Wolf (2010); Ridley et al. (2003); Miron-mendoza et al. (2008); Smith et al. (2007); Zhang et al. (2008)].

Like in previous studies [Friedl and Wolf (2003); Sanz-Moreno and Marshall (2009); Zhao and Guan (2011); Lauffenburger and Horwitz (1996)], these findings, show a dynamic relation between cell-cell adhesion, cell-surface adhesion and the migration pattern, which are essential for tumor progression and invasiveness [Rodriguez et al. (2012); Friedl and Gilmour (2009)]. With this study we propose that $K_v10.1$ overexpression regulates all the above-mentioned processes, not only in a migrating cell population, but also serves to prime resting, non-motile cells with adhesion deficits that allow for faster and more dispersed migration.

5 Conclusions and perspectives

Stimulation of the cells under study is required to study and better quantify the dynamic process of directional migration. We have confirmed that the scratch assay is suitable for this type of study, since it stimulates a cell population to migrate. In spite of the $K_v10.1$ overexpression, HT-1080 cells are also attracted to the initially introduced scratch, and finally close it, by forming a confluent cellular monolayer that is almost indistinguishable from their control counterparts. To better observe the dynamics of migrating cells in the context of the scratch assay, time-lapse live imaging is required. With our study, we revealed the effect of different stimulation / acquisition paradigms have on migration behavior and fluorescence yield of acquired cells. More importantly, this gave us the ability to adopt the least behavior-altering acquisition settings for all the subsequent scratch assay experiments.

Based on our results, we propose that $K_v10.1$ is responsible for cell-cell and cell-surface adhesion deficits. These deficits lead to a faster and more unconstrained migration of $K_v10.1$ overexpressing HT-1080 cells. Additionally, we propose a possible different involvement of $K_v10.1$ in the regulation of cell-cell and cell-surface adhesion, which to some degree can explain the different migration patterns after application of mAb56 or AST, which block $K_v10.1$ by different mechanisms.

This study sheds light on the invasiveness and the metastatic ability of $K_v10.1$ -expressing tumor cells, which is caused among others by the appearance of adhesion deficits. Especially in the case of fibrosarcoma, which is a malignant mesenchymal tumor with great invasive ability, the reduced surface adhesion enables a faster and more scattered migration ability, which is essential for the malignancy of this type of cancer. However,

we were able to improve cell-cell and cell-surface adhesion ability of HT-1080-mVenus (control) fibrosarcoma cells with the application of the mAb56. This approach resulted only in a significantly reduced maximum migration speed of fibrosarcoma cells, but seems promising for further implication of mAb56 for the treatment of K_v10.1-induced cancer.

We were further able to introduce new, semi-automated methods for scratch assay and time-lapse IRM analysis, which gave us the ability to quickly analyze a large amount of acquired data and to extract data regarding the scratch and the intercellular area size as well as measurements quantifying the dynamics of cell-substrate adhesion, with a minimum required user interaction. This also avoids any user-induced bias during analysis.

Our results are in absolute agreement with previous studies [Arcangeli and Becchetti (2006, 2010); Ridley et al. (2003); Pillozzi et al. (2011); Camacho et al. (2000)], concerning the localization and interaction of K_v10.1 with adhesion sites and cytoskeleton, as well as the effect of K_v10.1 on cell migration [Hammadi et al. (2012)]. However, for the first time the effect of K_v10.1 on cell-cell and cell-surface adhesion and migration was studied dynamically during and prior to scratch closure. Moreover, the effect of K_v10.1 on cell directionality was reported. These results may also be predictive for tumor cell behavior, especially concerning cell invasiveness and metastatic ability.

In the future, the role of K_v10.1 in cell proliferation during the scratch assay could also be investigated. The effect of K_v10.1 in cell proliferation has been reported before, but never during the scratch migration [Asher et al. (2011); Gómez-Varela et al. (2007); García-Quiroz and Camacho (2011); Pardo et al. (1999)]. The dynamic monitoring of cell proliferation though, during cell migration, can provide important data about how cell proliferation affects scratch closure and whether K_v10.1 may alter migration patterns through cell cycle manipulation. More specific, EdU can be used, together with Hoechst, in order to calculate the number and duration of cell division, even in different zones around the scratch, and to reveal how this proliferation ability is changing after blocking of K_v10.1. As part of the same experiment, filamentous actin content may be quantified through phalloidin staining, thereby quantifying any effect K_v10.1 overexpression may have on cytoskeleton dynamics in a migrating population.

Also, as the cellular cytoskeleton plays a major role in cell migration, a potential interplay between K_v10.1 and molecules controlling cytoskeleton dynamics can be investigated. Possible key players for this interactions could be PIP2, calmodulin or members of the family of small Rho GTPases, e.g., RhoA, Rac1 and Cdc42, that promote the formation of specific cellular morphologies and play a major role in cell migration [Meng et al. (2004); Nelson (2008); Petrie et al. (2009); Arcangeli and Becchetti (2006)]. The study of these interactions can help us reveal the molecular basis of the relation of K_v10.1 with cell-cell, cell-surface adhesion and migration.

In vivo experiments with injection of HT-1080-mVenus and HT-1080-K_v10.1-mVenus

cells in mice, could also give important insights into the effect of $K_v10.1$ in cell migration, invasion and metastasis. A subsequent application of mAb56 in these mice could additionally reveal the importance of mAb56 as an anti-cancer drug, for the case that it will result in alteration of the behavior of HT-1080- $K_v10.1$ overexpressing cells.

The overall aim of such a project would be the investigation of the rules governing the interplay between the $K_v10.1$ ion channel appearance and cell adhesion and motility. The understanding of these mechanisms may help explaining to some degree the role of cell motility and adhesion in cancer. The observation of the different patterns existing in movement and adhesion of cancer cells expressing $K_v10.1$ will help us perceive the role of this ion channel in those two important cell functions.

The outcome of these proposed studies may provide optimal tools for the study of tumor physiology, pattern of metastasis, and for monitoring tumor progression as well as the outcome and the effects of interventions on cancer.

6 Appendix / Algorithms

6.1 List of primary antibodies

| Label | Clonality Host | Target | Experiment | Dilution | Provider Reference |
|--------|-------------------|--------------------------------|--------------------|------------|--------------------------------------|
| 56 | Monoclonal Mouse | K _v 10.1 pore loop | Scratch Assay, IRM | 0.01 µg/ml | L.A. Pardo; Hemmerlein et al. (2006) |
| 1218 | Monoclonal Mouse | GFP / mVenus | IP | 2 µg/µl | Abcam® |
| 9391 | Polyclonal Rabbit | K _v 10.1 C-terminus | WB | 1:1500 | L.A. Pardo; Napp et al. (2005) |
| 6556 | Polyclonal Mouse | GFP / mVenus | WB | 1:1000 | Abcam® |
| 24610 | Monoclonal Mouse | acetylated- α -tubulin | IHC | 1:2000 | Abcam® |
| 610087 | Monoclonal Mouse | FAK | IHC | 1:250 | BD Bioscience |

Table 9 – List of used primary antibodies in different assays in this study

6.2 Adhesion dynamics algorithm (“ProRet”)

This algorithm is implemented in FIJI macros, combining in a novel way already existing plugins and methods. The following paragraphs is a summary of the main components of the software.

Software input and output

The software can accept a large variety of different file types, since it uses the Bio-Formats plugin importer. When multi stack container files are processed, the software gives the opportunity to select one or more image stacks that can be processed with the same parameters (A1 in Figure 37). The user can also define the channel (in case of multiple channel image stacks) that corresponds to the IRM signal (A2 in Figure 37), and also select a specific range of time frames for analysis (A3 in Figure 37).

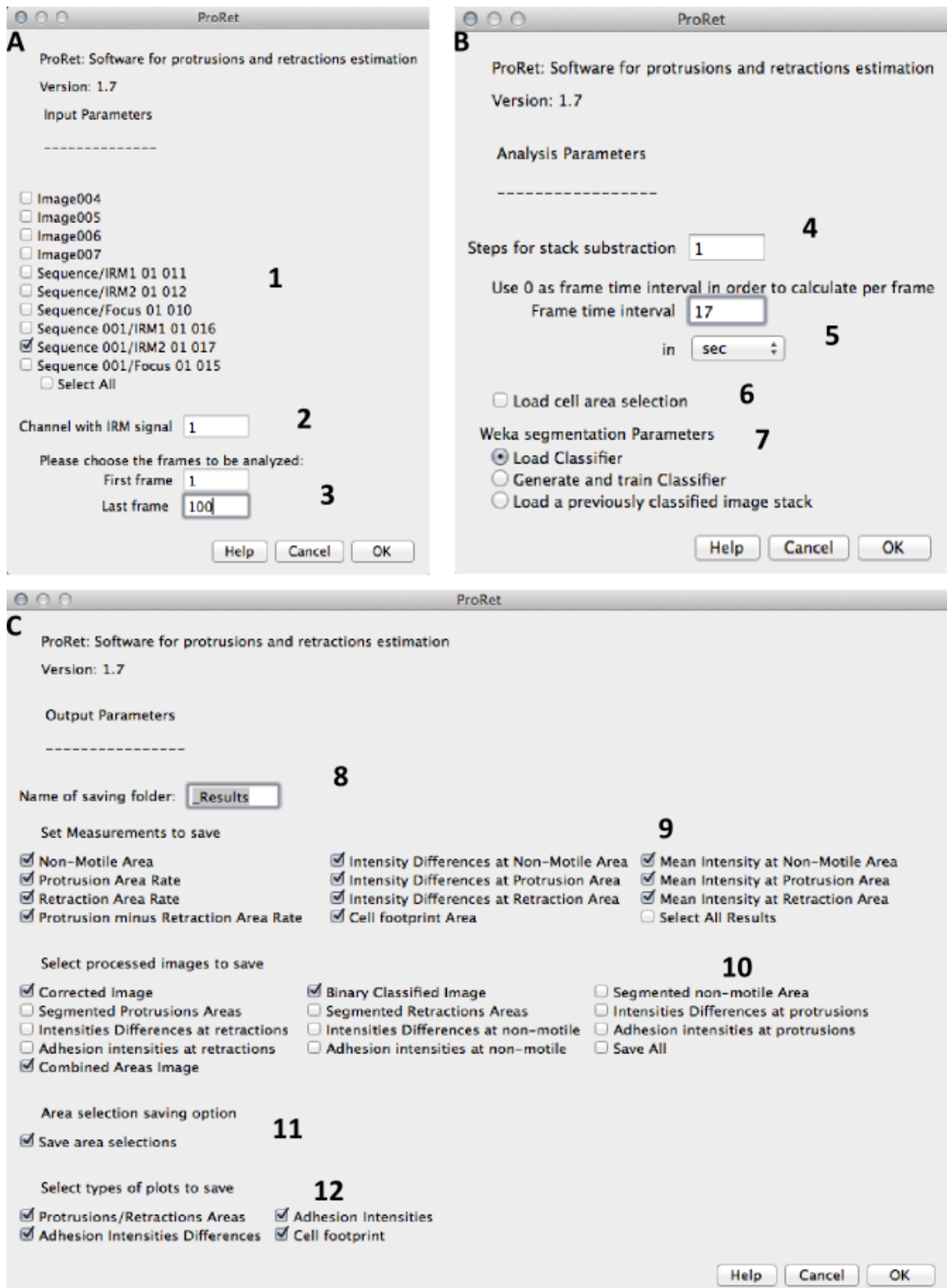


Figure 37 – Dialogue menu of “ProRet” software. The user can select the input file (**A₁**) as well as the channel (**A₂**) and frames (**A₃**) of interest. In **B** the user can insert the analysis parameters (subtraction steps 4, time frame interval 5, area selection 6 and Weka segmentation parameters 7). Finally, in **C** the user can choose the output parameters (name of output folder 8, type of measurements 9, which images will be saved 10, if area selection will be saved 11 and which types of plots will be saved 12).

The user then must enter the subtraction step that will be used for defining the protruding, the retracting and the non-motile areas of cells and also the vertical membrane movement rate at these regions (A4 in Figure 37). Moreover, the user can define the frame time interval used for the acquisition (A5 in Figure 37). This value will be used for the rate calculations giving the results as areas per sec, per min, per hrs or just per frame, depending on user input. All the measurements will take place in an area defined by the user. The software allows to load a previously selected area (A6 in Figure 37).

"ProRet" uses the Weka Trainable Segmentation plugin in order to classify and define the cell regions from the treated IRM image. The user has three options for this segmentation (A7 in Figure 37). An already trained classifier of the Weka plugin can be loaded in case the training has happened before, or the user can generate and train a new classifier (highly recommended in the case of an analysis taking place for the first time in a new data set). Additionally the user can load a previously classified version of the under analysis image. It is assumed at this step that the user will load a segmented version of the image time-stack that is selected for analysis.

The output files of each run are saved in a separate folder named by the user under the parent directory of the input file (C8 in Figure 37). For each selected image (A1 in Figure 37), a separate folder with the name of each time stack is generated under the specified output folder. The selected types of results (C9 in Figure 37) are saved in a text file with tab-separated columns. Additionally the processed images at the different stages of the program (images 3, 4, 7a, 7b, 7c, 8a, 8b, 8c, 9a, 9b, 9c in Figure 38) can also be saved, for further use or for evaluation of the software behavior by the user, based on the user selections (C10 in Figure 37). The area selection (loaded or selected by the user) that was used for the measurements can also be saved (C11 in Figure 37). The calculated results are plotted automatically by the software and can be also saved as .tif files giving the opportunity for a fast overview of the results for each analyzed image (C12 in Figure 37).

Image pre-treatment

The defined range of time frames of the input image is converted to 32 bit and each frame is normalized with a highly blurred (Gaussian blur 20 pixel radius) version of the stack, in order to remove noise derived from uneven illumination in each frame. Similar approaches for noise removal have also been implemented by others [Limozin and Sen Gupta (2007)] in the case of IRM data pre-treatment. The filtered stack is then registered using the StackReg plugin [Thévenaz et al. (1998)] in order to remove drifting from frame to frame that could affect the measurements. After this step, the software determines the minimum and maximum intensity value among all time frames of the stack and converts each pixel intensity value into distance from glass surface (in nm) using equation 6 as

described in 2.6.2.

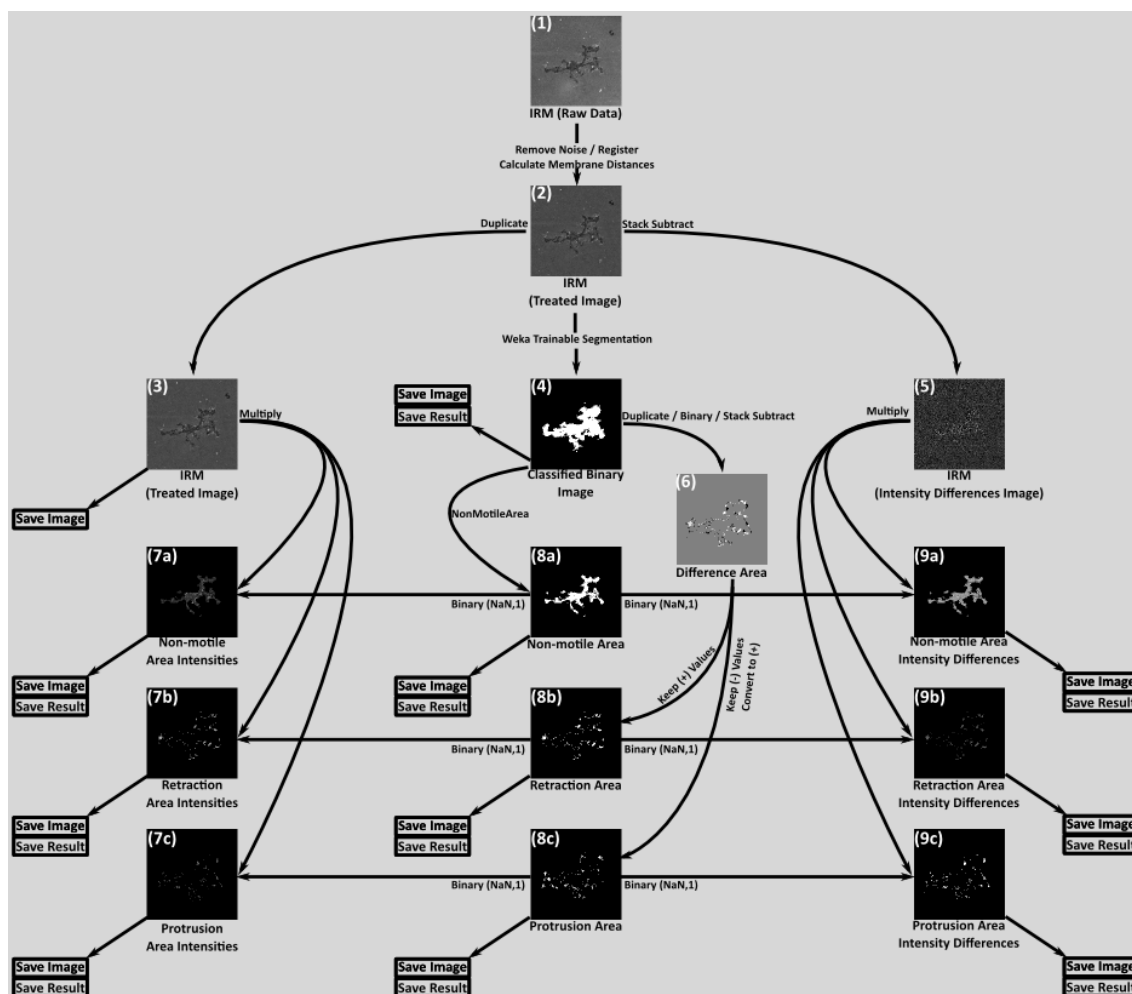


Figure 38 – Adhesion dynamics analysis workflow of the IRM signal of a cell. From the loaded stack (1) the noise is removed and the stack is registered (2 and 3). One version of this treated image is then segmented (with the Weka Trainable Segmentation plugin) and the classified binary image (4) is used to measure cell footprint over time and to define and measure the non-motile area (8a) and after frame subtraction the retracting (8b) and the protruding areas (8c) over time. These binary defined areas are then used in combination with the IRM treated image (3) in order to measure the mean adhesion intensity in non-motile area (7a), in retracting areas (7b) and in protruding areas (7c) for every time point. Moreover, using the subtracted adhesion intensities (5) in combination with the binary defined areas, the adhesion intensity rate (differences) is calculated for the respective regions (non-motile area 9a, retracting areas 9b and protruding areas 9c).

This treated multi-frame image contains pixel values that correspond to the calculated distance of each area from the substrate. This image (2 in Figure 38) will be used to measure then mean membrane distances, mean vertical membrane movement, and cell areas after segmentation.

Segmentation

The segmentation of the image is needed in order to define and distinguish cell regions from background. This can be difficult using a simple threshold, especially in the case of IRM images. For this reason, in "ProRet" we have used the Trainable Weka Segmentation plugin⁴ that is included at the latest ImageJ/Fiji distributions. With this plugin the user can train chosen classifiers based on the set of images that will be analyzed. These classifiers can also be loaded, shortening the analysis time. Additionally the user has the opportunity to load previously classified binary time-stack images (that corresponds to the same image that is under process).

Defining and measuring areas

After the classification, this binary classified image (4 in Figure 38) is used to define the cell footprint area, the non-motile cell area, as well as the protruding and retracting areas as following:

Cell footprint area: Since the binary classified image was generated based on the segmentation of the IRM signal, the measurement of the user-defined area of this image, gives the cell area footprint. After the measurement of this area per time frame, the area footprint can be plotted over time.

Non-motile area: The binary classified image with pixel values 0 for background and 255 for cell area is used in order to generate a projection of the average pixel values of the time stack image. Areas of the binary image that have always a value of 255 (non motile regions) are represented in the projection image as areas with pixel values of 255. All the pixels with average value less than 255 represent the motile over time regions of a cell. With a simple thresholding we keep from this projection only the non-motile regions (values 255), generating finally a binary (0,1) image mask that after multiplication with the classified image, a binary time stack image with the non-motile area of the cell (8a in Figure 38) is generated.

Protruding and retracting areas: At the binary classified image (4 in Figure 38) the StackSubtract32 plugin is applied generating a new time stack image where each frame contains the protruding (negative values) and retracting areas (positive values) of the cell (6 in Figure 38). Keeping with a threshold only the positive values or only the negative ones (converting them into their absolute value) we generate two binary (0, 255) time

⁴http://fiji.sc/Trainable_Weka_Segmentation

stacks, one containing only the retracting and the second only the protruding areas (8b and 8c respectively in Figure 38).

The above-defined areas were then measured for each time frame calculating the protruding and retracting area rate (area per time over time).

Measuring membrane proximity at the defined regions: Having the IRM treated image with pixel values that correspond to membrane distances from the glass surface (3 of Figure 38), after multiplication with the respective binary images defining the non-motile, the retracting and protruding regions, we generated images with height values at the defined areas (7a, 7b, and 7c respectively in Figure 38). Measuring the mean height for each time frame for each image, we calculated the mean membrane proximity for the respective areas over time.

Measuring membrane proximity rate at the defined regions: From the IRM treated image with height values (2 in Figure 38), using the StackSubtract32 plugin, a new time-stack image with height differences was generated (5 in Figure 38). Each pixel value at this image represents the membrane proximity change for the defined step of subtraction. Multiplying this image with the binary images with the defined regions (non-motile, retracting and protruding), new images with height differences only at the defined regions were generated (9a, 9b, and 9c respectively in Figure 38). Measuring the mean pixel value for each frame of these images, we calculated the mean membrane proximity rate over time.

Bibliography

- Abercrombie, M. and G. a. Dunn: 1975, 'Adhesions of fibroblasts to substratum during contact inhibition observed by interference reflection microscopy.'. *Experimental cell research* **92**(1), 57–62. (page 12).
- Abercrombie, M., J. E. Heaysman, and S. M. Pegrum: 1971, 'The locomotion of fibroblasts in culture. IV. Electron microscopy of the leading lamella.'. *Experimental cell research* **67**, 359–367. (page 8).
- Agarwal, R., F. Griesinger, W. Stühmer, L. A. Pardo, and J. R. Agarwal: 2010, 'The potassium channel Ether {à} go-go is a novel prognostic factor with functional relevance in acute myeloid leukemia'. *Mol Cancer* **9**(1), 18. (pages 6, 66, and 72).
- Alberto, M. E., N. Russo, A. Grand, and A. Galano: 2013, 'A physicochemical examination of the free radical scavenging activity of Trolox: mechanism, kinetics and influence of the environment.'. *Physical chemistry chemical physics : PCCP* **15**(13), 4642–50. (page 14).
- Albrecht-Buehler, G.: 1977, 'Phagokinetic tracks of 3T3 cells: parallels between the orientation of track segments and of cellular structures which contain actin or tubulin.'. *Cell* **12**(2), 333–9. (page 11).
- Amaral, A. C., N. A. Parizotto, and T. F. Salvini: 2001, 'Dose-dependency of Low-energy HeNe Laser Effect in Regeneration of Skeletal Muscle in Mice'. *Lasers in medical science* **16**, 44–51. (page 13).
- Anbar, M. and E. Hart: 1964, 'The Reactivity of Aromatic Compounds toward Hydrated Electrons'. *J. Am. Chem. Soc* **4090**(1962), 5–9. (page 13).
- Arcangeli, A. and A. Becchetti: 2006, 'Complex functional interaction between integrin receptors and ion channels.'. *Trends in cell biology* **16**(12), 631–9. (pages 12, 71, 74, and 74).
- Arcangeli, A. and A. Becchetti: 2010, 'Integrin structure and functional relation with ion channels.'. *Advances in experimental medicine and biology* **674**, 1–7. (pages 11, 12, and 74).
- Asher, V., R. Khan, A. Warren, R. Shaw, G. V. Schalkwyk, A. Bali, and H. M. Sowter: 2010a, 'The Eag potassium channel as a new prognostic marker in ovarian cancer.'. *Diagnostic pathology* **5**(1), 78. (page 6).

- Asher, V., H. Sowter, R. Shaw, A. Bali, and R. Khan: 2010b, 'Eag and HERG potassium channels as novel therapeutic targets in cancer.'. *World journal of surgical oncology* **8**(1), 113. (page 7).
- Asher, V., A. Warren, R. Shaw, H. Sowter, A. Bali, and R. Khan: 2011, 'The role of Eag and HERG channels in cell proliferation and apoptotic cell death in SK-OV-3 ovarian cancer cell line.'. *Cancer cell international* **11**(1), 6. (pages 6 and 74).
- Axelrod, D.: 1981, 'Cell-substrate contacts illuminated by total internal reflection fluorescence'. *Journal of Cell Biology* **89**(9), 141–145. (page 19).
- Babich, H., E. J. Liebling, R. F. Burger, H. L. Zuckerbraun, and a. G. Schuck: 2009, 'Choice of DMEM, formulated with or without pyruvate, plays an important role in assessing the in vitro cytotoxicity of oxidants and prooxidant nutraceuticals.'. *In vitro cellular & developmental biology. Animal* **45**(5-6), 226–33. (page 10).
- Bacakova, L., E. Filova, M. Parizek, T. Ruml, and V. Svorcik: 2011, 'Modulation of cell adhesion, proliferation and differentiation on materials designed for body implants'. *Biotechnology Advances* **29**(6), 739–767. (page 12).
- Basten, S. G. and R. H. Giles: 2013, 'Functional aspects of primary cilia in signaling, cell cycle and tumorigenesis.'. *Cilia* **2**(1), 6. (page 11 and 11).
- Bauer, C. K. and J. R. Schwarz: 2001, 'Physiology of EAG K⁺ channels.'. *The Journal of membrane biology* **182**, 1–15. (pages 1, 2, 4, and 6).
- Becchetti, A. and A. Arcangeli: 2010, 'Integrins and ion channels in cell migration: implications for neuronal development, wound healing and metastatic spread.'. In: *Advances in experimental medicine and biology*, Vol. 674. Landes Bioscience and Springer Science, pp. 107–23. (pages 8, 10, 12, 14, and 72).
- Bergert, M., S. D. Chandradoss, R. a. Desai, and E. Paluch: 2012, 'Cell mechanics control rapid transitions between blebs and lamellipodia during migration.'. *Proceedings of the National Academy of Sciences of the United States of America* **109**(36), 14434–9. (pages 9 and 69).
- Bogdanov, A. M., E. a. Bogdanova, D. M. Chudakov, T. V. Gorodnicheva, S. Lukyanov, and K. a. Lukyanov: 2009, 'Cell culture medium affects GFP photostability: a solution.'. *Nature methods* **6**(12), 859–60. (page 14).
- Bogdanov, A. M., E. I. Kudryavtseva, and K. a. Lukyanov: 2012, 'Anti-fading media for live cell GFP imaging.'. *PloS one* **7**(12), e53004. (page 14).

- Borlinghaus, R. T.: 2006, 'MRT Letter : High Speed Scanning Has the Potential to Increase Fluorescence Yield and to Reduce Photobleaching'. *Microscopy research and technique* **69**(July), 689–692. (pages 32 and 68).
- Bretscher, M. S.: 1996, 'Getting membrane flow and the cytoskeleton to cooperate in moving cells.'. *Cell* **87**(4), 601–6. (page 71).
- Bruggemann, A., L. A. Pardo, W. Stühmer, and O. Pongs: 1993, 'Ether-à-go-go encodes a voltage-gated channel permeable to K⁺ and Ca²⁺ and modulated by cAMP'. *Nature* **365**(6445), 445–448. (pages 2 and 5).
- Bruggemann, A., W. Stühmer, and L. a. Pardo: 1997, 'Mitosis-promoting factor-mediated suppression of a cloned delayed rectifier potassium channel expressed in *Xenopus* oocytes.'. *Proceedings of the National Academy of Sciences of the United States of America* **94**(2), 537–42. (page 5).
- Burnette, D. T., S. Manley, P. Sengupta, R. Sougrat, M. W. Davidson, B. Kachar, and J. Lippincott-Schwartz: 2011, 'A role for actin arcs in the leading-edge advance of migrating cells.'. *Nature cell biology* **13**(4), 371–81. (page 8).
- Cabodi, S., V. Morello, A. Masi, R. Cicchi, C. Broggio, P. Distefano, E. Brunelli, L. Silengo, F. S. Pavone, A. Arcangeli, E. Turco, G. Tarone, L. Moro, and P. Defilippi: 2009, 'Convergence of integrins and EGF receptor signaling via PI3K/Akt/FoxO pathway in early gene Egr-1 expression.'. *Journal of cellular physiology* **218**(2), 294–303. (page 14).
- Camacho, J., A. Sánchez, W. Stühmer, and L. A. Pardo: 2000, 'Cytoskeletal interactions determine the electrophysiological properties of human EAG potassium channels'. *Pflugers Arch* **441**(2-3), 167–174. (pages 14 and 74).
- Chalkiadaki, G., D. Nikitovic, A. Berdiaki, M. Sifaki, K. Krasagakis, P. Katonis, N. K. Karamanos, and G. N. Tzanakakis: 2009, 'Fibroblast growth factor-2 modulates melanoma adhesion and migration through a syndecan-4-dependent mechanism.'. *The international journal of biochemistry & cell biology* **41**(6), 1323–31. (pages 12 and 14).
- Chen, C.-H., H.-S. Hung, and S.-H. Hsu: 2008, 'Low-energy laser irradiation increases endothelial cell proliferation, migration, and eNOS gene expression possibly via PI3K signal pathway.'. *Lasers in surgery and medicine* **40**(1), 46–54. (page 13).
- Chen, Y., A. Sánchez, M. E. Rubio, T. Kohl, L. A. Pardo, and W. Stühmer: 2011, 'Functional K(v)10.1 channels localize to the inner nuclear membrane.'. *PloS one* **6**(5), e19257. (page 7 and 7).

- Cherubini, A., G. Hofmann, S. Pillozzi, L. Guasti, O. Crociani, E. Cilia, P. D. Stefano, S. Degani, M. Balzi, M. Olivotto, E. Wanke, A. Becchetti, P. Defilippi, R. Wymore, and A. Arcangeli: 2005, 'Human ether-a-go-go-related Gene 1 Channels Are Physically Linked to β 1 Integrins and Modulate Adhesion-dependent Signaling'. *Molecular Biology of the Cell* **16**(June), 2972–2983. (page 11).
- Choi, C. K., C. H. Margraves, A. E. English, and K. D. Kihm: 2008, 'Multicontrast microscopy technique to dynamically fingerprint live-cell focal contacts during exposure and replacement of a cytotoxic medium.'. *Journal of biomedical optics* **13**(5), 054069. (pages 17, 17, and 18).
- Christensen, S. T., S. F. Pedersen, P. Satir, I. R. Veland, and L. Schneider: 2008, 'The primary cilium coordinates signaling pathways in cell cycle control and migration during development and tissue repair'. In: *Current Topics in Developmental Biology*. Elsevier Inc., Chapt. 10, pp. 261–301. (pages 10 and 11).
- Chung, H., T. Dai, S. Sharma, Y. Huang, J. Carroll, and M. Hamblin: 2012, 'The Nuts and Bolts of Low-level Laser (Light) Therapy'. *Ann. Biomed Eng.* **40**(2), 516–533. (page 13).
- Clough, D. and R. Buenger: 1995, 'Protection by pyruvate against inhibition of Na⁺, K⁺-ATPase by free radical generating system containing t-Butylhydroperoxide'. *Life Sciences* **57**(10), 931–943. (page 13).
- Cole, K. S. and J. W. Moore: 1960, 'Potassium ion current in the squid giant axon: dynamic characteristic.'. *Biophysical journal* **1**, 1–14. (page 5).
- Condeelis, J. S., J. B. Wyckoff, M. Bailly, R. Pestell, D. Lawrence, J. Backer, and J. E. Segall: 2001, 'Lamellipodia in invasion.'. *Seminars in cancer biology* **11**(2), 119–28. (pages 15 and 69).
- Coomber, B. L. and a. I. Gotlieb: 1990, 'In vitro endothelial wound repair. Interaction of cell migration and proliferation'. *Arteriosclerosis, Thrombosis, and Vascular Biology* **10**(2), 215–222. (page 14).
- Cory, G.: 2011, 'Scratch-Wound Assay'. In: C. M. Wells and M. Parsons (eds.): *Methods in Molecular Biology*, Vol. 769 of *Methods in Molecular Biology*. Totowa, NJ: Humana Press, Chapt. 2, pp. 25–30. (page 15 and 15).
- Cunha, L. C., E. Del Bel, L. a. Pardo, W. Stühmer, R. Titze-De-Almeida, and I. Journal: 2013, 'RNA Interference with EAG1 Enhances Interferon Gamma Injury to Glioma Cells In Vitro'. *Anticancer Research* **33**(3), 865–870. (page 6).

- Curtis, A. S. G.: 1964, 'A Study by Interference Reflection Microscopy'. *Journal of Cell Biology* **20**(1), 199–215. (page 15).
- Dadras, S., E. Mohajerani, F. Eftekhari, and M. Hosseini: 2006, 'Different photoresponses of *Staphylococcus aureus* and *Pseudomonas aeruginosa* to 514, 532, and 633 nm low level lasers in vitro.'. *Current microbiology* **53**(4), 282–6. (page 13).
- Dailey, M., E. Manders, D. Soll, and M. Terasaki: 2006, 'Confocal Microscopy of Live Cells'. In: *Handbook of Biological Confocal Microscopy*. Pawley, James (Ed.), 3rd edition, Chapt. 19. (page 13 and 13).
- Dailey, M. E., G. S. Marrs, and D. Kurpius: 2011, 'Maintaining Live Cells and Tissue Slices in the Imaging Setup'. *Cold Spring Harbor Protocols* **2011**(4), 372–379. (page 13).
- D'Amico, M., L. Gasparoli, and A. Arcangeli: 2013, 'Potassium channels: novel emerging biomarkers and targets for therapy in cancer.'. *Recent patents on anti-cancer drug discovery* **8**(1), 53–65. (pages 6 and 7).
- Damsky, G. H., K. A. Knudsen, and G. A. Buck: 1984, 'Integral Membrane Glycoproteins in Cell-Cell and Cell-Substratum Adhesion'. In: *The Biology of Glycoproteins*. Plenum Press. (page 11).
- Davis, E. M. and J. P. Trinkaus: 1981, 'Significance of cell-to cell contacts for the directional movement of neural crest cells within a hydrated collagen lattice.'. *Journal of embryology and experimental morphology* **63**, 29–51. (page 9).
- de Guadalupe Chávez-López, M., J. I. Pérez-Carreón, V. Zuñiga García, J. Díaz-Chávez, L. a. Herrera, C. H. Caro-Sánchez, I. Acuña Macías, P. Gariglio, E. Hernández-Gallegos, A. J. Chiliquinga, and J. Camacho: 2015, 'Astemizole-based anticancer therapy for hepatocellular carcinoma (HCC), and Eag1 channels as potential early-stage markers of HCC'. *Tumor Biology*. (pages 6, 6, and 7).
- Devreotes, P. and C. Janetopoulos: 2003, 'Eukaryotic chemotaxis: distinctions between directional sensing and polarization.'. *The Journal of biological chemistry* **278**(23), 20445–8. (page 15 and 15).
- Dieterich, P., R. Klages, R. Preuss, and A. Schwab: 2008, 'Anomalous dynamics of cell migration.'. *Proceedings of the National Academy of Sciences of the United States of America* **105**(2), 459–63. (pages 38, 66, and 72).

- Ding, X., H. Luo, X. Jin, J. Yan, and Y. Ai: 2007a, 'Aberrant expression of Eag1 potassium channels in gastric cancer patients and cell lines'. *Med Oncol* pp. 345–350. (page 6).
- Ding, X., J. Yan, P. An, P. Lü, and H. Luo: 2007b, 'Aberrant expression of ether à go-go potassium channel in colorectal cancer patients and cell lines'. *World Journal of Gastroenterology* **13**(8), 1257–1261. (page 6).
- Doherty, G. J. and H. T. McMahon: 2008, 'Mediation, modulation, and consequences of membrane-cytoskeleton interactions.'. *Annual review of biophysics* **37**, 65–95. (page 29).
- Donnert, G., C. Eggeling, and S. W. Hell: 2007, 'Major signal increase in fluorescence microscopy through dark-state relaxation'. *Nature methods* **4**(1), 81–86. (pages 14, 32, and 68).
- Donnert, G., C. Eggeling, and S. W. Hell: 2009, 'Triplet-relaxation microscopy with bunched pulsed excitation.'. *Photochemical & photobiological sciences : Official journal of the European Photochemistry Association and the European Society for Photobiology* **8**(4), 481–5. (pages 14 and 68).
- Downie, B. R., A. Sánchez, H. Knötgen, C. Contreras-Jurado, M. Gymnopoulos, C. Weber, W. Stühmer, and L. a. Pardo: 2008, 'Eag1 expression interferes with hypoxia homeostasis and induces angiogenesis in tumors.'. *The Journal of biological chemistry* **283**(52), 36234–40. (pages 6, 7, and 7).
- Doyle, D. a., J. Morais Cabral, R. a. Pfuetzner, a. Kuo, J. M. Gulbis, S. L. Cohen, B. T. Chait, and R. MacKinnon: 1998, 'The structure of the potassium channel: molecular basis of K⁺ conduction and selectivity.'. *Science (New York, N.Y.)* **280**(1998), 69–77. (page 1).
- Eggeling, C., J. Widengren, R. Rigler, and C. a. Seidel: 1998, 'Photobleaching of Fluorescent Dyes under Conditions Used for Single-Molecule Detection: Evidence of Two-Step Photolysis'. *Analytical chemistry* **70**(13), 2651–9. (page 13).
- Ejiri, K., A. Aoki, Y. Yamaguchi, M. Ohshima, and Y. Izumi: 2013, 'High-frequency low-level diode laser irradiation promotes proliferation and migration of primary cultured human gingival epithelial cells.'. *Lasers in medical science*. (page 13 and 13).
- Elbashir, S. M., J. Harborth, W. Lendeckel, A. Yalcin, K. Weber, and T. Tuschl: 2001, 'Duplexes of 21-nucleotide RNAs mediate RNA interference in cultured mammalian cells'. *Nature* **411**(6836), 494–498. (page 20).

- Fehon, R., A. McClatchey, and A. Bretscher: 2010, 'Organizing the Cell Cortex : The role of ERM proteins'. *Nat Rev Mol Cell Biol* **11**(4), 276–287. (page 72).
- Folpe, A. L.: 2014, 'Fibrosarcoma: a review and update.'. *Histopathology* **64**(1), 12–25. (page 66).
- Friedl, P., S. Borgmann, and E. B. Bröcker: 2001, 'Amoeboid leukocyte crawling through extracellular matrix: lessons from the Dictyostelium paradigm of cell movement.'. *Journal of leukocyte biology* **70**(October), 491–509. (page 9).
- Friedl, P. and D. Gilmour: 2009, 'Collective cell migration in morphogenesis, regeneration and cancer.'. *Nature reviews. Molecular cell biology* **10**(7), 445–57. (pages 9, 9, and 73).
- Friedl, P. and K. Wolf: 2003, 'Tumour-cell invasion and migration: diversity and escape mechanisms.'. *Nature reviews. Cancer* **3**(5), 362–74. (pages 12, 66, and 73).
- Friedl, P. and K. Wolf: 2010, 'Plasticity of cell migration: a multiscale tuning model.'. *The Journal of Cell biology* **188**(1), 11–9. (pages 9, 9, 10, 12, 12, 70, and 73).
- Friedl, P., K. S. Zänker, and E. B. Bröcker: 1998, 'Cell migration strategies in 3-D extracellular matrix: Differences in morphology, cell matrix interactions, and integrin function'. *Microscopy Research and Technique* **43**(96), 369–378. (page 9).
- Frigault, M. M., J. Lacoste, J. L. Swift, and C. M. Brown: 2009, 'Live-cell microscopy - tips and tools.'. *Journal of cell science* **122**(Pt 6), 753–67. (page 13).
- Ganguly, A., H. Yang, R. Sharma, K. D. Patel, and F. Cabral: 2012, 'The Role of Microtubules and Their Dynamics in Cell Migration.'. *The Journal of biological chemistry* **287**(52), 43359–43369. (pages 8 and 14).
- Gangur, V., N. P. Birmingham, and S. Thanavorakul: 2002, 'Chemokines in health and disease.'. *Veterinary immunology and immunopathology* **86**(3-4), 127–36. (page 15).
- García-Ferreiro, R. E., D. Kerschensteiner, F. Major, F. Monje, W. Stühmer, and L. A. Pardo: 2004, 'Mechanism of block of hEag1 K⁺ channels by imipramine and astemizole.'. *The Journal of general physiology* **124**(4), 301–17. (pages 5, 5, and 7).
- García-Quiroz, J. and J. Camacho: 2011, 'Astemizole: an old anti-histamine as a new promising anti-cancer drug.'. *Anti-cancer agents in medicinal chemistry* **11**(3), 307–14. (pages 5 and 74).

- García-Quiroz, J., R. García-Becerra, D. Barrera, N. Santos, E. Avila, D. Ordaz-Rosado, M. Rivas-Suárez, A. Halhali, P. Rodríguez, A. Gamboa-Domínguez, H. Medina-Franco, J. Camacho, F. Larrea, and L. Díaz: 2012, 'Astemizole Synergizes Calcitriol Antiproliferative Activity by Inhibiting CYP24A1 and Upregulating VDR: A Novel Approach for Breast Cancer Therapy.'. *PloS one* **7**(9), e45063. (page 7).
- García-Quiroz, J., R. García-Becerra, N. Santos-Martínez, D. Barrera, D. Ordaz-Rosado, E. Avila, A. Halhali, O. Villanueva, M. a. J. Ibarra-Sánchez, J. Esparza-López, A. Gamboa-Domínguez, J. Camacho, F. Larrea, and L. Díaz: 2014, 'In vivo dual targeting of the oncogenic Ether-a-go-go-1 potassium channel by calcitriol and astemizole results in enhanced antineoplastic effects in breast tumors.'. *BMC cancer* **14**(1), 745. (page 7).
- Garg, V., F. B. Sachse, and M. C. Sanguinetti: 2012, 'Tuning of EAG K⁺ channel inactivation: Molecular determinants of amplification by mutations and a small molecule.'. *The Journal of general physiology* **140**(3), 307–24. (page 5).
- Gingell, D. and I. Todd: 1979, 'Interference reflection microscopy. A quantitative theory for image interpretation and its application to cell-substratum separation measurement.'. *Biophysical journal* **26**(3), 507–26. (page 17).
- Gómez-Varela, D., E. Zwick-Wallasch, H. Knötgen, A. Sánchez, T. Hettmann, D. Ossipov, R. Weseloh, C. Contreras-Jurado, M. Rothe, W. Stühmer, and L. a. Pardo: 2007, 'Monoclonal antibody blockade of the human Eag1 potassium channel function exerts antitumor activity.'. *Cancer research* **67**(15), 7343–9. (pages 5, 6, 7, and 74).
- Gonçalves, J. T. and W. Stühmer: 2010, 'Calmodulin interaction with hEAG1 visualized by FRET microscopy.'. *PloS one* **5**(5), e10873. (page 3).
- Grunnet, M., N. MacAulay, N. Jorgensen, B. Jensen, S.-P. Olesen, and D. Klaerke: 2002, 'Regulation of cloned, Ca²⁺-activated K⁺ channels by cell volume changes'. *Pflugers Archiv : European journal of physiologyers Archiv European Journal of Physiology* **444**, 167–177. (page 10).
- Hamill, O. P., A. Marty, E. Neher, B. Sakmann, and F. J. Sigworth: 1981, 'Improved Patch-Clamp Techniques for High-Resolution Current Recording from Cells and Cell-Free Membrane Patches'. *Pflugers Arch* **391**, 85–100. (page 21).
- Hammadi, M., V. Chopin, F. Matifat, I. Dhennin-Duthille, M. Chasseraud, H. Sevestre, and H. Ouadid-Ahidouch: 2012, 'Human ether à-gogo K(+) channel 1 (hEag1) regulates MDA-MB-231 breast cancer cell migration through Orai1-dependent calcium entry.'. *Journal of cellular physiology* **227**(12), 3837–46. (pages 11, 72, and 74).

- Hartung, F., W. Stühmer, and L. a. Pardo: 2011, 'Tumor cell-selective apoptosis induction through targeting of KV10.1 via bifunctional TRAIL antibody'. *Molecular Cancer* **10**(1), 109. (page 7).
- Hassounah, N. B., T. a. Bunch, and K. M. McDermott: 2012, 'Molecular pathways: the role of primary cilia in cancer progression and therapeutics with a focus on Hedgehog signaling.'. *Clinical cancer research : an official journal of the American Association for Cancer Research* **18**(9), 2429–35. (page 11).
- Hawkins, D. and H. Abrahamse: 2005, 'Laboratory Methods for Evaluating the Effect of Low Level Laser Therapy (L LLT) In Wound Healing'. *African Journal of Biomedical Research* **8**, 1–14. (page 13).
- Hegle, A. P., D. D. Marble, and G. F. Wilson: 2006, 'A voltage-driven switch for ion-independent signaling by ether-à-go-go K⁺ channels.'. *Proceedings of the National Academy of Sciences of the United States of America* **103**(Track II), 2886–2891. (page 7).
- Hemmerlein, B., R. M. Weseloh, F. Mello de Queiroz, H. Knötgen, A. Sánchez, M. E. Rubio, S. Martin, T. Schliephacke, M. Jenke, Heinz-Joachim-Radzun, W. Stühmer, and L. A. Pardo: 2006, 'Overexpression of Eag1 potassium channels in clinical tumours.'. *Molecular cancer* **5**, 41. (pages 6, 6, and 76).
- Herrmann, S., M. Ninkovic, T. Kohl, E. Lörinczi, and L. a. Pardo: 2012, 'Cortactin controls surface expression of the voltage-gated potassium channel K(V)10.1.'. *The Journal of biological chemistry* **287**(53), 44151–63. (pages 11, 69, and 71).
- Hille, B.: 2001, 'Ion Channels of Excitable Membranes'. In: *Ion Channels of Excitable Membranes, Third Edition*. Sinauer Associates, Inc. (page 1).
- Hodgkin, A. L. and A. Huxley: 1952, 'A quantitative description of membrane current and its application to conduction and excitation on nerve'. *J. Physiol* **117**, 500–544. (page 1).
- Hoebe, R. a., H. T. M. Van der Voort, J. Stap, C. J. F. Van Noorden, and E. M. M. Manders: 2008, 'Quantitative determination of the reduction of phototoxicity and photobleaching by controlled light exposure microscopy.'. *Journal of Microscopy* **231**(Pt 1), 9–20. (page 13).
- Hoffmann, E. K. and S. F. Pedersen: 2006, 'Sensors and signal transduction pathways in vertebrate cell volume regulation'. *Contrib Nephrol* **152**, 54–104. (page 10).

- Hu, W.-P., J.-J. Wang, C.-L. Yu, C.-C. E. Lan, G.-S. Chen, and H.-S. Yu: 2007, 'Helium-neon laser irradiation stimulates cell proliferation through photostimulatory effects in mitochondria.'. *The Journal of investigative dermatology* **127**(8), 2048–57. (page 13).
- Huang, X. and L. Y. Jan: 2014, 'Targeting potassium channels in cancer'. *The Journal of Cell Biology* **206**(2), 151–162. (page 7).
- Ishikawa, M., R. Fujita, M. Takayanagi, Y. Takayanagi, and K. Sasaki: 2000, 'Reversal of acquired resistance to doxorubicin in K562 human leukemia cells by astemizole.'. *Biological & pharmaceutical bulletin* **23**(1), 112–115. (page 5).
- Izzard, C. S. and L. R. Lochner: 1976, 'Cell-to-substrate contacts in living fibroblasts: an interference reflexion study with an evaluation of the technique'. *Journal of Cell Science* **159**, 129–159. (page 17).
- Jacobson, K., Z. Rajfur, E. Vitriol, and K. Hahn: 2008, 'Chromophore-assisted laser inactivation in cell biology.'. *Trends in cell biology* **18**(9), 443–50. (page 13).
- Jay, D. G. and T. Sakurai: 1999, 'Chromophore-assisted laser inactivation (CALI) to elucidate cellular mechanisms of cancer.'. *Biochimica et biophysica acta* **1424**(2-3), M39–48. (page 13).
- Jenke, M., A. Sánchez, F. Monje, W. Stühmer, R. M. Weseloh, and L. a. Pardo: 2003, 'C-terminal domains implicated in the functional surface expression of potassium channels'. *EMBO Journal* **22**(3), 395–403. (page 3).
- Jiang, Y., a. Lee, J. Chen, V. Ruta, M. Cadene, B. T. Chait, and R. MacKinnon: 2003, 'X-ray structure of a voltage-dependent K⁺ channel'. *Nature* **423**(May), 33–41. (pages 2 and 4).
- Kaczmarek, L. K.: 2006, 'Non-conducting functions of voltage-gated ion channels.'. *Nature reviews. Neuroscience* **7**(10), 761–71. (page 7).
- Kaplan, W. D. and W. E. Trout: 1969, 'The behavior of four neurological mutants of *Drosophila*'. *Genetics* **61**(February), 399–409. (page 2).
- Kaye, G. I., L. F. Siegel, and R. R. Pascal: 1971, 'Cell replication of mesenchymal elements in adult tissues. I. The replication and migration of mesenchymal cells in the adult rabbit dermis.'. *The Anatomical record* **169**, 593–611. (page 9).
- Kim, K. W., C. H. Choi, T. H. Kim, C. H. Kwon, J. S. Woo, and Y. K. Kim: 2009, 'Silibinin inhibits glioma cell proliferation via Ca²⁺/ROS/MAPK-dependent mechanism in vitro and glioma tumor growth in vivo.'. *Neurochemical research* **34**(8), 1479–90. (page 14).

- Klein, K., T. Maier, V. C. Hirschfeld-Warneken, and J. P. Spatz: 2013, 'Marker-Free Phenotyping of Tumor Cells by Fractal Analysis of Reflection Interference Contrast Microscopy Images'. *Nano* **8**(13), 5474–5479. (page 38).
- Kolega, J.: 2004, 'Phototoxicity and photoinactivation of blebbistatin in UV and visible light.'. *Biochemical and biophysical research communications* **320**(3), 1020–5. (page 13).
- Kong, X., L. Chen, L. Jiao, X. Jiang, F. Lian, L. Junyan, K. Zhu, D. Du, J. Liu, H. Ding, N. Zhang, J. Shen, M. Zheng, K. Chen, X. Liu, H. Jiang, and C. Luo: 2014, 'Astemizole Arrests the Proliferation of Cancer Cells by Disrupting the EZH2-EED Interaction of Polycomb Repressive Complex 2'. *Journal of Medicinal Chemistry*. (pages 6 and 7).
- Krause, M. and A. Gautreau: 2014, 'Steering cell migration: lamellipodium dynamics and the regulation of directional persistence'. *Nature Reviews Molecular Cell Biology* **15**(9), 577–590. (page 12).
- Ku, H.: 1966, 'Notes on the use of propagation of error formulas'. *Journal of Research of the National Bureau of Standards, Section C: Engineering and Instrumentation* **70C**(4), 263. (page 61).
- Lacoste, J., K. Young, and C. M. Brown: 2013, 'Live-Cell Migration and Adhesion Turnover Assays'. In: D. J. Taatjes and J. Roth (eds.): *Cell Imaging Techniques: Methods and Protocols, Methods in Molecular Biology*, Vol. 931 of *Methods in Molecular Biology*. Totowa, NJ: Humana Press, Chapt. 3, pp. 61–84. (page 19).
- Lämmermann, T. and M. Sixt: 2009, 'Mechanical modes of 'amoeboid' cell migration'. *Current Opinion in Cell Biology* **21**, 636–644. (pages 9, 9, and 10).
- Lang, F., G. L. Busch, M. Ritter, H. Volkl, S. Waldegger, E. Gulbins, and D. Haussinger: 1998, 'Functional significance of cell volume regulatory mechanisms'. *Physiological Reviews* **78**(1), 247–306. (page 10).
- Lauffenburger, D. a. and a. F. Horwitz: 1996, 'Cell migration: a physically integrated molecular process.'. *Cell* **84**(3), 359–69. (pages 8, 14, and 73).
- Le Bras, G. F., K. J. Taubenslag, and C. D. Andl: 2012, 'The regulation of cell-cell adhesion during epithelial-mesenchymal transition, motility and tumor progression.'. *Cell adhesion & migration* **6**(4), 365–73. (pages 12, 12, 66, and 72).
- Liang, C.-C., A. Y. Park, and J.-L. Guan: 2007, 'In vitro scratch assay: a convenient and inexpensive method for analysis of cell migration in vitro.'. *Nature protocols* **2**(2), 329–33. (pages 14 and 15).

- Limozin, L. and K. Sengupta: 2007, 'Modulation of vesicle adhesion and spreading kinetics by hyaluronan cushions.'. *Biophysical journal* **93**(9), 3300–13. (pages 31 and 78).
- Limozin, L. and K. Sengupta: 2009, 'Quantitative reflection interference contrast microscopy (RICM) in soft matter and cell adhesion.'. *Chemphyschem : a European journal of chemical physics and physical chemistry* **10**(16), 2752–68. (pages 17 and 31).
- Lin, H., Z. Li, C. Chen, X. Luo, J. Xiao, D. Dong, Y. Lu, B. Yang, and Z. Wang: 2011, 'Transcriptional and post-transcriptional mechanisms for oncogenic overexpression of ether à go-go K⁺ channel.'. *PloS one* **6**(5), e20362. (page 72).
- Lucas, C., L. J. Criens-Poublon, C. T. Cockrell, R. J. de Haan, and R. J. D. Haan: 2002, 'Wound healing in cell studies and animal model experiments by Low Level Laser Therapy; were clinical studies justified? a systematic review.'. *Lasers in medical science* **17**(2), 110–34. (page 13).
- Ludwig, J., D. Owen, and O. Pongs: 1997, 'Carboxy-terminal domain mediates assembly of the voltage-gated rat ether-a-go-go potassium channel'. *EMBO Journal* **16**(21), 6337–6345. (page 3).
- Ludwig, J., H. Terlau, F. Wunder, A. Bruggemann, L. A. Pardo, and A. Marquardt: 1994, 'Functional expression of a rat homologue of the voltage gated ether á go-go potassium channel reveals differences in selectivity and activation kinetics between the Drosophila channel and its mammalian counterpart.'. *EMBO J.* **13**(19), 4451–4458. (pages 2 and 6).
- Magidson, V. and A. Khodjakov: 2013, 'Circumventing photodamage in live-cell microscopy'. *Methods Cell Biology* **40**(2), 516–533. (page 13).
- Maruta, H., K. Greer, and J. Rosenbaum: 1986, 'The Acetylation of Alpha-Tubulin and Its Relationship to the Assembly and Disassembly of Microtubules Preparation of Chlamydomonas Cell Body Extract'. *The Journal of Cell Biology* **103**(August), 571–579. (page 28).
- McDonald, R., S. J. Macgregor, J. G. Anderson, M. Maclean, and M. H. Grant: 2011, 'Effect of 405-nm high-intensity narrow-spectrum light on fibroblast-populated collagen lattices: an in vitro model of wound healing.'. *Journal of biomedical optics* **16**(4), 048003. (page 13).
- Menéndez, S. T., M. A. Villaronga, C. G. Vilorio, C. Suárez, and J. M. García-pedrero: 2012, 'Frequent aberrant expression of the human ether à go-go (hEAG1) potassium channel in head and neck cancer : pathobiological mechanisms and clinical implications'. *J Mol Med* (90), 1173–1184. (page 6).

- Meng, W., M. Numazaki, K. Takeuchi, Y. Uchibori, Y. Ando-Akatsuka, M. Tominaga, and T. Tominaga: 2004, 'DIP (mDia interacting protein) is a key molecule regulating Rho and Rac in a Src-dependent manner.'. *The EMBO journal* **23**(4), 760–71. (page 74).
- Michaud, E. J. and B. K. Yoder: 2006, 'The primary cilium in cell signaling and cancer.'. *Cancer research* **66**(13), 6463–7. (page 11).
- Miron-mendoza, M., J. Seemann, and F. Grinnell: 2008, 'Collagen Fibril Flow and Tissue Translocation Coupled to Fibroblast Migration in 3D Collagen Matrices'. *Molecular Biology of the Cell* **19**(May), 2051–2058. (page 73).
- Mitra, S. K., D. a. Hanson, and D. D. Schlaepfer: 2005, 'Focal adhesion kinase: in command and control of cell motility.'. *Nature reviews. Molecular cell biology* **6**(1), 56–68. (pages 11, 12, 12, and 28).
- Moore, M. a.: 2001, 'The role of chemoattraction in cancer metastases.'. *BioEssays : news and reviews in molecular, cellular and developmental biology* **23**(8), 674–6. (page 15).
- Morais-Cabral, J. a. H. and G. a. Robertson: 2014, 'The Enigmatic Cytoplasmic Regions of KCNH Channels.'. *Journal of molecular biology* pp. 1–10. (page 3).
- Mortensen, L. S., H. Schmidt, Z. Farsi, A. Barrantes-Freer, M. E. Rubio, R. Ufartes, J. Eilers, T. Sakaba, W. Stühmer, and L. a. Pardo: 2014, 'KV10.1 opposes activity-dependent increase in Ca²⁺ influx into the presynaptic terminal of the parallel fibre - Purkinje cell synapse.'. *The Journal of physiology* **1**, 181–196. (page 6).
- Müller, a., B. Homey, H. Soto, N. Ge, D. Catron, M. E. Buchanan, T. McClanahan, E. Murphy, W. Yuan, S. N. Wagner, J. L. Barrera, a. Mohar, E. Verástegui, and a. Zlotnik: 2001, 'Involvement of chemokine receptors in breast cancer metastasis.'. *Nature* **410**(6824), 50–6. (page 15).
- Murphy, P. M.: 2001, 'Chemokines and the molecular basis of cancer metastasis'. *Clinical implications of basic research* **345**(11), 833–835. (page 15).
- Napp, J., F. Monje, W. Stühmer, and L. A. Pardo: 2005, 'Glycosylation of Eag1 (Kv10.1) potassium channels: intracellular trafficking and functional consequences.'. *The Journal of biological chemistry* **280**(33), 29506–12. (pages 2, 21, 27, 47, and 76).
- Neher, E., B. Sakmann, and J. H. Steinbach: 1978, 'The Extracellular Patch Clamp: A Method for Resolving Currents through Individual Open Channels in Biological Membranes'. *Pflügers Arch* **228**, 219–228. (page 1).

- Nelson, W. J.: 2008, 'Regulation of cell-cell adhesion by the cadherin-catenin complex'. *Biochem Soc Trans* **36**(Pt 2), 149–155. (pages 12, 72, and 74).
- Ngok, S. P., R. Geyer, A. Kourtidis, N. Mitin, R. Feathers, C. Der, and P. Z. Anastasiadis: 2013, 'TEM4 is a junctional Rho GEF required for cell-cell adhesion, monolayer integrity and barrier function.'. *Journal of cell science* **126**(Pt 15), 3271–7. (page 72 and 72).
- Ninkovic, M., M. Mitkovski, T. Kohl, W. Stühmer, and L. A. Pardo: 2012, 'Physical and Functional Interaction of K(V)10.1 with Rabaptin-5 Impacts Ion Channel Trafficking.'. *FEBS letters* **null**(null). (pages 49, 69, and 71).
- North, A. J.: 2006, 'Seeing is believing? A beginners' guide to practical pitfalls in image acquisition.'. *The Journal of Cell biology* **172**(1), 9–18. (pages 13 and 14).
- Occhiodoro, T., L. Bernheim, J. H. Liu, P. Bijlenga, M. Sinnreich, C. R. Bader, and J. Fischer-Lougheed: 1998, 'Cloning of a human ether-a-go-go potassium channel expressed in myoblasts at the onset of fusion'. *FEBS Letters* **434**, 177–182. (pages 2, 2, and 6).
- Ortiz, C. S., D. Montante-Montes, M. Saqui-Salces, L. M. Hinojosa, A. Gamboa-Dominguez, E. Hernández-Gallegos, B. Martínez-Benítez, M. Del Rosario Solís-Pancoatl, E. Garcia-Villa, A. Ramírez, R. Aguilar-Guadarrama, P. Gariglio, L. A. Pardo, W. Stühmer, and J. Camacho: 2011, 'Eag1 potassium channels as markers of cervical dysplasia'. *Oncol Rep* **26**(6), 1377–1383. (page 6).
- Pardo, L. A.: 2004, 'Voltage-gated potassium channels in cell proliferation.'. *Physiology (Bethesda, Md.)* **19**, 285–92. (page 7).
- Pardo, L. A., A. Bruggemann, J. Camacho, and W. Stühmer: 1998, 'Cell cycle-related changes in the conducting properties of r-eag K⁺ channels.'. *The Journal of Cell biology* **143**(3), 767–75. (page 5 and 5).
- Pardo, L. A., C. Contreras-Jurado, M. Zientkowska, F. Alves, and W. Stühmer: 2005, 'Role of voltage-gated potassium channels in cancer'. *J Membr Biol* **205**(3), 115–124. (pages 6 and 72).
- Pardo, L. A., D. del Camino, A. Sánchez, F. Alves, A. Bruggemann, S. Beckh, and W. Stühmer: 1999, 'Oncogenic potential of EAG K(+) channels'. *EMBO J* **18**(20), 5540–5547. (pages 6, 72, and 74).
- Pardo, L. A. and W. Stühmer: 2008, 'Eag1 as a cancer target'. *Expert Opin Ther Targets* **12**(7), 837–843. (pages 6 and 7).

- Pardo, L. A. and W. Stühmer: 2013, 'The roles of K(+) channels in cancer.'. *Nature Publishing Group* **14**(1), 39–48. (page 71).
- Parsons, J. T., A. R. Horwitz, and M. a. Schwartz: 2010, 'Cell adhesion: integrating cytoskeletal dynamics and cellular tension.'. *Nature reviews. Molecular cell biology* **11**(9), 633–43. (pages 8, 12, 14, 69, and 71).
- Parsons, M. E. and C. R. Ganellin: 2006, 'Histamine and its receptors.'. *British journal of pharmacology* **147 Suppl**, S127–S135. (page 5).
- Patt, S., K. Preuß at, C. Beetz, R. Kraft, M. Schrey, R. Kalff, K. Schönherr, and S. H. Heinemann: 2004, 'Expression of ether à go-go potassium channels in human gliomas'. *Neuroscience Letters* **368**, 249–253. (page 6).
- Pattison, D. I. and M. J. Davies: 2006, 'Actions of ultraviolet light on cellular structures.'. *Exs* (96), 131–57. (page 13).
- Pedersen, S. F., E. K. Hoffmann, and J. W. Mills: 2001, 'The cytoskeleton and cell volume regulation.'. *Comparative biochemistry and physiology. Part A, Molecular & integrative physiology* **130**, 385–399. (pages 10 and 12).
- Petrie, R. J., A. D. Doyle, and K. M. Yamada: 2009, 'Random versus directionally persistent cell migration.'. *Nature reviews. Molecular cell biology* **10**(8), 538–49. (page 74).
- Pettit, E. J. and F. S. Fay: 1998, 'Cytosolic free calcium and the cytoskeleton in the control of leukocyte chemotaxis.'. *Physiological reviews* **78**(4), 949–967. (page 10 and 10).
- Pierres, A., A. M. Benoliel, and P. Bongrand: 2002, 'Cell fitting to adhesive surfaces: A prerequisite to firm attachment and subsequent events'. *European Cells and Materials* **3**, 31–45. (pages 28 and 38).
- Pillozzi, S. and A. Arcangeli: 2010, 'Physical and functional interaction between integrins and hERG1 channels in cancer cells.'. *Advances in experimental medicine and biology* **674**, 55–67. (pages 11, 12, 71, and 72).
- Pillozzi, S., M. Masselli, E. De Lorenzo, B. Accordi, E. Cilia, O. Crociani, A. Amedei, M. Veltroni, M. D'Amico, G. Basso, A. Becchetti, D. Campana, and A. Arcangeli: 2011, 'Chemotherapy resistance in acute lymphoblastic leukemia requires hERG1 channels and is overcome by hERG1 blockers.'. *Blood* **117**(3), 902–14. (page 74).
- Rahnama, F., F. Shafiei, P. D. Gluckman, M. D. Mitchell, and P. E. Lobie: 2006, 'Epigenetic regulation of human trophoblastic cell migration and invasion.'. *Endocrinology* **147**(11), 5275–83. (pages 14 and 72).

- Rasheed, S., W. A. Nelson-Rees, E. M. Toth, P. Arnstein, and M. B. Gardner: 1974, 'Characterization of a newly derived human sarcoma cell line (HT-1080)'. *Cancer* pp. 1027–1033. (pages 20 and 66).
- Restrepo-Angulo, I., C. Sanchez-Torres, and J. Camacho: 2011, 'Human EAG1 potassium channels in the epithelial-to-mesenchymal transition in lung cancer cells.'. *Anti-cancer research* **31**(4), 1265–70. (page 11).
- Reynolds, J. L., J. Akhter, and D. L. Morris: 1996, 'In vitro effect of histamine and histamine H1 and H2 receptor antagonists on cellular proliferation of human malignant melanoma cell lines.'. *Melanoma research* **6**(2), 95–99. (page 5).
- Ridley, A. J., M. a. Schwartz, K. Burridge, R. a. Firtel, M. H. Ginsberg, G. Borisy, J. T. Parsons, and A. R. Horwitz: 2003, 'Cell migration: integrating signals from front to back.'. *Science (New York, N.Y.)* **302**(5651), 1704–9. (pages 8, 69, 73, and 74).
- Robertson, G. a., J. W. Warmke, and B. Ganetzky: 1996, 'Potassium currents expressed from Drosophila and mouse eag cDNAs in Xenopus oocytes'. *Neuropharmacology* **35**(7), 841–850. (page 2).
- Rodriguez, F. J., L. J. Lewis-Tuffin, and P. Z. Anastasiadis: 2012, 'E-cadherin's dark side: possible role in tumor progression.'. *Biochimica et biophysica acta* **1826**(1), 23–31. (pages 12, 66, and 73).
- Sanz-Moreno, V. and C. J. Marshall: 2009, 'Rho-GTPase signaling drives melanoma cell plasticity.'. *Cell cycle (Georgetown, Tex.)* **8**(10), 1484–7. (page 73).
- Sarkar, P., S. V. Koushik, S. S. Vogel, I. Gryczynski, and Z. Gryczynski: 2009, 'Photophysical properties of Cerulean and Venus fluorescent proteins.'. *Journal of biomedical optics* **14**(3), 034047. (page 67).
- Satir, P., L. B. Pedersen, and S. T. Christensen: 2010, 'The primary cilium at a glance.'. *Journal of cell science* **123**(Pt 4), 499–503. (pages 11 and 28).
- Schilling, J., K. Sengupta, S. Goennenwein, A. Bausch, and E. Sackmann: 2004, 'Absolute interfacial distance measurements by dual-wavelength reflection interference contrast microscopy'. *Physical Review E* **69**(2), 021901. (page 31).
- Schindelin, J., I. Arganda-Carreras, E. Frise, V. Kaynig, M. Longair, T. Pietzsch, S. Preibisch, C. Rueden, S. Saalfeld, B. Schmid, J.-Y. Tinevez, D. J. White, V. Hartenstein, K. Eliceiri, P. Tomancak, and A. Cardona: 2012, 'Fiji: an open-source platform for biological-image analysis.'. *Nature methods* **9**(7), 676–82. (page 34).

- Schneider, L., M. Cammer, J. Lehman, S. K. Nielsen, C. F. Guerra, I. R. Veland, C. Stock, E. K. Hoffmann, B. K. Yoder, A. Schwab, P. Satir, S. T. Christensen, K. Sonja, and K. Hoffmann: 2010, 'Directional Cell Migration and Chemotaxis in Wound Healing Response to PDGF-AA are Coordinated by the Primary Cilium in Fibroblasts'. *Cellular Physiology and Biochemistry* **25**(2-3), 279–292. (page 11).
- Schneider, L., C.-M. Stock, P. Dieterich, B. H. Jensen, L. B. Pedersen, P. Satir, A. Schwab, S. T. Christensen, and S. F. Pedersen: 2009, 'The Na⁺/H⁺ exchanger NHE1 is required for directional migration stimulated via PDGFR-alpha in the primary cilium.'. *The Journal of Cell biology* **185**(1), 163–76. (pages 11 and 28).
- Schwab, A., A. Fabian, P. Hanley, and C. Stock: 2012, 'Role of ion channels and transporters in cell migration.'. *Physiological reviews* **92**(4), 1865–913. (page 10 and 10).
- Schwab, A., P. Hanley, A. Fabian, and C. Stock: 2008, 'Potassium channels keep mobile cells on the go.'. *Physiology (Bethesda, Md.)* **23**, 212–20. (pages 8, 10, and 15).
- Schwab, A., V. Nechyporuk-Zloy, A. Fabian, and C. Stock: 2007, 'Cells move when ions and water flow.'. *Pflügers Archiv : European journal of physiology* **453**(4), 421–32. (pages 8 and 69).
- Schwab, A., L. Wojnowski, K. Gabriel, and H. Oberleithner: 1994, 'Oscillating Activity of a Ca²⁺ -sensitive K⁺ Channel'. *J. Clin. Invest* **93**, 1631–1636. (page 10).
- Schwartz, M. a. and A. R. Horwitz: 2006, 'Integrating adhesion, protrusion, and contraction during cell migration.'. *Cell* **125**(7), 1223–5. (page 10).
- Seeger-Nukpezah, T. and E. a. Golemis: 2012, 'The extracellular matrix and ciliary signaling.'. *Current opinion in cell biology* **24**(5), 652–61. (pages 11, 14, and 72).
- Sheetz, M. P.: 2001, 'Cell control by membrane-cytoskeleton adhesion'. *Nat Rev Mol Cell Biol* **2**(5), 392–396. (page 12).
- Simons, C., L. D. Rash, J. Crawford, L. Ma, B. Cristofori-Armstrong, D. Miller, K. Ru, G. J. Baillie, Y. Alanay, A. Jacquinet, F.-G. Debray, A. Verloes, J. Shen, G. Yesil, S. Guler, A. Yuksel, J. G. Cleary, S. M. Grimmond, J. McGaughran, G. F. King, M. T. Gabbett, and R. J. Taft: 2014, 'Mutations in the voltage-gated potassium channel gene KCNH1 cause Temple-Baraitser syndrome and epilepsy.'. *Nature Genetics* **47**(November), 73–77. (page 6).
- Singh, R. P., S. Dhanalakshmi, S. Mohan, C. Agarwal, and R. Agarwal: 2006, 'Silibinin inhibits UVB- and epidermal growth factor-induced mitogenic and cell survival signal-

- ing involving activator protein-1 and nuclear factor-kappaB in mouse epidermal JB6 cells.’. *Molecular cancer therapeutics* **5**(5), 1145–53. (page 14).
- Singla, V. and J. F. Reiter: 2006, ‘The Primary Cilium as the Cell’s Antenna : Signaling at a Sensory Organelle’. *Science* **313**(August), 629–633. (page 11).
- Smith, L. a., H. Aranda-Espinoza, J. B. Haun, M. Dembo, and D. a. Hammer: 2007, ‘Neutrophil traction stresses are concentrated in the uropod during migration.’. *Biophysical journal* **92**(7), L58–60. (page 73).
- Sorokin, S. P.: 1968, ‘Centriole formation and ciliogenesis.’. *J. Cell Sci.* **11**, 213–216. (page 11).
- Spitler, R. and M. W. Berns: 2014, ‘Comparison of laser and diode sources for acceleration of in vitro wound healing by low-level light therapy.’. *Journal of biomedical optics* **19**(3), 38001. (page 67).
- Stephens, D. J. and V. J. Allan: 2003, ‘Light microscopy techniques for live cell imaging.’. *Science (New York, N.Y.)* **300**(5616), 82–6. (pages 13 and 15).
- Stock, C., F. T. Ludwig, P. J. Hanley, and A. Schwab: 2013, ‘Roles of ion transport in control of cell motility.’. *Comprehensive Physiology* **3**(1), 59–119. (pages 10 and 15).
- Stout, A.: 1948, ‘Fibrosarcoma: The Malignant Tumor of Fibroblasts’. *Cancer* p. 34. (page 66).
- Stühmer, W. and L. A. Pardo: 2010, ‘K(+) channels as therapeutic targets in oncology’. *Future Med Chem* **2**(5), 745–755. (page 7).
- Sung, B. H., X. Zhu, I. Kaverina, and A. M. Weaver: 2011, ‘Cortactin controls cell motility and lamellipodial dynamics by regulating ECM secretion.’. *Current biology : CB* **21**(17), 1460–9. (page 11).
- Sung, H. J., Y. Kim, H. Kang, J. W. Sull, Y. S. Kim, S.-W. Jang, and J. Ko: 2012, ‘Inhibitory effect of Trolox on the migration and invasion of human lung and cervical cancer cells.’. *International journal of molecular medicine* **29**(2), 245–51. (page 14).
- Surrey, T., M. B. Elowitz, P. E. Wolf, F. Yang, F. Nédélec, K. Shokat, and S. Leibler: 1998, ‘Chromophore-assisted light inactivation and self-organization of microtubules and motors.’. *Proceedings of the National Academy of Sciences of the United States of America* **95**(8), 4293–8. (page 13 and 13).

- Swedlow, J. R., P. D. Andrews, and M. Platani: 2009, 'In vivo imaging of mammalian cells: image acquisition and analysis.'. *Cold Spring Harbor protocols* **2009**(9), pdb.ip70. (page 14).
- Swen, S.-P., C.-S. Wu, and H.-S. Yu: 2002, 'Effect of Helium-Neon laser on human melanoma cell migration'. *Biomedical Engineering* **8**(14), 243–250. (page 13).
- Takeichi, M.: 1988, 'The cadherins: cell-cell adhesion molecules controlling animal morphogenesis.'. *Development (Cambridge, England)* **102**(4), 639–55. (pages 12 and 72).
- Terlau, H., J. Ludwig, R. Steffan, O. Pongs, W. Stühmer, and S. H. Heinemann: 1996, 'Extracellular Mg²⁺ regulates activation of rat eag potassium channel.'. *Pflügers Archiv : European journal of physiology* **432**(2), 301–12. (page 5).
- Thévenaz, P., U. E. Ruttimann, and M. Unser: 1998, 'A pyramid approach to subpixel registration based on intensity.'. *IEEE transactions on image processing : a publication of the IEEE Signal Processing Society* **7**(1), 27–41. (page 78).
- Thiery, J. P.: 2002, 'Epithelial-mesenchymal transitions in tumour progression.'. *Nature reviews. Cancer* **2**(June), 442–454. (page 10).
- Tinevez, J.-Y., J. Dragavon, L. Baba-Aissa, P. Roux, E. Perret, A. Canivet, V. Galy, and S. Shorte: 2012, 'A quantitative method for measuring phototoxicity of a live cell imaging microscope.'. In: *Methods in enzymology*, Vol. 506. Elsevier Inc., 1 edition, pp. 291–309. (page 13).
- Toral, C., M. E. Mendoza-Garrido, E. Azorín, E. Hernández-Gallegos, J. C. Gomora, D. M. Delgadillo, C. Solano-Agama, and J. Camacho: 2007, 'Effect of extracellular matrix on adhesion, viability, actin cytoskeleton and K⁺ currents of cells expressing human ether {à} go-go channels'. *Life Sci* **81**(3), 255–265. (pages 8, 10, and 14).
- Ufartes, R., T. Schneider, L. S. Mortensen, C. de Juan Romero, K. Hentrich, H. Knoetgen, V. Beilinson, W. Moebius, V. Tarabykin, F. Alves, L. a. Pardo, J. N. P. Rawlins, and W. Stühmer: 2013, 'Behavioural and functional characterization of Kv10.1 (Eag1) knockout mice.'. *Human molecular genetics* **22**(11), 2247–62. (page 6).
- Urrego, D., A. P. Tomczak, F. Zahed, W. Stühmer, and L. A. Pardo: 2014, 'Potassium channels in cell cycle and cell proliferation.'. *Philosophical transactions of the Royal Society of London. Series B, Biological sciences* **369**(1638), 20130094. (pages 5 and 7).
- Valderrama, F., S. Thevapala, and A. J. Ridley: 2012, 'Radixin regulates cell migration and cell-cell adhesion through Rac1.'. *Journal of cell science* **125**(Pt 14), 3310–9. (page 72).

- van de Linde, S., M. Heilemann, and M. Sauer: 2012, 'Live-cell super-resolution imaging with synthetic fluorophores.'. *Annual review of physical chemistry* **63**, 519–40. (page 13).
- Vargas, F., I. Martinez Volkmar, J. Sequera, H. Mendez, J. Rojas, G. Fraile, M. Velasquez, and R. Medina: 1998, 'Photodegradation and phototoxicity studies of furosemide. Involvement of singlet oxygen in the photoinduced hemolysis and lipid peroxidation.'. *Journal of photochemistry and photobiology. B, Biology* **42**(3), 219–25. (page 13).
- Verschuieren, H.: 1985, 'Interference reflection microscopy in cell biology: methodology and applications.'. *Journal of cell science* **75**, 279–301. (pages 16, 17, 17, and 18).
- Warmke, J. W. and B. Ganetzky: 1994, 'A family of potassium channel genes related to eag in Drosophila and mammals.'. *Proceedings of the National Academy of Sciences of the United States of America* **91**(April 1994), 3438–3442. (page 2).
- Watkins, S. C. and C. M. St Croix: 2013, 'Building a live cell microscope: what you need and how to do it.'. *Current protocols in cytometry / editorial board, J. Paul Robinson, managing editor ... [et al.] Chapter 2*(July), Unit2.21. (page 14).
- Webb, D. J., K. Donais, L. a. Whitmore, S. M. Thomas, C. E. Turner, J. T. Parsons, and A. F. Horwitz: 2004, 'FAK-Src signalling through paxillin, ERK and MLCK regulates adhesion disassembly.'. *Nature cell biology* **6**(2), 154–61. (page 12).
- Webb, D. J., J. T. Parsons, and A. F. Horwitz: 2002, 'Adhesion assembly, disassembly and turnover in migrating cells – over and over and over again.'. *Nature cell biology* **4**(4), E97–100. (pages 12 and 69).
- Weber, C., F. M. De Queiroz, B. R. Downie, A. Suckow, W. Stühmer, and L. a. Pardo: 2006, 'Silencing the activity and proliferative properties of the human EagI potassium channel by RNA interference'. *Journal of Biological Chemistry* **281**, 13030–13037. (pages 6, 7, and 66).
- Wheatley, D. N.: 1971, 'Cilia in cell-cultured fibroblasts. 3. Relationship between mitotic activity and cilium frequency in mouse 3T6 fibroblasts.'. *Journal of anatomy* **110**, 367–382. (page 11).
- Wilkinson, T. C. I., M. J. Gardener, and W. a. Williams: 2014, 'Discovery of Functional Antibodies Targeting Ion Channels.'. *Journal of biomolecular screening* pp. 1–14. (page 7).
- Wojtovich, A. P. and T. H. Foster: 2014, 'Optogenetic control of ROS production.'. *Redox biology* **2**, 368–376. (page 13).

- Wolfenson, H., Y. I. Henis, B. Geiger, A. D. Bershadsky, and A. Manuscript: 2009, 'The heel and toe of the cell's foot: a multifaceted approach for understanding the structure and dynamics of focal adhesions'. *Cell Motil Cytoskeleton* **66**(11), 1017–1029. (page 50).
- Wong, M. K. and a. I. Gotlieb: 1988, 'The reorganization of microfilaments, centrosomes, and microtubules during in vitro small wound reendothelialization.'. *The Journal of Cell biology* **107**(5), 1777–83. (page 14).
- Wu, X., D. Zhong, Q. Gao, W. Zhai, Z. Ding, and J. Wu: 2013, 'MicroRNA-34a Inhibits Human Osteosarcoma Proliferation by Downregulating Ether à go-go 1 Expression.'. *International journal of medical sciences* **10**(6), 676–82. (page 6).
- Wulff, H., N. A. Castle, and L. A. Pardo: 2009, 'Voltage-gated potassium channels as therapeutic targets'. *Nat Rev Drug Discov* **8**(12), 982–1001. (page 6).
- Yu, H.-S., C.-S. Wu, C.-L. Yu, Y.-H. Kao, and M.-H. Chiou: 2003, 'Helium-neon laser irradiation stimulates migration and proliferation in melanocytes and induces repigmentation in segmental-type vitiligo.'. *The Journal of investigative dermatology* **120**(1), 56–64. (pages 10, 13, and 13).
- Zahm, J. M., H. Kaplan, a. L. Hérard, F. Doriot, D. Pierrot, P. Somelette, and E. Puchelle: 1997, 'Cell migration and proliferation during the in vitro wound repair of the respiratory epithelium.'. *Cell motility and the cytoskeleton* **37**(1), 33–43. (pages 14 and 69).
- Zhang, X., G. Jiang, Y. Cai, S. J. Monkley, D. R. Critchley, and M. P. Sheetz: 2008, 'Talin depletion reveals independence of initial cell spreading from integrin activation and traction.'. *Nature cell biology* **10**(9), 1062–8. (page 73).
- Zhao, X. and J.-L. Guan: 2011, 'Focal adhesion kinase and its signaling pathways in cell migration and angiogenesis.'. *Advanced drug delivery reviews* **63**(8), 610–5. (pages 11, 12, 69, and 73).
- Zhu, N. W., C. M. Perks, a. R. Burd, and J. M. Holly: 1999, 'Changes in the levels of integrin and focal adhesion kinase (FAK) in human melanoma cells following 532 nm laser treatment.'. *International journal of cancer. Journal international du cancer* **82**(3), 353–8. (page 8).

Curriculum vitae

Personal Details

Name: Ioannis Alexopoulos

Date of Birth: 16/08/1978

Place of Birth: Chania, Crete, Greece

✉ alexopoulos@em.mpg.de ✉ jalexop@gmail.com

Education

06/2012 - now: PhD Student at Max Planck Institute for Experimental Medicine. Participation at Molecular Medicine PhD Program

10/2004 - 10/2007: MSc in Bioinformatics, Department of Cell Biology & Biophysics, Faculty of Biology at National and Kapodistrian University of Athens, Greece. Degree 86%.

09/1997 - 09/2004: BSc in Biology, Faculty of Biology at National and Kapodistrian University of Athens, Greece. Degree 64.5%.

06/1996 - 06/1997: PanHellenic exams; curriculum 2nd: Biological and Medical studies. Main Subjects: Biology (degree 86.3%), Physics (degree 99.4%), Chemistry (degree 97%) and Assay Writing (degree 82%).

1996: Graduation from the 3rd General Lyceum of Egaleo. Degree 89.5%.

Research Experience

6/2012 - now: PhD thesis project at Max Planck for Experimental Medicine, under the supervision of Dr. Mišo Mitkovski with title 'The $K_v10.1$ voltage gated potassium ion channel modulates the cell adhesion and mi-

gration cancer hallmarks' with extended use of confocal laser scanning microscopy and implementation of image analysis algorithms in FIJI-ImageJ macros. Molecular biology assays (PCR and RealTime PCR), biochemistry assays (Western Blot and IP-WB), immunocytochemistry and mammalian cell culturing.

- 9/2005 - 2/2007:** M.Sc thesis project at the Postgraduate Program in Bioinformatics at the faculty of Biology at the National and Kapodistrian University of Athens in Greece under the supervision of Assistant Professor P. G. Bagos with subject 'Computing study of protein-protein interactions in multi-domain proteins of *Escherichia coli*'. Extended use of molecular graphic programs and databases. Build of algorithms calculating molecule distances in Perl programming language.
- 1/2004 - 4/2004:** Participation at the research work with subject 'Structural studies of the interactions of histone dimmers in the Archaeal nucleosome by comparative modeling'. Use of multiple sequence alignment programs (ClustalW), comparative modeling methods and implementation of algorithms in Perl for the measurement of structural distances.
- 1/2001 - 12/2005:** Participation at the research program of the University of Athens with the title 'Construction of a full system for the study of intra-cellular protein receptors'. Retrieval and annotation of entries from protein databases. Implementation of data retrieval algorithms in Perl. Database debugging.
- 9/2000 - 9/2002:** Final year project at the section of Cell Biology and Biophysics at the department of Biology at the National and Kapodistrian University of Athens under the supervision of Professor S. J. Hamodrakas with subject 'Computational analysis of linkers in multi-domain proteins of *Escherichia coli*'. Learn and use of molecular graphic programs (O, Grasp, SwissPdbViewer, RasMol). Extended use of Perl algorithms and biological databases.
-

Working Experience

- 11/2006 - 11/2011:** Product and Application Specialist at the Support (www.zcgroup.gr) and R&D (www.flowcytogen.com) Department of P. Zafiroopoulos S.A. Support and customer training for a variety of instruments and reagents in the field of:

Automated Imaging Platforms: -Cytogenetics (Karyotyping, FISH) - Pathology (CISH, FISH) -Spectral Imaging for cytogenetics and pathology.

Molecular Biology: -PCR (gel detection systems with horizontal or vertical electrophoresis systems, strip detection systems, membrane hybridization systems, HLA-typing systems). -Real Time PCR (all well known technics and technologies like FRET, TaqMAN Probe, Hybridization probes, Beacon Probes etc.). -FISH.

Flow Cytometry: Multi-parametric immunophenotyping, Flow-FISH, Multi-Bead Arrays.

Immunology: EIA (ELISA)

2/2006 - 10/2006: Military service at the Hellenic Navy Hospital with the specialty of nurse.

1/2005 - 10/2005: Administration of the computer systems of the 'MSc in Bioinformatics' Program (<http://bioinformatics.biol.uoa.gr/msc/>).

1/2005 - 10/2005: Administration and web design of the official web site of the 'MSc in Bioinformatics' Program (<http://bioinformatics.biol.uoa.gr/msc/>).

2001 - 2005: Participation at the research program of the University of Athens with the title 'Construction of a full system for the study of intra-cellular protein receptors'

Computer Skills

Operating Systems: MAC OS X, UNIX (SGI-IRIX), LINUX (Red Hat Linux, Debian, SUSE Linux etc.), MS-WINDOWS (all versions).

Software Suites: MS-Office, Open Office, Adobe eGolive, Adobe Photoshop, Macromedia Dreamweaver MX 2004, Imaris Bitplane, FIJI/ImageJ, Inkscape.

Website administration and design:

- <http://bioinformatics.biol.uoa.gr/msc/> (Design and administration during 2006 of the official web page of Bioinformatics MSc).
- <http://www.biol.uoa.gr/> (Design and administration from 2007 to 2010 of the official page of Faculty of Biology at National and Kapodistrian University of Athens).

Programming Languages: Perl, Fiji/ImageJ macros, Java (basic experience), HTML Programming, L^AT_EX, PhP (basic experience).

Databases: Basic experience in construction and administration of databases (SQL, MySQL).

Languages

- Greek: Native
 - English: Fluent
 - German: Basic
-

Scientific Congresses – Presentations

- *Ioannis Alexopoulos*, Araceli Sánchez, Sabine Klöppner, Luis Pardo, Walter Stühmer, Mišo Mitkovski, 'K_v10.1 overexpression results in cell-cell adhesion deficits and increased cell motility', 2013, Winter School on Bioimaging, sensing, and therapeutic applications of nanomaterials.
- *Ioannis Alexopoulos*, Araceli Sánchez, Ye Chen, Sabine Klöppner, Luis Pardo, Walter Stühmer, Mišo Mitkovski, 'K_v10.1 overexpression coincides with enhanced cell motility', 2012, International Meeting on Ion Transport and Cancer (ITC).
- *Alexopoulos, I.K.*, Bagos, P.G. and Hamodrakas, S.J. 'Analysis of domain interactions in crystallographically solved proteins of *Escherichia coli*', 2003, Hellenic Society for Biological Sciences, 25th Conference - Metelene - Lesvos.
- Liakopoulos, Th.D., Bagos, P.G., *Alexopoulos, I.K.* and Hamodrakas, S.J. 'A web tool to select biological sequences from a given set, with similarity/homology less than a user-defined level', 2003, Hellenic Society for Biological Sciences, 25th Conference - Metelene - Lesvos.
- Kapasa, M.G., *Alexopoulos, I.K.*, Papandreou, N.C., Moudrianakis, E.N. and Hamodrakas, S.J. 'Structural studies of the interactions of histone dimmers in the Archaeal nucleosome by comparative modeling.' 2004, Hellenic Society for Biological Sciences, 26th Conference – Volos

Publications

- Aura M. Jiménez-Garduño, Miso Mitkovski, Ioannis K. Alexopoulos, Araceli Sánchez, Walter Stühmer, Luis A. Pardo, Alicia Ortega, $K_v10.1$ K⁺-channel plasma membrane discrete domain partitioning and its functional correlation in neurons, *Biochimica et Biophysica Acta (BBA) - Biomembranes*, Volume 1838, Issue 3, March 2014, Pages 921-931.
- Schanila Nawaz, Paula Sánchez, Sebastian Schmitt, Nicolas Snaidero, Mišo Mitkovski, Caroline Velte, Bastian Rouven Brückner, Ioannis Alexopoulos, Tim Czopka, Sang Yong Jung, Jeong Seop Rhee, Andreas Janshoff, Walter Witke, Iwan AT Schaap, David A. Lyons, Mikael Simons, “Actin filament turnover drives leading edge growth during myelin sheath formation in the central nervous system”, [Submitted]
- I. K. Alexopoulos, L. A. Pardo, W. Stühmer, M. Mitkovski, “ $K_v10.1$ overexpression enhances cell migration, while reducing cell-cell and cell-surface adhesion”, [Working Title - Under Preparation]
- I. K. Alexopoulos, K. Bröking, L. A. Pardo, W. Stühmer, M. Mitkovski, “Cell migration is affected by the level and the pattern of laser energy dosage”, [Working Title - Under Preparation]
- I. K. Alexopoulos, W. Stühmer, M. Mitkovski, “ProRet: A novel algorithm to dynamically quantify surface adhesion ability from Interference Reflection Microscopy data”, [Working Title - Under Preparation]

References

- Prof. Dr. Walter Stühmer, dept. of Molecular Biology of Neuronal Signals, Max Planck Institute of Experimental Medicine, Göttingen. Member of PhD thesis committee. ✉ stuehmer@em.mpg.de
- Prof. Dr. Luis A. Pardo, dept. of Molecular Biology of Neuronal Signals, Max-Planck Institute of Experimental Medicine, Göttingen. Member of PhD thesis committee. ✉ pardo@em.mpg.de

- Dr. Mišo Mitkovski, Light Microscopy Facility, Max Planck Institute of Experimental Medicine, Göttingen. Supervisor of PhD thesis. ✉ mitkovski@em.mpg.de